



HAL
open science

Topological and electronic properties of electron-doped manganite thin films

Lorenzo Vistoli

► **To cite this version:**

Lorenzo Vistoli. Topological and electronic properties of electron-doped manganite thin films. Materials Science [cond-mat.mtrl-sci]. Université Paris Saclay (COMUE), 2019. English. NNT : 2019SACLS113 . tel-02645241

HAL Id: tel-02645241

<https://theses.hal.science/tel-02645241>

Submitted on 29 May 2020

HAL is a multi-disciplinary open access archive for the deposit and dissemination of scientific research documents, whether they are published or not. The documents may come from teaching and research institutions in France or abroad, or from public or private research centers.

L'archive ouverte pluridisciplinaire **HAL**, est destinée au dépôt et à la diffusion de documents scientifiques de niveau recherche, publiés ou non, émanant des établissements d'enseignement et de recherche français ou étrangers, des laboratoires publics ou privés.

Topological and Electronic Properties of Electron-Doped Manganite Thin Films

Thèse de doctorat de l'Université Paris-Saclay
préparée à l'Université Paris-Sud

Ecole doctorale n°564 Physique en Ile-de-France
Spécialité de doctorat : Physique

Thèse présentée et soutenue à Palaiseau, le 28/5/2019, par

LORENZO VISTOLI

Composition du Jury :

Mme. Pascale Foury-Leylekian Prof., Université Paris-Saclay	Présidente
Mme. Tamalika Banerjee Prof., Rijksuniversiteit Groningen	Rapporteuse
M. Olof Karis Prof., Uppsala Universitet	Rapporteur
Mme. Laurence Méchin Directrice de Recherche, GREYC Caen	Examinatrice
M. Manuel Bibes Directeur de Recherche, Unité Mixte de Physique CNRS/Thales	Directeur de thèse
M. Vincent Garcia Chargé de Recherche, Unité Mixte de Physique CNRS/Thales	Co-directeur de thèse
M. Julien Rault Beamline Scientist, Soleil Synchrotron	Invité

Introduction

Oxide materials crystallizing in the perovskite ABO_3 structure host a wide range of properties, from ferromagnetism to antiferromagnetism, from semiconductivity to metallicity or even superconductivity, strong correlations and heavy fermions, quasi-2D systems and multiferroism. Among these oxides, manganites are studied for their rich phase diagrams, and their spintronic and magnetoresistive properties, all of which are strongly tied to strong correlations and coupling to bosons. In thin films, these properties are easily tunable by strain, doping, and interface engineering, making manganite thin films a suitable playground to improve our understanding of the behavior of electrons in complex solids.

We take electron-doped $CaMnO_3$ as a case study of how strongly correlated oxides form bands and become conductive, owing to its strong sensitivity to electron doping (in the form of Ce for Ca substitution) which allows the system to transition to a metallic and weakly-ferromagnetic regime without any accompanying structural transitions that may bring about other effects. We used strain due to lattice mismatch with the single-crystal substrate to enhance this sensitivity and study the electronic structure as a function of electron doping. Strain also allows for the control of the magnetic properties of $CaMnO_3$ which can be forced, during magnetization reversal, to nucleate magnetic bubbles with a non-trivial topology arising from strong dipole interactions. By studying these topological properties as a function of electron doping, these manganite thin film are able to shed light on electron transport in the presence of topological structures in strongly correlated oxides.

Outline

In the first chapter we will give a topical overview of the state of art of magnetic skyrmions, skyrmion bubbles and perovskite manganites. Magnetic skyrmions are topological structures which are garnering interest among researchers due to their novel physics and promising applications. Skyrmions give rise to the hallmark topological Hall effect, whose physics are closely tied to that of the anomalous Hall effect. We will then introduce perovskite manganites, with a focus on their electronic and magnetic properties. These materials feature strong electron-phonon coupling and correlations, which influence electron transport. Skyrmion structures and topological Hall effect are known to be harbored in manganites, and recently their existence has been shown in manganite thin films (as well as in other oxides). These results are inspiring new research since manganites, and oxides in general, present physical phenomena that can interplay with magnetic skyrmions and are tunable through doping, strain, and interface engineering. Lastly, we will briefly describe perovskite ferroelectrics and how these can be used to modify the properties of manganites, and

Mott insulators in general.

In the second chapter we will describe growth process and basic properties of our CaMnO_3 thin films. The thin films were grown by pulsed laser deposition, and characterized by atomic force microscopy and X-ray diffraction. To measure magnetotransport, optical lithography was used to fabricate Hall bars. We also employed X-ray magnetic circular dichroism, X-ray absorption spectroscopy and electron energy loss spectroscopy to study the electronic and magnetic properties of the samples.

In the third chapter we report our findings on the electronic structure of CaMnO_3 and how it influences transport mechanisms. We performed angle-resolved photoemission spectroscopy, through which we were able to observe the Fermi surface of our manganite thin films. Upon further investigation, we discovered that charge carriers can be either electrons lightly coupled to phonons, or electrons that strongly couple to lattice vibrations and form the so-called polarons. We show how these heavy polarons form due to the breakdown of the Migdal approximation, which works in the single particle approximation. We also show how these findings are able to expand the current theory on electron transport in manganites, identifying the role of both carriers.

In the fourth chapter we report the presence of topological Hall effect in electron-doped manganite thin films. Magnetic force microscopy reveals how this effect is accompanied by the nucleation of magnetic bubbles, pointing out their topological nature. We investigated the behavior of the topological Hall effect with various dopings, observing a divergence as the system approaches its insulating phase. Thanks to a theory developed concomitantly with our work, we are able to identify correlations as the most likely mechanism behind this enhancement. These finding shed light on how correlations can influence transport in the presence of magnetic skyrmions, and how the topological Hall effect could be manipulated by combining our manganite thin films with ferroelectrics.

In the fifth and last chapter we will describe our attempts at observing ferroelectric field effect by combining a ferroelectric oxide with electron-doped manganite thin films. We were not able to measure any substantial field effect, and so we used scanning tunneling electron microscopy to investigate the ferroelectric switching of our bilayers, looking for a possible cause. We found that the ferroelectric is not able to completely switch polarization close to the ferroelectric/manganite interface. We were able to measure the depth profile of the carrier density, and observed that the accumulation and depletion of carrier occurs in properly switched interfaces, but ultimately is not able to give rise to sizable changes in the properties of the manganite electrode due to the lack of complete switching at the interface. These results highlight a major hurdle to overcome in order to fully realize Mott transistors with ferroelectric gating.

Contents

1	State of the art	1
1.1	Topological spin structures and transport phenomena	1
1.1.1	Magnetic skyrmions and skyrmion bubbles	2
1.1.1.1	Skyrmion bubbles and dipole-dipole interaction	3
1.1.1.2	Skyrmions in non-centrosymmetric crystals	5
1.1.1.3	Skyrmions in heterostructures	6
1.1.1.4	Topological devices	7
1.1.2	Topology and transport phenomena	7
1.1.2.1	Topological Hall effect	7
1.1.2.2	Anomalous Hall effect	9
1.2	Perovskite manganites	10
1.2.1	Crystal structure and electronic configuration	11
1.2.1.1	The perovskite unit cell	11
1.2.1.2	Crystal field splitting and Jahn-Teller effect	12
1.2.1.3	Correlations and metal-insulator transitions	13
1.2.2	Magnetic structure and properties	15
1.2.2.1	Single-valence manganites and superexchange	15
1.2.2.2	Mixed-valence manganites and double exchange	16
1.2.2.3	Dzyaloshinskii-Moriya interaction	18
1.2.3	Electronic properties and transport	19
1.2.3.1	Polarons and electronic transport	19
1.2.3.2	Mass enhancement	23
1.2.3.3	Electronic structure in reciprocal space	25
1.2.4	Topology in manganites	26
1.2.4.1	Skyrmions in manganites	26
1.2.4.2	Topological Hall effect in manganites	28
1.2.4.3	Anomalous Hall effect in manganites	29

1.2.5	CaMnO ₃	31
1.2.5.1	Bulk properties	31
1.2.5.2	Ce doping	32
1.2.5.3	CaMnO ₃ thin films	33
1.3	Oxide ferroelectric devices	34
1.3.1	BiFeO ₃	34
1.3.2	Ferroelectric control of Mott insulators	36
2	Manganite thin film growth and properties	41
2.1	Pulsed laser deposition	41
2.2	Structural properties	45
2.3	Electronic properties	48
2.4	Magnetic measurements	49
2.5	Device fabrication	51
3	Electronic structure of Ce-doped CaMnO₃ thin films: doping a charge-transfer insulator	55
3.1	Transport measurements	55
3.2	Electronic structure	57
3.3	Carrier-dependent electron-phonon coupling	64
3.4	Light and heavy charge carriers in transport	66
3.4.1	Hall resistivity	67
3.4.2	Longitudinal resistivity in the low temperature ferromagnetic phase	67
3.4.3	Longitudinal transport in the high temperature paramagnetic phase	70
4	Giant topological Hall effect in electron-doped CaMnO₃ thin films	73
4.1	Hall effect measurements and isolation of the topological Hall effect	73
4.1.1	Hall effect of a 4% Ce-doped CaMnO ₃ thin film	73
4.1.2	Topological Hall extraction and phase diagram	75
4.1.3	Strain dependence of the topological Hall effect	76
4.2	Micromagnetism of CaMnO ₃ : interpretation of the topological Hall effect	77
4.2.1	Magnetic force microscopy measurements	78
4.2.1.1	Polarity and topological charge of magnetic bubbles	80
4.2.2	Discussion on the possible origins of the topological Hall effect	81
4.3	Doping dependence and enhancement of the topological and anomalous Hall effect	83
4.3.1	Doping dependence of the micromagnetic structure	85
4.3.2	Doping and temperature dependence the Hall effect	87

Contents

4.3.2.1	Topological Hall effect	87
4.3.2.2	Anomalous Hall effect	87
4.3.3	Weak-coupling topological Hall effect	89
4.3.4	Discussion on possible mechanisms of mass enhancement	91
4.3.5	Enhancement of topological and anomalous Hall effect	94
5	Ferroelectric field effect in BiFeO₃/(Ca,Ce)MnO₃ bilayers	97
5.1	Ferroelectric field effect	97
5.2	Atomic scale analysis of polarization switching	101
5.3	Polarization-induced changes in electronic properties of (Ca,Ce)MnO ₃ at the atomic scale	104
6	Conclusions and Perspectives	109
6.1	Summary	109
6.2	Perspectives	111
	Bibliography	113

Contents

State of the art

1.1 Topological spin structures and transport phenomena

Topology in condensed matter physics is a field of growing interest due to the distinct topological phases and physical phenomena discovered in the past decade. In its strictest sense, topology is the study of properties that are preserved under continuous deformations, and as such it provides the mathematical means to study and predict novel phases and phenomena, such as topological insulators and quantum spin Hall effect. In this thesis we will focus solely on topological phenomena and structures in real space, where the topology can be understood from a core concept in physics: symmetry.

A ferromagnetic and an antiferromagnetic structure (Fig. 1.1a) are strikingly different systems with different properties, all of which can be traced back to the different symmetries of the magnetic configuration (respectively symmetry group $p_p(\bar{1})$ and p). For example, $\text{La}_{1-x}\text{Sr}_x\text{MnO}_3$ undergoes a transition at $x = 0.5$ from a ferromagnetic and metallic state to an antiferromagnetic insulating state. The magnetic and the metal-insulator transition, which occur at the same time, are tied together by the symmetry of the spin lattice of the material.

However, these two magnetic structures are topologically equivalent since one can slowly and continuously deform the antiferromagnetic lattice by rotating the spins of one of the sublattices, transforming it into a ferromagnetic lattice. Real-space topology in condensed matter deals with structures that are topologically non-trivial, i.e. topologically distinct from conventional phases like ferromagnetism. Topological phenomena in materials thus arise from properties that go beyond the conventional properties stemming from symmetry, and as such the topological study of materials is able to bring to light new properties and effects in systems that may appear to have exhausted all possible discoveries.

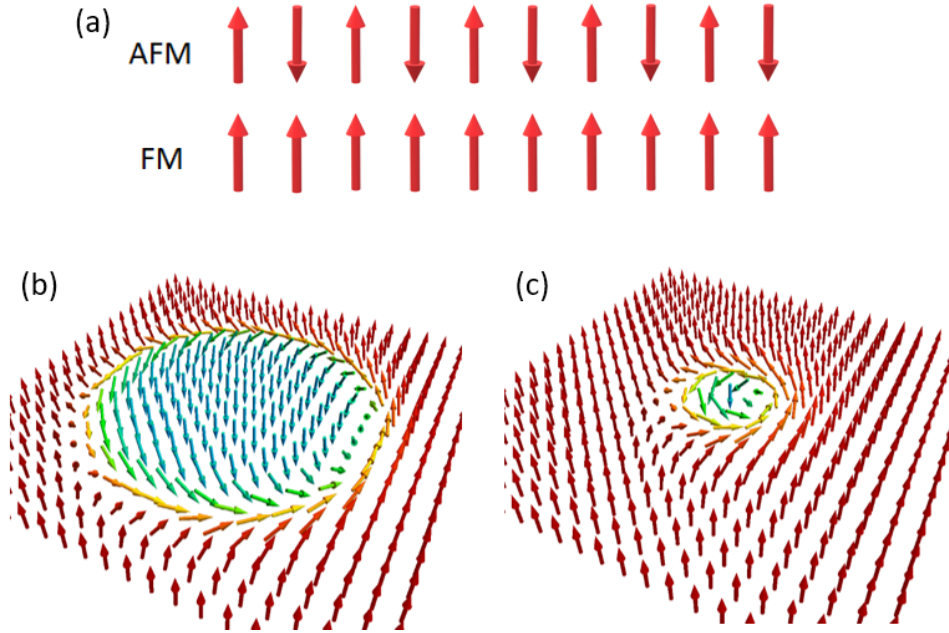


Figure 1.1: (a) Ferromagnets and antiferromagnets have magnetic configurations with different properties, due to their different symmetries, but are topologically equivalent since they are topologically trivial. An example of topologically non-trivial magnetic configurations are (b) skyrmion bubbles and (c) skyrmions (courtesy of Joo-Von Kim).

1.1.1 Magnetic skyrmions and skyrmion bubbles

The concept of topological states originated in the '60s in a paper from Skyrme [1], who tried to solve the problem of the stability of particles. Skyrme argued that particles may be topologically non-trivial, i.e. topologically distinct from vacuum. These particles are thus called skyrmions. In magnetism, topologically non-trivial states are spin configurations that require to be broken, and not bent, in order to erase them. These structures are magnetic skyrmion bubbles (Fig. 1.1b) and magnetic skyrmions (Fig. 1.1c) (throughout the rest of this thesis we will refer to these omitting "magnetic"). A skyrmion is a vortex-like spin structure around a spin aligned antiferromagnetically to the ferromagnetic background; a skyrmion bubble is vortex-like spin structure around a bubble domain, aligned antiferromagnetically to the ferromagnetic background (i.e. a bubble domain with a skyrmion-like domain wall). While these two structures arise in different conditions and have different sizes (100-1000 nm for skyrmion bubbles and 5-100 nm for skyrmions), they share most of their topological properties.

Fig. 1.2 depicts the topological structure of skyrmions and skyrmion bubbles, with the arrows representing the in-plane orientation of the spin $\vec{n}(\vec{r})$ in the position \vec{r} . The topology of these structures is quantified by the topological charge Q (also called skyrmion number) defined as the number of times the spins $\vec{n}(\vec{r})$ wrap around

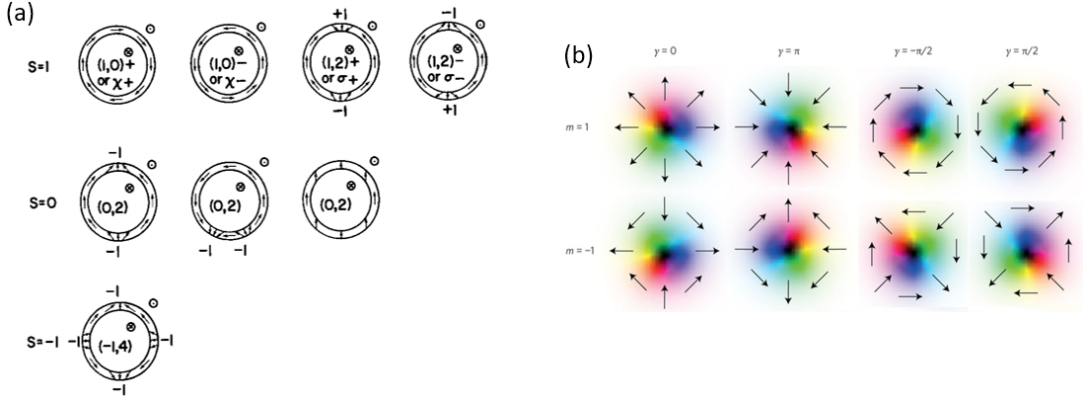


Figure 1.2: Schematic of different spin configurations in (a) skyrmions bubbles [2] and (b) skyrmions [3] for different topological charge vorticities [S in (a) m in (b)] and helicities.

the skyrimon core, or

$$Q = \frac{1}{4\pi} \int d\vec{r} \cdot [\partial_x \vec{n}(\vec{r}) \times \partial_y \vec{n}(\vec{r})] = pv \quad (1.1)$$

where $p = \pm 1$ is the polarization (out-of-plane component of the magnetization of the skyrmion core), and v is the vorticity or winding number (typically $v = \pm 1$) determined by the in-plane magnetization structure at the perimeter of the bubble, i.e. the number of revolutions the spin $\vec{n}(\vec{r})$ makes as \vec{r} revolves around the skyrmion core:

$$v = \frac{\int_0^{2\pi} d\Phi(\phi)}{2\pi} \quad (1.2)$$

where Φ is the phase of the spins at an angle ϕ from the skyrmion core [3]. Skyrmions and skyrmion bubbles are also defined by their helicity γ , i.e. the phase of the winding spins.

Skyrmions and skyrmion bubbles with various vorticities and helicities are shown in Fig. 1.2. One can note that while these structures vary, skyrmions and skyrmion bubbles with the same charge Q may have the same in-plane magnetization patterns.

1.1.1.1 Skyrmion bubbles and dipole-dipole interaction

Magnetic bubbles were extensively studied in the '70s as candidates for magnetic data storage [2]. While studying the energetics of these configurations, it was discovered that these bubble domains could feature whirling spins around their core. These magnetic bubbles are now referred to as skyrmion bubbles. The topological charge of these structures is stabilized by dipole-dipole interaction, whose energy is

$$E_{d-d} \propto \rho_{mag} \propto \vec{\nabla} \cdot \vec{n}(\vec{r}) \quad (1.3)$$

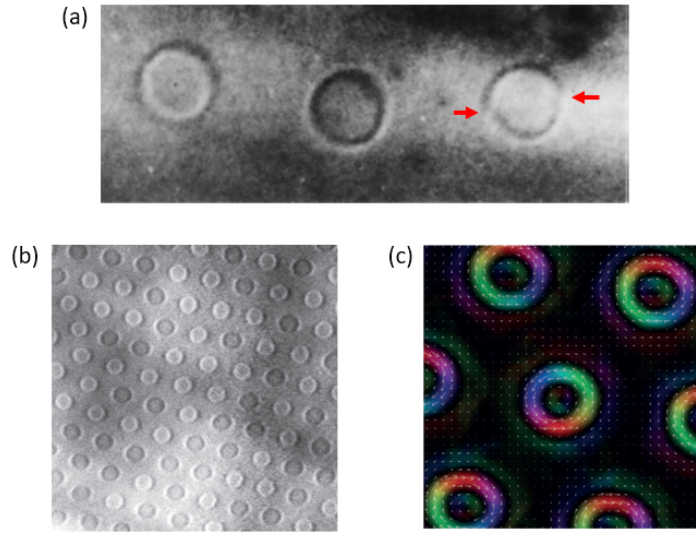


Figure 1.3: Transmission electron microscope image of bubble domains in a 300 nm thick film of $\text{PbFe}_{12}\text{O}_{19}$. The first two bubbles have winding number $v = 1$ and opposite vorticity ($\gamma = \pm\pi/2$, corresponding to the bright and dark colors), while the second one is topologically trivial [6]. In the latter, two Bloch lines can be seen by the change in contrast in the domain wall. (b) Transmission electron microscope image of $\text{BaFe}_{11.79}\text{Sc}_{0.16}\text{Mg}_{0.05}\text{O}_{19}$ showing a skyrmion lattice in a 100 mT field. Bright and dark colors correspond to the helicities $\gamma = \pm\pi/2$. (c) In-plane magnetization of the same bubbles, showing their topological character [7].

where ρ_{mag} is the magnetic charge. This energy is minimized when the spins assemble head-to-tail, reducing the magnetic charge, and forming a Bloch-like domain wall structure. In particular, skyrmion bubbles with perfect Bloch walls ($v = 1$ and $\gamma = \pm\pi/2$, the first two bubble in the first row of Fig. 1.2a) are the most energetically favored. Two of such bubbles, with opposite polarities, are shown in Fig. 1.3a. The chirality, i.e. the sign of γ , of these Bloch skyrmion bubbles is not determined by the dipole interaction and may take both values; two of such bubbles, with opposite polarities, are shown in Fig. 1.3b where bubbles with opposite vorticities are randomly nucleated in a triangular lattice.

Bloch walls can be interrupted by a Bloch line, a change in polarity of the wall. Since Bloch lines break the head-to-tail pattern of the skyrmion bubbles' domain, they have an energy cost due to strong dipole interaction. Topologically trivial bubbles must always contain at least two Bloch lines, as shown in Fig. 1.3a. Because of this, materials with strong dipole interaction tend to nucleate bubbles that are topologically non-trivial, especially when the bubbles have a small diameter (100-200 nm) which increases the domain wall energy relative to that of the domain core.

Although skyrmion bubbles fell out of popularity in the '90, now many scientists are starting to re-examine them in light of the increasing interest in topological structures. Modern techniques also allow the precise mapping of the in-plane magnetization

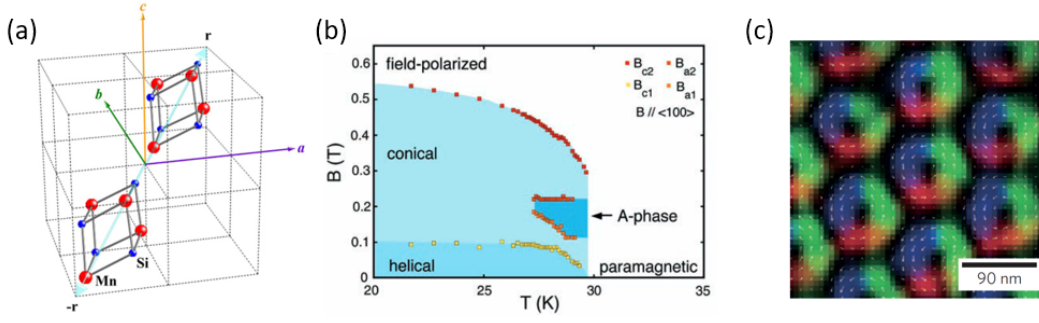


Figure 1.4: (a) Crystal structure of MnSi with B20 cubic symmetry. The lack of inversion symmetry is due to fact that inversion ($\vec{r} \rightarrow -\vec{r}$) Operation does not produce identical unit but rather its opposite. [8] (b) Magnetic phase diagram of MnSi. The A-phase is identified as the skyrmion crystal phase [9]. (c) Color map of the in place magnetization of the spins of the Fe_{0.5}Co_{0.5}Si skyrmion lattice [10].

of skyrmion bubbles and enable the visualization in real space of their topological spin structure (Fig. 1.3c).

1.1.1.2 Skyrmions in non-centrosymmetric crystals

Non-centrosymmetric materials feature lattices that lack inversion symmetry (i.e. are changed by the transformation $\vec{r} \rightarrow -\vec{r}$). One such material is MnSi with its B20 crystal lattice, pictured in Fig. 1.4a. In this case, an antisymmetric exchange mechanism called Dzyaloshinskii-Moriya interaction (DMI) arises. The energy involved in DMI, in general, follows the expression [4, 5]

$$\vec{E}_{DM} = \vec{D} \cdot (\vec{s}_1 \times \vec{s}_2) \quad (1.4)$$

where \vec{s}_1 and \vec{s}_2 are the spins involved in the exchange and \vec{D} is the DM vector that vanishes when the center between two the two spins is centrosymmetric. If \vec{s}_1 and \vec{s}_2 are initially parallel or antiparallel, the effect of a strong DMI is to introduce a tilt, with sign and magnitude depending on the sign and magnitude of d_{12} . Since in non-centrosymmetric materials there is a global breaking of inversion symmetry, this induces a global tilt in the system. As a result, by plugging Eq. 1.4 in the spin Hamiltonian of a ferromagnet, its ground state becomes a helical state with a wave vector $q = 2\pi/\lambda = D/J$, where J is the exchange integral. By applying a magnetic field, the material first transitions to a conical spin state, and, when the field is strong enough, a ferromagnetic structure is recovered. In the conical state, close to the transition temperature, there exists a fourth phase, dubbed A-phase (Fig. 1.4b). Neutron magnetic scattering experiments have shown in 2009 that the A-phase in MnSi is a skyrmion lattice [9]. This is the first experimental proof of magnetic

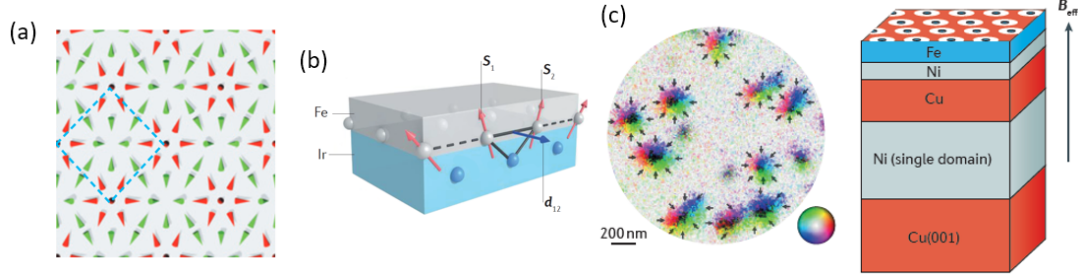


Figure 1.5: (a) Skyrmion lattice of a hexagonal Fe monolayer on Ir (111). The red and green cones represent up and down magnetization components respectively [11]. (b) Schematic of the Dzyaloshinskii–Moriya interaction at the interface between a ferromagnetic film (Fe) and a heavy metal (Ir). \vec{S}_1 and \vec{S}_2 label the spins of neighboring atoms, and \vec{d}_{12} is the corresponding Dzyaloshinskii–Moriya vector [12]. (c) Spin-polarized low-energy electron microscopy image (left) of skyrmions in an Fe/Ni bilayer in a multilayer structure such as that shown in the schematic picture (right). The skyrmions are stabilized at room temperature in zero external field through exchange with the Cu layer, which creates a virtual out-of-plane magnetic field, B_{eff} [15].

skyrmions.

Real-space skyrmion imaging is possible thanks to various microscopy techniques. One of these is Lorentz transmission electron microscopy which can measure in-plane magnetization with nm precision. The first real-space observation of skyrmions was in 2010, when Yu et al. observed a skyrmion crystal in $\text{Fe}_{0.5}\text{Co}_{0.5}\text{Si}$, another material with a B20 lattice [10]. These skyrmions are Bloch-like ($\gamma = -\pi/2$), and the uniform helicity γ is determined by the sign of the DMI.

A second candidate for crystals hosting skyrmion lattice are frustrated triangular spin lattice [13], where the frustration could stabilize a skyrmion lattice. This is appealing from a technological point of view, although there exists to this date only one experimental report of skyrmions in such systems [14].

1.1.1.3 Skyrmions in heterostructures

Different types of heterostructures feature skyrmions. The first report on this system, from 2011 [11], shows how Fe monolayer on Ir (111) feature skyrmions with diameters of a few unit cells, in a triangular lattice (Fig. 1.5a). Although the dominant cause of the formation of these skyrmions is four-spin interaction, this system presents strong DMI due to the symmetry breaking at the interface.

Interfaces inherently break inversion symmetry so, in a system comprising a ferromagnet (such as Fe) and a material with strong spin-orbit coupling (such as Ir), DMI will arise with $\vec{D} = D(\vec{z} \times \vec{u}_{12})$, where z is the unit vector perpendicular to the interface and u_{12} is the unit vector connection the two spins.

Skyrmions caused by interfacial DMI are generally stable at room temperature

since, unlike skyrmion lattices in B20 crystals whose formation strictly depends on the transition temperature of hosting material, these skyrmions originate from the interface itself and can thus be engineered from ferromagnets with high critical temperatures, such as Co or Fe. The first report of interfacial skyrmions, in Fe/Ni bilayers, are not only present at room temperature, but also at zero field, since Ni is exchange-coupled to an underlying Cu spacer which provides the field-like interaction needed to stabilize the skyrmions.

1.1.1.4 Topological devices

Skyrmions are small, stable magnetic elements whose properties are inspiring many possible applications. All of the basic functions necessary for data storage and processing have been proved possible, although not all with individual skyrmions at room temperature. The nucleation [16, 17] and annihilation [18] of skyrmions has been demonstrated, although not yet at room temperature in multilayered single skyrmion systems [20]. The motion of skyrmions can be induced by currents interacting with the skyrmions through spin transfer torque [16]. The detection of a single skyrmion has been recently proven possible by observing the transverse Hall of a sub- μm wide track as a skyrmion travels through it [19]. Possible room-temperature skyrmion devices include racetrack memories (nm-wide tracks hosting moving skyrmions that are read and written by magnetic heads) [21], logic devices and transistors [22, 23], skyrmion magnonic meta-materials [24], and skyrmion radio-frequency generators [25, 20].

1.1.2 Topology and transport phenomena

Charged quantum particles such as electrons are able to be affected by electromagnetic fields that are not present in the space where the electrons are confined. This phenomenon was first predicted by Aharonov and Bohm [26], who showed that an electromagnetic field is able to affect electrons confined in a region where both \vec{E} and \vec{B} are zero. This occurs through the coupling of the phase of the particle's wave function to the electromagnetic four-potential. The coupling adiabatically modifies the phase of the electrons, endowing it with an additional contribution every wave cycle. This additional phase is called geometrical, or Berry, phase [27], and is a central concept to the effects of topological states on electron transport.

1.1.2.1 Topological Hall effect

Similarly to the Aharonov-Bohm effect, a carrier passing through a skyrmion, skyrmion bubble, or any topological structure, will acquire a Berry phase of a flux

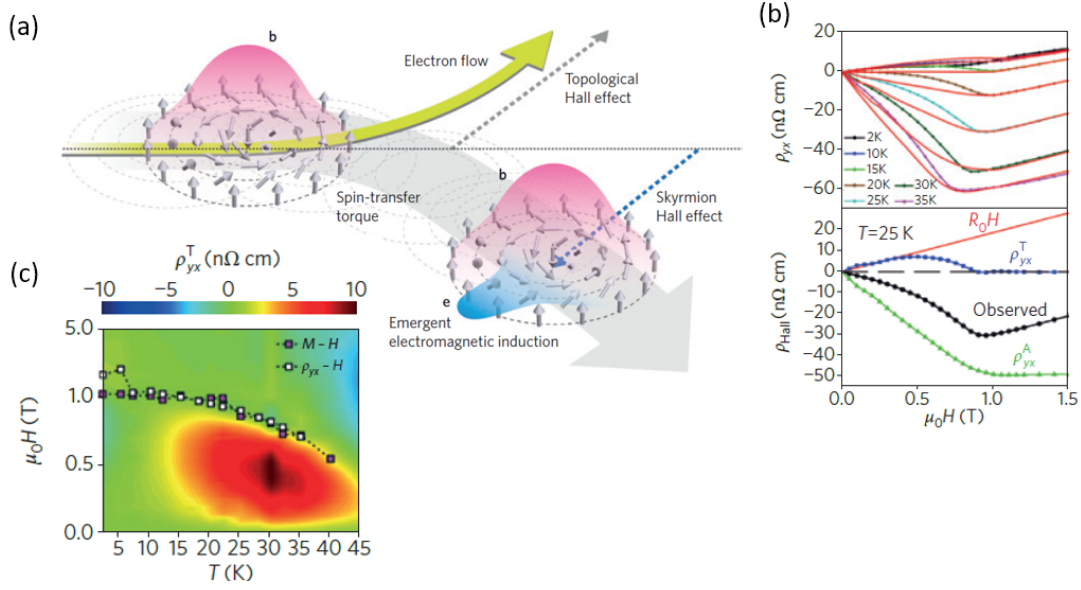


Figure 1.6: (a) Schematic picture of the effects of a current passing through a skyrmion. Electrons are deflected by and emergent magnetic field through the Lorentz force, giving rise to the topological Hall effect. Spin transfer torque will move the skyrmion and its emergent magnetic field; this causes an emergent magnetic field induction mechanism called skyrmion Hall effect. (b) Hall effect of a MnSi thin film and its decomposition of the Hall effect into normal, anomalous and topological Hall effect ρ_{xy} [29]. (c) Phase diagram of the skyrmion system obtained as the color map of ρ_{xy} [29].

quantum $\Phi_0 = h/e$ per unit of topological charge Q .¹ Due to this Berry phase the charge carriers feel an emergent magnetic field, and as a result of a fictitious Lorentz force the electron will be deflected transversally, giving rise to the topological Hall effect [3].

This effect was first predicted in 2004 [28], when Bruno and colleagues demonstrated that, with strongly coupled carriers, there will be an additional contribution to the Hall effect in the field range where skyrmions are nucleated, of magnitude

$$\rho_{THE} = \frac{P\langle b \rangle}{en} = \frac{P\sigma_{sk}\Phi_0}{en} \quad (1.5)$$

where P is the spin polarization, $\langle b \rangle = \sigma_{sk}\Phi_0$ is the emergent magnetic field and σ_{sk} is the skyrmion density.

The first report of a topological Hall effect from a skyrmion system is from 2009 when Neubauer and colleagues reported a topological Hall effect with an amplitude of 4.5 n Ω cm in a 50 nm MnSi thin film (Fig. 1.6b) [30, 29]. The skyrmion phase diagram can be extracted from these measurements, showing the skyrmions appearing in a

¹This magnetic flux quantum is defined differently from that of superconductors ($\Phi_0 = h/2e$), where the Cooper pairing doubles the charge and thus halves the flux

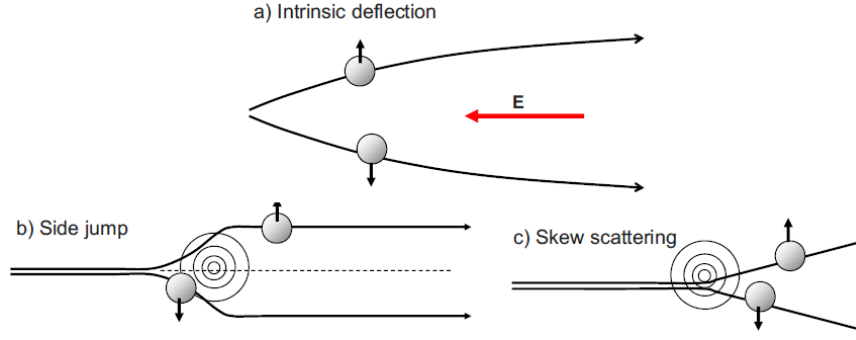


Figure 1.7: Illustration of the three main mechanisms that can give rise to an anomalous Hall effect [35].

pocket of magnetic field slightly below the transition temperature (Fig. 1.6c). This is comparable to the phase diagram extracted from neutron scattering experiments (Fig. 1.6b), proving how the topological Hall effect can be a powerful tool to detect topological structures.

It should be noted that not only skyrmions and skyrmion bubbles may cause topological Hall effect, as chiral spin structures may give rise to Berry phases and thus topological Hall effect. For example, the fan spin structure present in MnP causes a topological Hall effect, driven by the spin chirality of the magnetic structure [31].

1.1.2.2 Anomalous Hall effect

The anomalous Hall effect is one of the oldest magnetotransport phenomena observed in condensed matter, having been discovered by Edwin H. Hall himself who noticed that the pressing electricity (now called Hall voltage) of a ferromagnet was one order of magnitude larger than in non-magnetic conductors [32]. More than half a century later, it was shown that this anomalous Hall effect is proportional to the magnetization of the sample [33]:

$$\rho_{xy} = R_0 H + R_S M. \quad (1.6)$$

The first theory of anomalous Hall effect [34] showed that, by applying an electric field, electrons may gain an "anomalous velocity" perpendicular to the electric field, accumulating at the sides of the conductor and causing the anomalous Hall effect. The concept of anomalous velocity has now been superseded by the Berry curvature (defined as Berry phase per unit area in reciprocal space), to which it is proportional.

There are different mechanisms that can produce a Berry curvature in electrons. The first mechanism proposed is the intrinsic deflection, a band-dependent contribution, independent of impurities, arising in a perfect crystal. Later theories showed

that a Berry curvature can be also acquired through extrinsic mechanisms: asymmetrical skew scattering from impurities [37], and by deflection from spin-orbit coupled impurities [38]. These mechanisms are shown in Fig. 1.7.

Although it was not clear from the start, the intrinsic anomalous Hall effect is an inherently topological process. When the first theories were formulated, the concept of Berry phase was not known and the precise mathematical interpretation of the anomalous velocity could not be obtained. However we now know that the geometrical phase effects present in any anomalous Hall mechanism stem from the topology of the space, be it reciprocal or real, where the electrons are confined. This topological interpretation was stressed by Onoda and Nagaosa [36], who showed that the Bloch states causing the intrinsic anomalous Hall effect are characterized by a topological Chern number, and the anomalous Hall effect occurs when this number is non-zero.

It should also be pointed out that the theory of topological Hall effect [28] originated in the scientific discussion on the theory of anomalous Hall effect, since topological and anomalous Hall effect can be both seen as the manifestation in electron transport of the Berry phase.

1.2 Perovskite manganites

Perovskite manganites are a class of materials known for hosting a wide range of phenomena (metal-insulator transition, diverse magnetic orders, half-metallicity). These materials are also remarkably sensitive to stimuli (strain and interface engineering, magnetic and electric field, and even doping), making them ideal candidates for engineering and then studying physical phenomena in the materials realm.

Interest in manganites sparked in the '50s with the discovery of the colossal magnetoresistance, but faded since the magnetic field needed to exploit this effect were too large. In the following decades, as spintronics began to develop, this class of materials was studied for its peculiar characteristic of being a half-metal [39], meaning that at the Fermi level only one electron spin state has a non-zero density of states and so the current is 100% spin polarized.

These materials also feature very rich phase diagrams with doping, exhibiting metal-insulator transitions, ferromagnetic-antiferromagnetic transitions that give birth to non-coplanar spin texture, coupling with bosons, and charge- and orbital- ordering. Additionally, close to the metal-to-insulator transition strong correlations are present and strongly depend on doping and strain. These electronic, magnetic and ordering phenomena can depend on one another, and this interplay can be observed with the help of the strong tunability of this phenomena.

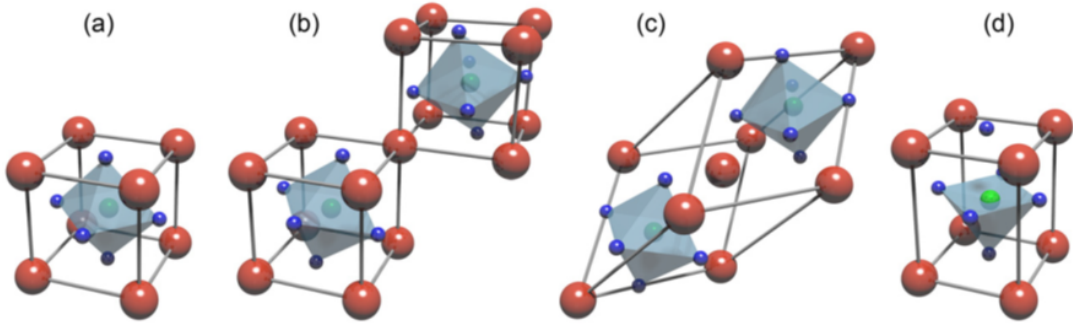


Figure 1.8: Cubic perovskite crystal unit cell (a) of an ABO_3 compound, with (b) orthorhombic, (c) monoclinic, and (d) tetragonal distorted unit cells [126]. In a $R_{1-x}M_xMnO_3$ perovskite manganite, the blue corner atoms are Mn atoms, the green body centered atoms are dopants (R and M) and the red face centered atoms are O. This crystal structure takes the name from the mineral $CaTiO_3$, called perovskite.

1.2.1 Crystal structure and electronic configuration

1.2.1.1 The perovskite unit cell

Manganites typically have a $R_{1-x}M_xMnO_3$ ($0 < x < 1$) chemical structure, where R typically is a rare earth material (e.g. La) and M typically is an alkaline earth metal (e.g. Ca, Sr). They crystallize in the perovskite ABO_3 structure, pictured in Fig. 1.8a. The perovskite unit cell comprises, in its center, a B cation enclosed in an oxygen octahedron and, at the corners, an A cation. This structure, in its most basic form, is purely cubic, and its stability depends on the delicate balance between ionic radii of the A and B cations. Both radii need to be large enough to accommodate the bond with the oxygen ions, but if the ionic radius of A is too large, the oxygen octahedron is excessively strained and the crystal structure collapses; the ionic radius of B, on the other hand, if larger than that of A, distorts the oxygen octahedron which starts to tilt under strain, reducing symmetry, and if this distortion is too large, the crystal structure is again not stable.

This is formalized by the tolerance factor (or Goldschmidt factor) [40, 41]

$$t = \frac{r_A + r_O}{\sqrt{2}(r_B + r_O)}, \quad (1.7)$$

which represents the balance between the radii of the A and B cations, and thus between the A-O and B-O bonds. When $t = 1$ and the unit cell is cubic, but if $t \neq 1$ the unit cell can be compressed and deformed and the oxygen octahedron can undergo tilts and rotation:

- $t > 1$ the unit cell is hexagonal
- $1 > t > 0.9$ the unit cell is cubic

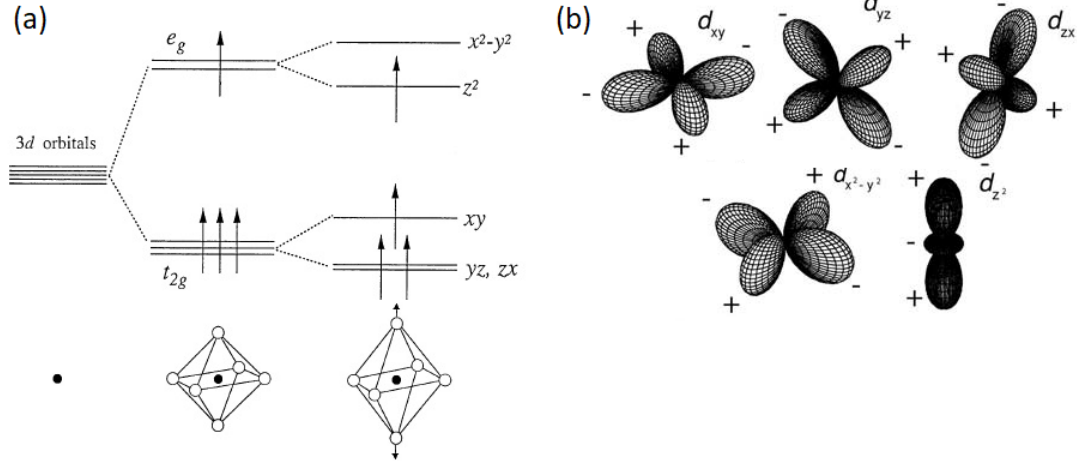


Figure 1.9: (a) Energy levels of 3d orbitals in vacuum, split by crystal field (first splitting) and then by Jahn-Teller effect with elongation along z (second splitting) [44]. (b) 3d electron orbitals [42].

- $0.9 > t > 0.8$ the unit cell is rhombohedral
- $0.8 > t > 0.7$ the unit cell is orthorhombic
- $0.7 > t$ the structure is not a perovskite (e.g. ilmenite or corundum)

These ranges are valid only for bulk materials, as in thin film the substrate strain also influences the crystal structure.

1.2.1.2 Crystal field splitting and Jahn-Teller effect

The electronic configuration of a perovskite manganites is highly sensitive to its crystalline structure due to Coulomb interaction with the surrounding charges. In vacuum, the valence electrons of a Mn ion are in the 3d orbitals, which are degenerate. However, when this Mn ion is in the octahedrally-coordinated B site of the perovskite unit cell, the different symmetries of the different will have different energies due to the non-uniform environment (Fig. 1.9). Here, the 3d orbitals split into the lower t_{2g} triplet (xy , yz , and zx , which have less overlap with the oxygen p electrons) and the upper e_g doublet ($x^2 - y^2$ and z^2 orbitals, which have more overlap with the neighboring oxygen p electrons). This is called crystal field splitting.

The electronic structure depends on the crystal structure, but the opposite is also true. If we imagine the oxygen octahedron elongating along z (by 2δ) and contracting along x and y (by δ), preserving its volume, then the $x^2 - y^2$ and xy increase their overlap with the oxygen electrons, and increase their energy by 3Δ . Meanwhile, the z^2 , yz , and zx orbitals decrease their overlap with the oxygen electrons, decreasing their energy by 2Δ for z^2 and Δ for yz and zx . If there are three, or five, electrons in the 3d orbitals, the net change in energy due to this distortion is zero, but if the 3d electrons are four, there is a net decrease in energy of Δ (Fig. 1.9). This means that

this distortion is self-stabilized by the decrease in potential energy that it brings, and thus appears spontaneously. This is called Jahn-Teller effect [45]. By these means, it is not possible to predict the direction of the elongations and contractions, but we can only predict that the undistorted system is unstable.

In the single valence manganites like LaMnO_3 , Mn is in the 3+ oxidation state, which has a $3d^4$ valence configuration. Thus, LaMnO_3 is uniformly Jahn-Teller distorted. In the case of mixed-valence manganites, the situation is a bit more complex. Since the degree of Jahn-Teller effect depends directly on the valence of Mn ions, if there is more than one valence state then the Jahn-Teller distortion becomes distributed non-uniformly. If the charge carriers are associated to a valence state that favors Jahn-Teller effect (e.g. 3+), then, as they move through the material, they carry Jahn-Teller distortions with them. If, on the other hand, the charge carriers are associated to a valence state with no Jahn-Teller effect (e.g. 4+), then they remove Jahn-Teller distortions as they travel. Thus, charge carriers in mixed-valence manganites tend to be strongly interacting with Jahn-Teller distortions.

1.2.1.3 Correlations and metal-insulator transitions

The Mn ions in manganites typically have an oxidation state between 2+ and 4+, meaning that their valence varies between $3d^3$ and $3d^5$. Their 3d orbitals are half-filled, and conventional band theory would argue that they are conductors. However, all single-valence manganites are insulators [47]. This is due to electron-electron interactions (and crystal-field splitting), which are not considered by conventional band theory.

The theory to account for static correlations was developed by Mott and Hubbard [48, 49]. In the Mott-Hubbard model, a Coulomb repulsion term is added to the-tight binding Hamiltonian:

$$H = \sum_i \epsilon_i \hat{n}_i - t \sum_{ij} \left(\hat{c}_i^\dagger \hat{c}_j + \hat{c}_j^\dagger \hat{c}_i \right) + U \sum_i (\hat{n}_{i\uparrow} \hat{n}_{i\downarrow}) \quad (1.8)$$

where the first term in the potential orbital energy, the second is the kinetic energy, and the third is electron-electron Coulomb repulsion. U is the Hubbard parameter and is the energy necessary to transfer a 3d electron to a neighboring Mn 3d orbitals.

If U is small, the conventional tight binding Hamiltonian is recovered. The cutoff value for U is the bandwidth W of the valence 3d electrons: if $U \gg W$ then a bandgap is opened in the otherwise half-filled d band, and the system becomes insulating. This is represented schematically in Fig. 1.10a: if U is large enough the electrons are not able to delocalize due to the presence of the other repelling electrons, and become localized in the Mn ions. In this condition, the material is called a Mott-Hubbard insulator.

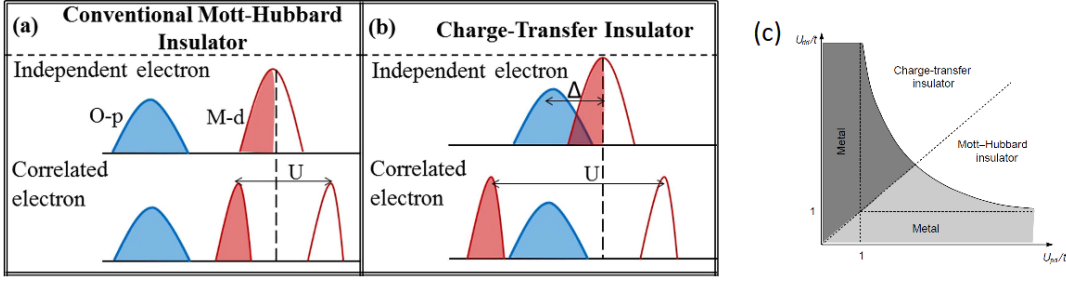


Figure 1.10: (a,b) Schematic illustration of different correlation effects leading to insulating behavior in otherwise conducting manganites. [46]. (c) Zaanen-Sawatzky-Allen phase diagram of different Mott insulators [42]. U_{dd} is the on-site Hubbard U and U_{pd} is the charge transfer energy Δ_{ct} , while t is the hopping integral which in this case it is assumed to be equal to the bandwidth W .

In manganites, U is in the 5 – 10 eV range while $W \approx 1$ eV [47], putting them in the strongly correlated $U \gg W$ regime. However, some manganites such as CaMnO_3 are not well represented by this model as their valence band also comprises O 2p electrons. This is because the Mott-Hubbard model does not take into consideration the hybridization between Mn 3d and O p electrons orbitals.

The Mott-Hubbard formalism is generalized in the framework of Mn-O orbital hybridization by the d-p model [50], which was formulated in order to explain how high- T_C superconductors have hole carriers in the O 2p orbitals, in the presence of strong correlations. In this model there are two interactions; one between localized Mn 3d ions, described in Mott-Hubbard model and represented by the parameter on-site Hubbard U ; the second is the interaction between Mn 3d electrons and their neighboring O 2p electrons, represented by the parameter Δ_{ct} , the charge transfer energy, which is the energy necessary to transfer an electron from an occupied O 2p orbital to a neighboring Mn 3d orbital.

If $U < \Delta$, the previous Mott-Hubbard insulator is recovered, where, in their ground state, the electrons remain fully localized. However, if $U > \Delta$ then charge transfer becomes the dominant, lowest-energy excitation. These materials are called charge-transfer insulators, where electrons are able to hop between Mn 3d and their hybridized O 2p orbitals, but not to another Mn ion.

A directly measurable consequence is that the band gap of a charge-transfer insulator is opened between O 2p and Mn 3d orbitals, while that of a Mott-Hubbard insulator is opened between only Mn 3d orbitals (Fig. 1.10a,b). The phase diagram of the electronic phase of a material as a function of U and W .

Single-valence manganites exhibit some kind of insulating behavior since their associated U and Δ values are greater than their bare bandwidth W . This is because, owing to their small carrier density, there is little electron-screening. In mixed-valence manganites, the carrier density is increased and electron screening increases. In this

situation, the screened Coulomb interaction becomes

$$U(r) = U_0(r) \exp(-r/\lambda_s) \quad (1.9)$$

where $U_0(r)$ is the unscreened potential and $\lambda_s \approx a_0^*/4n^{1/3}$ is the Fermi-Thomas screening length, with a_0^* the Bohr radius and n the carrier density [51]. The Coulomb interaction becomes negligible for values of carrier densities above the Mott criterion:

$$n^{1/3}a_0^* = C \quad (1.10)$$

where C is a constant, according to various estimates, in the 0.2 – 1 range. Thus, as mixed-valence manganites reach this critical carrier density value, a metal-insulator transition is achieved.

Correlations are not the only mechanisms that opens the band gap in manganites, and oxides in general. In perovskite oxides, the ubiquity of structural distortions (both cubic or orthorhombic crystal-field splitting, or Jahn-Teller distortions) also implies a splitting of the 3d levels, opening band gaps [52]. While this implies that the Mott-Hubbard model is not necessarily the key to justifying why these materials are insulating, it does not imply that correlations are not present. Static correlations are always present (as they are the mechanism behind crystal-field splitting and Jahn-Teller distortions), and dynamical correlations may also be at play in other mechanisms. The role of correlations in transport in manganites will be described in 1.2.3.2

1.2.2 Magnetic structure and properties

The magnetic configuration of manganites relies on exchange mechanisms, beyond the simple Heisenberg exchange interaction, and strongly depends on the crystal structure and orbital occupancy of the Mn ions.

1.2.2.1 Single-valence manganites and superexchange

Single-valence manganites are insulators where electrons are localized and there is negligible overlap between the wave functions of electrons in different Mn ions, so simple Heisenberg exchange does not occur. Mn 3d and O 2p orbitals hybridize and so, as Mn atoms hybridize with the same O ion, the latter ion acts as a bridge and allows for exchange interaction between the electrons in the orbitals of the two Mn ions.

This is a second order process where the total energy of the interaction is the energy required to form an excited state through virtual hopping of two electrons [53, 54]. Fig. 1.11 depicts these excited states, for both ferromagnetic and antiferromagnetic ordering. It can be easily seen that the ferromagnetic configuration produces excited

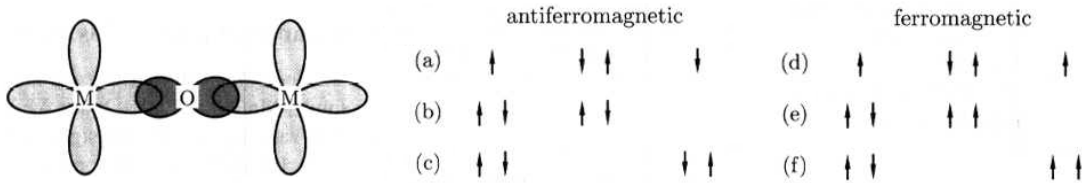


Figure 1.11: Superexchange interaction: in the antiferromagnetic case, the ground state is (a). The excited states, produced by the virtual hopping of two electrons, to which the ground state couples are (b) and (c); in the ferromagnetic case the ground state is (d) and excited state produced by virtual hopping of two electrons are states forbidden by the Pauli exclusion principle. [43]

state with high energy prevented by the Pauli exclusion principle, while the antiferromagnetic configuration excites states with lower energy. Thus, antiferromagnetism tends to be the preferred magnetic order in single-valence insulating manganites such as CaMnO_3 or LaMnO_3 .

The above argument is based on the assumption that magnetism arises from a single, unpaired electron. This is not always the case, but more complicated situations can be dealt in a similar manner. This is summarized in the Goodenough-Kanamori empirical rules:

1. When the Mn cations have singly-occupied $3d$ orbitals with a M-O-M bond angle of 120° - 180° , superexchange is strongly antiferromagnetic.
2. When the Mn cations have singly-occupied $3d$ orbitals and the M-O-M angle is 90° , superexchange is weakly ferromagnetic.
3. When the overlap is between an singly-occupied orbital and an unoccupied or double occupied orbital, superexchange is weakly ferromagnetic.

Rules (2) and (3) are rarely applied in manganites, where normally the insulating state of single-valency is antiferromagnetic.

1.2.2.2 Mixed-valence manganites and double exchange

Mixed-valence manganites, unlike the single-valence ones, possess ferromagnetic and metallic phases. Here, the A-site cations are not all of the same species, making the Mn cations not all of the same oxidation state. Thus, instead of superexchange, which requires single valence, double exchange arises as the dominant interaction. As in the case of superexchange, there is no direct coupling between the magnetic $3d$ orbitals, and we can treat the mechanism as a second-order process due to the hybridization and overlap to O $2p$ orbitals [55]. The total energy of the interaction is the energy required to form an excited state through hopping of one electron from one Mn ion to another, through the O ion.

In Fig. 1.12 we see the possible double exchange mechanism for ferromagnetic and antiferromagnetic configurations between the $3d^4$ -occupied Mn^{3+} and $3d^3$ -occupied

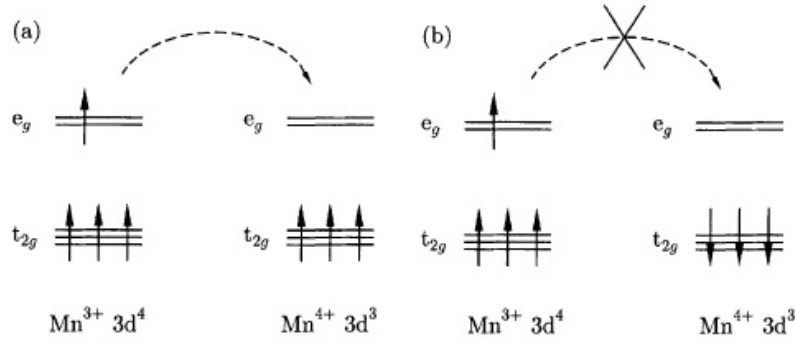


Figure 1.12: Double exchange interaction: (a) if the two Mn ions are ferromagnetically aligned, then the e_g electron can freely hop from Mn^{3+} to Mn^{4+} , passing through the connecting O ion; (b) if the two Mn ions are not ferromagnetically aligned, then the e_g electron would need to change spin direction to conform with Hund's rules, and thus cannot hop as to do so it would have to pass a high energy barrier. [43]

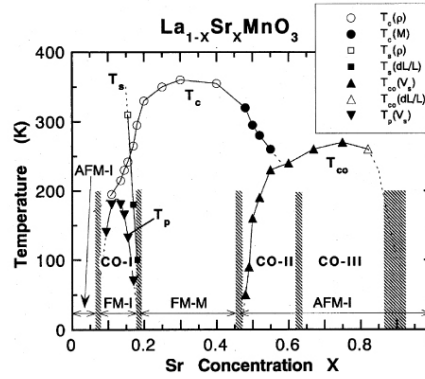


Figure 1.13: $\text{La}_{1-x}\text{Sr}_x\text{MnO}_3$ phase diagram shows that transport and magnetic properties are function of Sr ions fraction. In the range $0.2 < x < 0.5$ the compound becomes ferromagnetic and metallic, under a Curie temperature near room temperature, due to double exchange [56]

Mn^{4+} . If the ions are aligned ferromagnetically, then an electron from the Mn^{3+} ion is able to hop to the Mn^{4+} ion, through the O ion. If the ions are aligned antiferromagnetically, then this electron will feel a strong potential energy from the Hund coupling (typically 2 eV in manganites [42]). Unlike superexchange, these hopping states are not virtual but are the hopping mechanism that allows the conducting electron on the Mn^{3+} ion to move. Thus, ferromagnetism arises because it allows the electrons to delocalize, reducing the kinetic energy of the system which allowed to be metallic.

Double exchange is the reason why in manganites, metal-insulator transitions are normally accompanied by ferromagnetic-antiferromagnetic transitions. For example, $\text{La}_{1-x}\text{Sr}_x\text{MnO}_3$, where a fraction x of the Mn ions are Mn^{4+} , and $1 - x$ are Mn^{3+} . When $x = 0$, the material is simply LaMnO_3 , a single-valence, insulating antiferro-

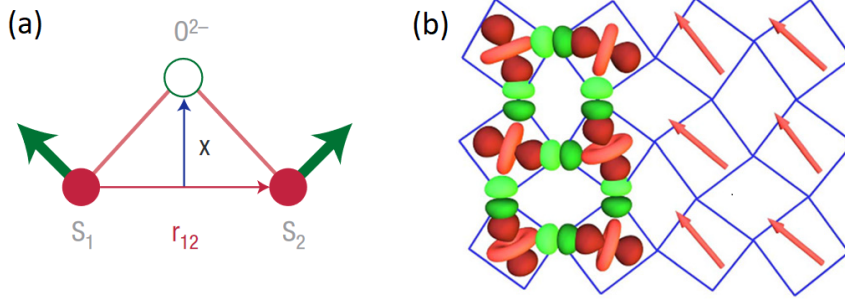


Figure 1.14: (a) [57] (b) Mn 3d and O 2p orbitals (left) and Mn spin orientation (right) of LaMnO_3 (composed of ferromagnetically-ordered planes antiferromagnetically coupled with each other) [58].

magnetic. As x increase, so does the carrier density, which gets closer to the critical value of the Mott transition (Eq. 1.10), and at $x = 0.175$ the material transitions to a metallic and ferromagnetic state, due to double exchange dominating over superexchange (see Fig. 1.13).

Double exchange can also occur in systems that are not fully ferromagnetic but rather canted antiferromagnets, magnetic systems can arise due to competition between different interactions, including double exchange [121]. Weak ferromagnets are a kind of canted antiferromagnets where the dominant magnetic order is antiferromagnetic but the spins are all canted uniformly in one direction, due to double exchange, giving the whole material a net magnetization [120, 119].

1.2.2.3 Dzyaloshinskii-Moriya interaction

In 1.1.1.2 we showed how the Dzyaloshinskii-Moriya interaction (DMI) stabilizes skyrmions in systems with global inversion symmetry breaking. However, DMI theory originated to explain spin canting in antiferromagnets with spin-orbit coupling and local symmetry breaking [4, 5]. The energy involved follows the expression

$$\vec{E}_{DM} = \vec{D} \cdot (\vec{s}_1 \times \vec{s}_2) \quad (1.11)$$

where \vec{s}_1 and \vec{s}_2 are the spins involved in the exchange and \vec{D} is the DM vector, which vanishes when the center between the two spins is centrosymmetric (i.e. that point has some kind of inversion symmetry).

In a superexchange material, DMI can occur if the Mn-O-Mn angle is not flat, locally breaking the inversion symmetry. In this case, represented in Fig. 1.14a, there is a DM vector

$$\vec{D} = \vec{r}_1 \times \vec{r}_2 = \vec{r}_{12} \times \vec{x} \quad (1.12)$$

where the vectors involved are shown in Fig. 1.14a. This interaction results in a canting is typically around 1° . This can occur both in antiferromagnets, resulting in

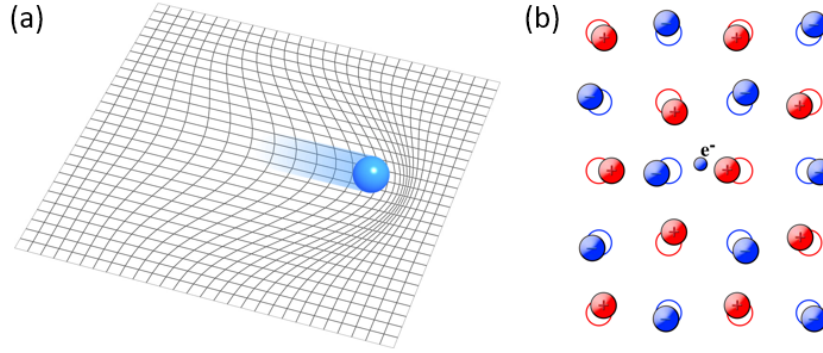


Figure 1.15: (a) Representation of polaronic motion in a crystal. (b) Representation of the electron-phonon interaction behind the formations of polarons. Courtesy of Olivier D’Allivy Kelly.

either a small ferromagnetic component or in an additional antiferromagnetic ordering in a secondary orientation. This is shown in 1.14a: LaMnO_3 has a dominant A-type antiferromagnetic dominant magnetic order (ferromagnetically-aligned planes antiferromagnetically aligned with one another). In addition to this antiferromagnetism, the tilt of the oxygen octahedra surrounding the Mn ions gives rise to DMI that cants the spins, forming a secondary antiferromagnetic order.

The role of the symmetry breaking needs to be clarified. For the DMI to exist (i.e. $\vec{D} \neq 0$) the center between the two magnetic ions needs to be non-centrosymmetric. This does not imply lack of centrosymmetry of the material, as *local* symmetry breaking can give rise to a *local* DMI. The tilt of the oxygen octahedra (Fig. 1.14b) breaks the symmetry only locally, although globally $\sum_i \vec{D}_i = 0$, as one should expect in a centrosymmetric material such as LaMnO_3 . For the DMI to be global ($\sum_i \vec{D}_i \neq 0$), there needs to be global symmetry breaking that occurs in non-centrosymmetric crystal structure, or at interfaces in multilayers (containing both materials with magnetic exchange ordering and strong spin-orbit coupling).

1.2.3 Electronic properties and transport

1.2.3.1 Polarons and electronic transport

First attempts to model the transport properties only used double exchange, the tendency to hop while maintaining a ferromagnetic configuration. However, double exchange alone does not explain the transport behavior of manganites [60], in particular in this model there is no mechanism to explain how the kinetic energy of the carriers can decrease around the transition temperature T_C , driving the metal-insulator transition [59]. One proposed mechanism that could drive the transition is polarons: quasiparticles formed by carriers that, as they move around the material, they drag

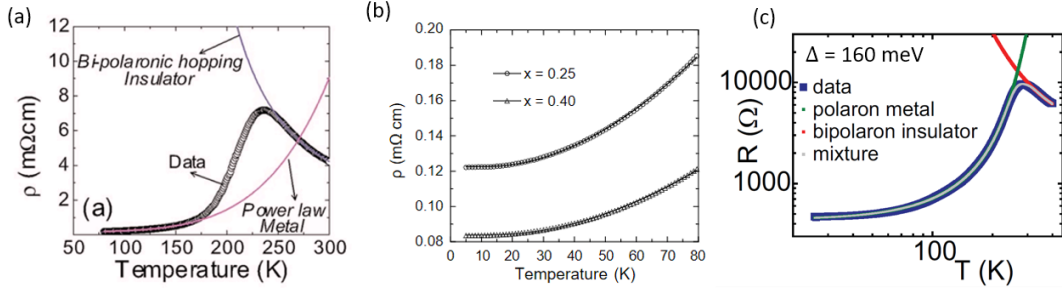


Figure 1.16: (a) Temperature dependence of generic $\text{La}_{2/3}\text{Ca}_{1/3}\text{MnO}_3$ data. Solid lines indicate the extrapolated fits at low temperatures to a $\rho + \rho_2 T^2 + \rho_5 T^5$ power law and at high temperatures to bipolaronic hopping model [67]. (b) Low-temperature resistivity of $\text{La}_{1-x}\text{Ca}_x\text{MnO}_3$ films. The solid lines are fitted curves [78]. (c) Resistivity of a $\text{La}_{0.67}\text{Ca}_{0.33}\text{MnO}_3$ thin film, fitted with a polaron-bipolaron model [81].

along coupled lattice distortions which reduce the carriers' mobility. As phonon occupancy increases with temperature, so does the number of coupled phonons, decrease the mobility of the polaron. At the transition temperature, the coupling to phonons increases to the point that the carriers slow down and localize, bringing about a metal-insulator transition, and consequently a magnetic one, at the transition temperature $T_C \approx \hbar\omega_0/2k_B$, where $\hbar\omega_0$ is the energy of the dominant phonon mode [71].

The existence of polarons has been confirmed by thermal measurements [61], optical conductivity [62] and reflectivity [63], angle resolved photoelectron spectroscopy [64] and neutron scattering [65]. However, there are still open questions about these polarons, for example regarding their magnetism and size. We will focus on their effects on the electric transport of thin manganite films.

Early attempts at fitting the resistivity of the low temperature metallic resistivity of CMR manganites used a polynomial [66, 68, 69]

$$\rho(T) = \rho_0 + \rho_2 T^2 + \rho_5 T^5. \quad (1.13)$$

Where ρ_0 represents impurity scattering, $\rho_2 T^2$ electron or magnon scattering and $\rho_5 T^5$ phonon scattering. The T^2 power law has been initially interpreted as electron-electron scattering. However, the electron-electron resistivity parameter ρ_2 is related with the coefficient of the electronic specific heat γ by the Kadowaki-Woods relation $\rho_2/\gamma^2 \approx 1 \times 10^{-5} \mu\Omega \text{ cm (mole K/mJ)}^2$ [70]. The ρ_2 parameters obtained with this approach are however two orders of magnitude higher than what one would expect from this relation [72], indicating that this scattering mechanism is in fact due to magnons. There are also issues with interpreting T^2 as a magnon scattering power law, since it arises from a one-magnon process. Manganites like $\text{La}_{1-x}\text{Sr}_x\text{MnO}_3$ are half metals, meaning that the minority spin state has a zero DOS at the Fermi energy E_F [39]. The bottom of the minority spin state is 350 meV from E_F [73], making one-

magnon scattering mechanisms unlikely. The T^5 electron-phonon scattering terms also raises many problems. First of all, imposing this power law makes this polynomial applicable only in small temperature ranges (see Fig. 1.16a). This power law is also obtained for the case of simple non-interacting electrons with a spherical Fermi surface, which is not the case for manganites (we will report these findings in 1.2.3.3). The value of ρ_5 is also two orders of magnitude smaller than in metals, pointing out further the fact that this power law is not applicable in manganites as it ignores the polaronic character of the carriers.

A second approach, suggested by Kubo and Ohata [74], substitutes the latter term T^5 with $T^{4.5}$:

$$\rho(T) = \rho_0 + \rho_2 T^2 + \rho_{4.5} T^{4.5}. \quad (1.14)$$

This expression retains the same problems that arise from the use of the T^2 term, whereas introducing the two-magnon scattering power law $\rho_{4.5} T^{4.5}$ further neglects polaronic effects by completely ignoring electron-phonon interaction. Fits using this expression can be done by imposing a limited temperature range, as in the previous case, and the obtained coefficient $\rho_{4.5}$ is too small to be physically meaningful [68, 81].

Other attempts include using a generic T^α term [75], with no clear physical meaning, and a Bloch-Grüneisen expression [76], which worked only at low temperatures for thin films [77].

The first attempts at using polaron theory to model the resistivity of manganites was from Zhao and colleagues [78, 79]. According to theory [80], the electron-phonon scattering rate in the presence of strong electron-phonon coupling is

$$\frac{1}{\tau} = \sum_{\alpha} \frac{A_{\alpha} \omega_{\alpha}}{\sinh^2(\hbar \omega_{\alpha} / 2k_B T)} \quad (1.15)$$

where A_{α} a constant that depends on the conduction band width and the strength of the electron-phonon interaction, $\hbar \omega_{\alpha}$ is the energy of the phonons, and the sum is across all optical phonon modes. Due to the strong inverse proportionality between the factor $1/\sinh^2(\hbar \omega_{\alpha} / 2k_B T)$ and ω_{α} , the above expression can be approximated

$$\frac{1}{\tau} \approx \frac{A_0 \omega_0}{\sinh^2(\hbar \omega_0 / 2k_B T)} \quad (1.16)$$

for the softest coupled phonon mode, with energy $\hbar \omega_0$. The temperature dependence of the resistivity becomes

$$\rho(T) = \rho_0 + \frac{E \omega_0}{\sinh^2(\hbar \omega_0 / 2k_B T)} \quad (1.17)$$

where the prefactor E contains the effective mass of the polarons. This model accurately fits the data of $\text{La}_{1-x}\text{Ca}_x\text{MnO}_3$ thin films, as shown in Fig. 1.16b, al-

though in a limited temperature range. The obtained phonon modes have energies $\hbar\omega/k_B \approx 100 - 130$ K, much lower than what one would expect from a transition temperature $T_C \approx \hbar\omega/2k_B \approx 200 - 250$ K.

This model fails to account for the temperature-dependent effective mass enhancement. As the temperature increases, so does the occupancy of phonon modes coupled to the polaron, decreasing its mobility and increasing its mass. In the Sewell model [82], used for strong coupling, the effective mass increases exponentially with temperature:

$$m^* = m_0 \exp[g^2 \coth(\hbar\omega_0/2k_B T)]. \quad (1.18)$$

Here m_0 is the bare carrier mass, g^2 the zero-temperature band narrowing factor and $\hbar\omega_0$ the energy of the softest coupled phonon mode.

The first (and to our knowledge, the only) model containing the polaronic character of carrier able to fit the metallic phase of manganites up to the transition temperature T_C is from Graziosi and colleagues [81], who included electron-magnon scattering, electron-phonon scattering in the presence of strong electron coupling (Eq. 1.16) and polaronic mass enhancement (Eq. 1.18). The resulting resistivity is

$$\rho(T) = \rho_0 + \rho_2 T^2 + \rho_{e-ph} \frac{1}{\sinh^2(\hbar\omega_0/2k_B T)} \exp[g^2 \coth(\hbar\omega_0/2k_B T)]. \quad (1.19)$$

This equation is able to fit a variety of manganites, with values in good agreement with literature. We note, however, that the T^2 electron-magnon scattering term was obtained heuristically by linearizing the $\rho(T)$ curve at low temperatures, even though it arises from a scattering process that is not allowed in half-metallic manganites. In the presence of strong on-site Hund interaction, electronic spin-waves are coupled ferromagnetically to the spin waves of the localized moments (composite spin-waves). In this picture, one-magnon scattering processes are allowed and should produce a $T^{1.5}$ dependence of the resistivity [157].

Most manganites feature an insulating paramagnetic phase upon heating above the transition temperature. In polaron theory, this is due to the electron-phonon coupling, whose strength increases with temperature, eventually reducing the mobility of the polarons. The electronic nature of this latter state is not yet entirely clear. Charge carrier density collapse (CCDC) theory posits that the transition is driven by the competition between double exchange, which delocalizes the carriers, and electron-phonon coupling, which localizes the carriers. As the temperature increases, electron-phonon interaction becomes stronger and ultimately binds two different polarons into a bipolaron, which are the dominant carriers in the high temperature phase. In this regime the resistivity is

$$\rho = \rho_0 T \exp\left(-\frac{\Delta}{2k_B T}\right) \quad (1.20)$$

where Δ is the bipolaron binding energy. Single crystals and thin films thicker than 40 nm may exhibit metal-metal insulator [81, 83], although the nature of this paramagnetic metal is not well understood.

Two models representing the ferromagnetic and paramagnetic phase can be combined into one single expression [158]

$$\rho(T) = \rho_F^{f(T)}(T) \cdot \rho_P^{f(T)}(T) \quad (1.21)$$

where $\rho_F(T)$ is the fit of the low ferromagnetic phase, $\rho_P(T)$ the fit of the high temperature paramagnetic phase, and

$$f(T) = \left\{ \frac{1}{2} \left[1 - \operatorname{erf} \left(\frac{T - T_C}{T} \right) \right] \right\}^\varsigma \quad (1.22)$$

represent the fraction of the ferromagnetic phase, with ς is the non-ideality exponent [81] that takes into account the possible phase separation known to happen in transitions in manganites [162, 164].

1.2.3.2 Mass enhancement

Polarons have their mass enhanced by electron-phonon interaction. The effective mass computed by Sewell (Eq. 1.18), obtained from tight binding computations, is a convenient way to visualize the mass enhancement and the subsequent band narrowing as a function of temperature. However, being an *ab initio* calculation, it depends on the parameter g^2 which is not always easily relatable to the measured properties of materials.

Polarons coupled to long-range distortions are described by the Fröhlich model [84]. Here, the strength of the electron-phonon coupling is described by the parameter

$$\alpha = \frac{e^2}{4\pi\epsilon_0\kappa\hbar} \sqrt{\frac{m}{2\hbar\omega_0}} \quad (1.23)$$

where m is the bare mass and

$$\frac{1}{\kappa} = \frac{1}{\epsilon_{HF}} - \frac{1}{\epsilon_S} \quad (1.24)$$

with ϵ_{HF} the high frequency relative dielectric constant and ϵ_S the static relative dielectric constant. In the intermediate-coupling regime ($1 < \alpha < 5$), perturbation theory shows that the mass enhancement is [85]

$$\frac{m^*}{m} = \frac{1}{1 - \alpha/6}, \quad (1.25)$$

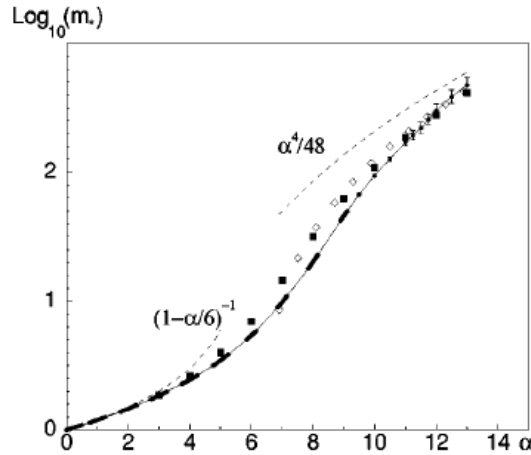


Figure 1.17: Effective mass of a Frölich polaron as a function of its coupling parameter α [86].

while in the high-coupling regime ($\alpha > 10$)

$$\frac{m^*}{m} = \frac{\alpha^4}{48}. \quad (1.26)$$

Quantum Monte Carlo algorithm have been used to estimate the mass enhancement without using any approximations, and have found that the previous expressions correctly estimate the polaron effective mass (Fig. 1.17).

When polarons are coupled to short-range distortion their behavior is described by the Holstein model [87]. Here the coupling is quantified by

$$\lambda = \frac{E_P}{D} \quad (1.27)$$

where D is the half-bandwidth and $E_P \approx \frac{q_D e^2}{\pi \kappa}$ is the polaron level shift, with q_D the Debye momentum. The effective mass is [85]

$$\frac{m^*}{m} = (1 + \lambda). \quad (1.28)$$

However when electrons are coupled to short-range phonon modes, they become sensitive to the dimensionality, coordination number and crystal structure. Thus short-range polarons can have larger effects [88] although a complete theory has not been formulated.

Mass enhancement in manganites can also be caused by correlations. In doped Mott insulators, as the transition to the insulating state is approached from the metallic side, the effective mass diverges [89]. This can be understood from a purely thermodynamic perspective. In a doped Mott insulator, as the system approaches the metal-insulator transition, Coulomb repulsion localizes the carriers, turning them into

localized spin moments. A system of n perfectly localized spin- $\frac{1}{2}$ moments carries a residual entropy

$$S = n \ln 2. \quad (1.29)$$

Thus, the system approaches a state with a non-zero residual entropy, i.e. entropy that persists up to very low temperatures.

This residual entropy can be interpreted through Fermi liquid theory, although the consequences are more general [90]. In a Fermi liquid, the entropy at the coherence temperature $T^* \propto m_{eff}^{-1}$ is a constant:

$$S(T^*) = S_c > 0. \quad (1.30)$$

When the effective mass diverges ($m_{eff} \rightarrow +\infty$), the coherence temperature tends to zero ($T^* \rightarrow 0$), and consequently the system draws near a state with a non-zero residual entropy

$$S_0 = S(T^* \rightarrow 0) = S_c > 0, \quad (1.31)$$

Thus, Fermi liquid theory states that a system tends to a state with a non-zero residual entropy when the effective mass of its carriers diverges. Hence, in doped Mott insulators, the mass divergence close to the metal-insulator transition is a sign of the approach towards a state with a non-zero residual entropy produced by correlations.

When the insulating state is at zero doping ($n = 0$), the mass enhancement of this mechanism is

$$\frac{m^*}{m} = \frac{1}{n^\alpha} \quad (1.32)$$

where typically $\alpha = 1$ [89, 90]. In thin film, values of $\alpha = 2$ can be reached, as many-body effect, enhanced by low dimensionality, contribute to this effect [93].

The increase of effective mass close to a Mott transition is seen in perovskite oxides. For examples, in Sr-doped LaTiO₃ the effective mass reaches $m^* \approx 20m_0$ as the system approaches the insulating state of LaTiO₃ [91]. Ce-doped SrMnO₃ also features strong mass enhancement, with the effective mass reaching $m^* \approx 10m_0$ at the Mott-insulating state of SrMnO₃ [92]. However, this is not a gradual mass enhancement such as that of Sr-doped LaTiO₃, but rather a sharp increase concomitant with a structural transition to a tetragonal lattice due to doping, which forces the polarons to self-organize and change the strength of the electron-phonon interaction. These results show how both mass enhancement mechanisms are present in manganites, and that one has to be careful when attributing such enhancement to a specific mechanism.

1.2.3.3 Electronic structure in reciprocal space

Owing to the strong interaction of electrons with the crystalline structure and neighboring electrons, manganites feature rich electronic structures in reciprocal space.

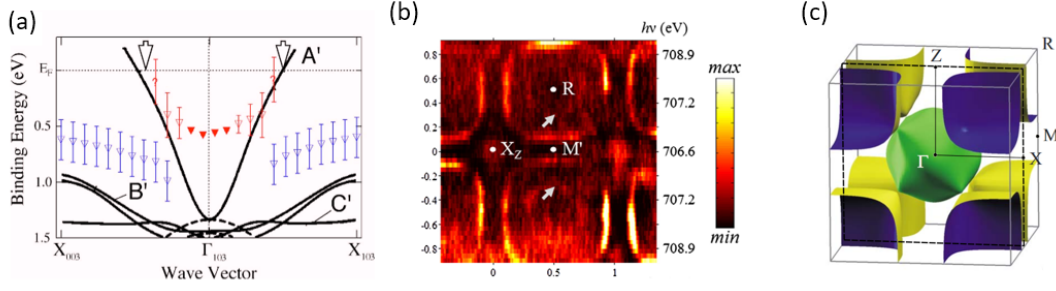


Figure 1.18: (a) ARPES and DFT band structure of $\text{La}_{0.6}\text{Sr}_{0.4}\text{MnO}_3$ [94]. (b) ARPES cut of the Fermi surface of $\text{La}_{0.67}\text{Sr}_{0.33}\text{MnO}_3$ and DFT calculations [96]. (c) DFT calculations of the Fermi surface of $\text{La}_{0.67}\text{Sr}_{0.33}\text{MnO}_3$ [95].

Experimental imaging of these properties is done through angle-resolved photoemission spectroscopy, which confirmed that the valence band of $\text{La}_{0.6}\text{Sr}_{0.4}\text{MnO}_3$ is formed by O 2p orbitals while the conduction band by Mn 3d orbitals [94]. A dispersive band is observed at Γ (Fig. 1.18), indicative of an electron pocket centered at Γ , whose spectral weight is normalized by strong electron-phonon coupling.

The Fermi surface can be imaged by measuring the photoemission signal while scanning the (k_x, k_z) electron momentum space, revealing that the Fermi surface is composed of an electron pocket at Γ and quasi-2D cylinders in the x , y and z directions, intersecting at Γ .

1.2.4 Topology in manganites

Manganites, and in general oxide materials, have a wide range of degrees of freedom, and easily tunable properties and functionalities, making them attractive candidates to explore and harness topological states. Here we will briefly introduce recent developments in skyrmion states and topological Hall effect in manganites.

1.2.4.1 Skyrmions in manganites

In 2012 Nagai and colleagues reported the presence of magnetic bubbles with diameters of 100 – 200 nm in the ferromagnetic and insulating bulk $\text{La}_{0.875}\text{Sr}_{0.125}\text{MnO}_3$. Lorentz microscopy showed that these elliptical bubbles (Fig. 1.19a) are topologically non-trivial, although most of the study focused not on the topology but rather on the size and shape, attributed to strong orbital ordering which increases the anisotropy. Later studies showed that the metallic bulk $\text{La}_{0.825}\text{Sr}_{0.175}\text{MnO}_3$ nucleates both topological and non-topological bubbles of the same size (Fig. 1.19b) [103]. As one would expect in a non-centrosymmetric material, topological bubbles with opposite helicities are nucleated with the same frequency, proving that this type of topological bubble is stabilized by long-range dipole interaction rather than DMI, which nucleates bubbles

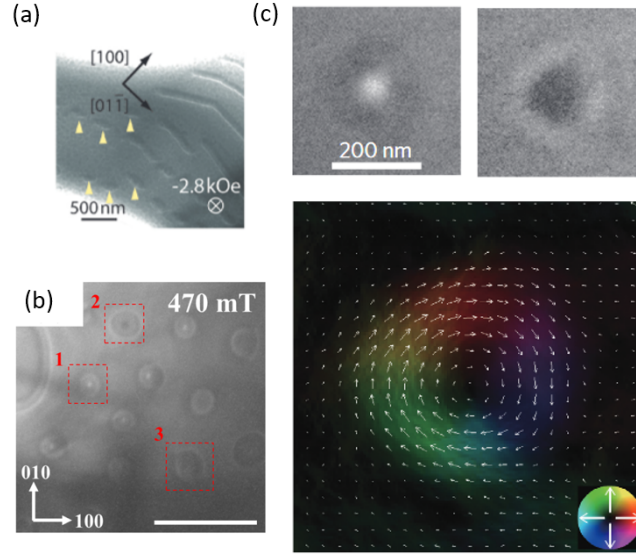


Figure 1.19: (a) Lorentz image at 100 K of $\text{La}_{0.875}\text{Sr}_{0.125}\text{MnO}_3$ showing hellicptical bubble domains [101]. (b) Lorentz image at 100 K of $\text{La}_{0.875}\text{Sr}_{0.125}\text{MnO}_3$ showing skyrmion bubbles with opposite helicity (1 and 2, bright and dark colors) and a topologically trivial bubbles (3) [103]. (c) Overfocused (upper left) and underfocused (upper right) images of a skyrmion bubble in $\text{La}_{0.5}\text{Ba}_{0.5}\text{MnO}_3$, and the color map of its magnetic distribution [102].

with a preferred helicity (see Fig. 1.3a,b for comparison). Thus, these topological bubbles can be called skyrmion bubbles.

The latter manganite is also able to stabilize skyrmion bubbles at zero field. By field cooling the bulk material below the transition from rhombohedral to orthorhombic crystal structure, the zero-field uniform magnetization transitions to a skyrmion bubbles lattice, due to the change in anisotropy [104]. Due to the lack of DMI, which favors certain helicities, and applied magnetic field, which induces Bloch line motion, the bubbles can have very different topologies. Fig. 1.20 shows such bubbles: aside from a standard $Q = 1$ spiral skyrmion bubble we can see a spiral skyrmion bubble encasing another one with opposite helicity, two identical skyrmion bubbles superimposed, and skyrmion bubbles sharing a domain wall with a non-topological bubble.

Skyrmion bubbles have also been reported in bulk $\text{La}_{0.5}\text{Ba}_{0.5}\text{MnO}_3$, very similar to the latter manganite (Fig. 1.19c) [101]. Here, however, the skyrmion states are present only at temperatures higher than the magnetic transition temperature T_C , indicating a strong presence of thermal fluctuations, while in the previous reports on $\text{La}_{1-x}\text{Sr}_x\text{MnO}_3$ the skyrmion bubbles were stable under the respective transition temperatures. Recently, skyrmion bubbles have been detected also in manganite thin films [107]. We will now describe these results, together with reports of topological Hall effect in manganite thin films.

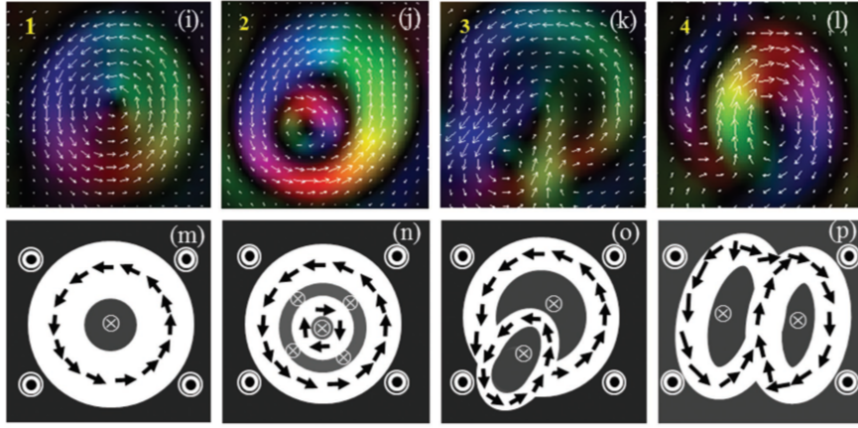


Figure 1.20: Magnetization of skyrmion bubbles in $\text{La}_{0.825}\text{Sr}_{0.175}\text{MnO}_3$ and schematic of their topology [104].

1.2.4.2 Topological Hall effect in manganites

Prior to 2018, there were no reports on the direct imaging of the topology of skyrmion bubbles in oxide thin films. This is due to technical difficulties with the signal-to-noise ratio in Lorentz microscopy when dealing with the weak out-of-plane magnetization of the skyrmion structures, in particular at low temperatures. Due to this, the first reports of a topological-like Hall effect in oxides thin films [105, 106] could not point out directly at topological bubbles as the source of the discovered Hall effect.

In 2018 skyrmion bubbles and topological Hall effect were reported in $\text{La}_{0.7}\text{Sr}_{0.3}\text{Mn}_{1-y}\text{Ru}_y\text{O}_3$ on $(\text{LaAlO}_3)_{0.3}(\text{SrAl}_{0.5}\text{Ta}_{0.5}\text{O}_3)_{0.7}$ (LSAT) substrates [107]. The substitution of Mn with Ru enables the control of the perpendicular magnetic anisotropy. At $y = 0$ the films were magnetized in plane, and at $y = 0.1$ the films were uniformly magnetized out of plane, showing that the Ru substitution increases the strength of the out-of-plane anisotropy. At $y = 0.05$, the films develop a third Hall component, aside normal and anomalous Hall effect (Fig. 1.21a), which can be extracted by subtracting the normal Hall effect (a slope), the anomalous Hall effect (proportional to the magnetization), as shown in Fig. 1.21b. This additional Hall component features the typical anti-symmetric peaks of a topological Hall effect. Magnetic force microscopy shows that the magnitude of the topological Hall effect is highest when the magnetization of the thin film comprises bubble domains (Fig. 1.21c). Lorentz microscopy also shows that these have topological charge $Q = 1 - 2$. Remarkably, the observed topological Hall effect is two orders of magnitude larger than what is expected from the measured density of skyrmion bubbles.

Other thin film heterostructures where topological Hall effect has been observed are $\text{La}_{0.7}\text{Sr}_{0.3}\text{MnO}_3/\text{SrTiO}_3/\text{SrRuO}_3$ and $\text{La}_{0.7}\text{Sr}_{0.3}\text{MnO}_3/\text{BaTiO}_3/\text{SrRuO}_3$ multilayer-

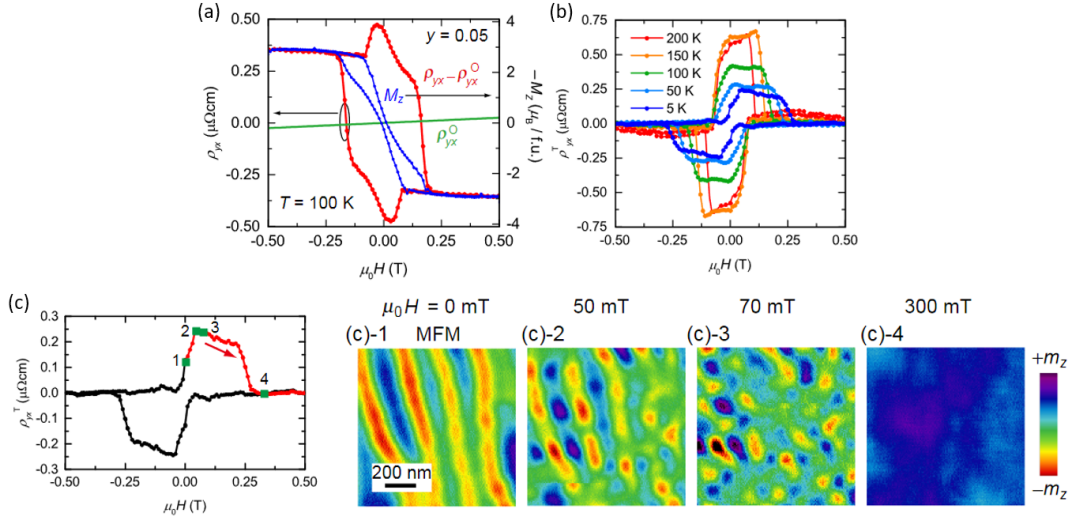


Figure 1.21: (a) Hall effect of $\text{La}_{0.7}\text{Sr}_{0.3}\text{Mn}_{0.95}\text{Ru}_{0.05}\text{O}_3$, together with its normal Hall effect and anomalous Hall effect (proportional to the magnetization). (b) Topological Hall effect, at various temperatures, obtained by subtracting ordinary and anomalous Hall effect from the total effect. (c) Magnetic force microscopy images at different fields, and the topological Hall effect with dots indicating the corresponding fields. [107]

ers [108]. The origin of the topological Hall effect could be topological textures, but it has been posited that Weyl nodes, which give rise to an intrinsic anomalous Hall effect in SrRuO_3 , could also be responsible for the effect. One example of an alternative model was formulated by Kan and colleagues [109], who showed that due to inhomogeneities in thin films of SrRuO_3 can also give rise to a contribution to the anomalous Hall effect indistinguishable in shape from a skyrmion-driven topological Hall effect. Although in this model the effect is visible in a range of temperatures much smaller than the original paper it tries to refute [111] and this large inhomogeneity has not yet been observed in SrRuO_3 , this paper shows how alternative models can explain the topological Hall effect.

1.2.4.3 Anomalous Hall effect in manganites

The anomalous Hall effect in manganites has a strong dependence with temperature. Fig. 1.22a shows the temperature dependence of the anomalous Hall effect of $\text{La}_{0.67}\text{Ca}_{0.33}\text{MnO}_3$: at low temperature up to $T_C/2$ the effect is negligible, at $T_C/2$ the signal starts to rise until it peaks at T_C where it then tails off. There are two models which describe this behavior, and both are intrinsically topological.

Non-collinear spin triads can be viewed as a skyrmion string, which begin as a skyrmion ($Q = +1$) and end as an anti-skyrmion ($Q = -1$). Without any spin-orbit interaction, this does not give rise to any Hall effect as the topological charge of the

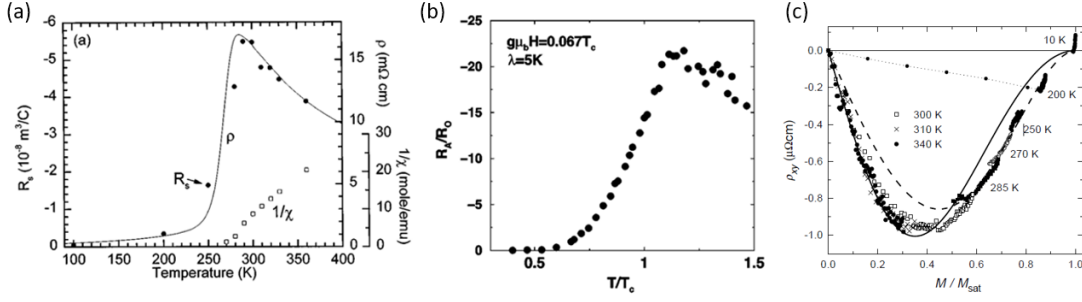


Figure 1.22: (a) Temperature dependence of the anomalous Hall effect of $\text{La}_{0.67}\text{Ca}_{0.33}\text{MnO}_3$ [97]. (b) [99]. (c) [100].

skyrmion string is zero due to the skyrmion and the anti-skyrmion canceling each other out. When spin-orbit coupling and a non-zero magnetization is present, the skyrmions have a privileged orientation. The density of skyrmions and anti-skyrmions becomes [98]

$$n_{\pm} = \alpha e^{-\beta(E_C \pm \lambda S Q a)} \quad (1.33)$$

where $\alpha \approx 230$, E_C is the formation energy of the skyrmion string, λ is the spin-orbit coupling constant, S is the net localized spin and a is the lattice constant. Thus, skyrmions and anti-skyrmions are present in different quantities and non-zero topological charge emerges. The obtained emerging field is, assuming that the difference in Boltzmann energy between the skyrmions and anti-skyrmions is small [99]

$$\langle b \rangle = \frac{\alpha}{6} a \lambda n S \frac{e^{-E_C/k_B T}}{T}. \quad (1.34)$$

This emergent magnetic field can be plugged in the Bruno model (Eq. 1.5) to obtain the magnitude of the anomalous Hall effect. Monte Carlo simulations that well reproduce the trend with temperature of the anomalous Hall effect in manganites are shown in Fig. 1.22b.

At the same time, another model model using the hopping behavior of carriers in manganites was formulated [100]. In a hopping regime, the wave function of an electron is influenced by all of the possible paths it can take from the start to the end of its path. Interference effects, such as localization, can thus arise. Another effect is that every time that an electron passes by a non-collinear spin triad, it picks of a berry phase $\Phi = \Omega/2$, where Ω is the solid angle of the geodesic triangle defined by the spin vectors of the non-collinear spin triad. However, since the electron can hop both clockwise and counter-clockwise, the two contributions cancel out. If spin-orbit coupling is introduced, one sense of circulation becomes favored and a non-zero Berry

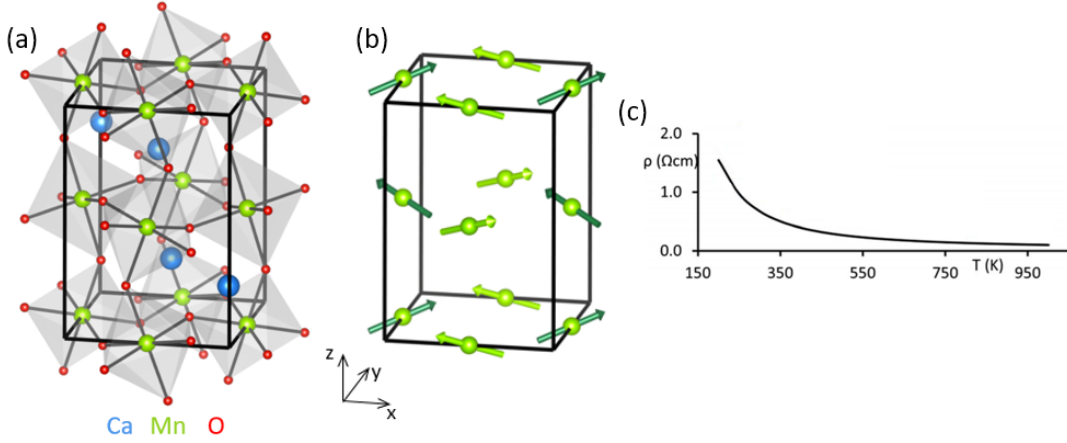


Figure 1.23: (a) Orthorhombic perovskite structure of CaMnO₃. (b) $\mathbf{G}_x\mathbf{A}_y\mathbf{F}_z$ magnetic structure of Mn spins of CaMnO₃ in an orthorhombic lattice. The canting angles are exaggerated ten times. (c) Temperature dependence of the resistivity of bulk CaMnO₃ [115]. Images (1) and (2) courtesy of Julien Varignon.

phase can arise. Here the anomalous Hall effect is

$$\rho_{AHE} = \rho_0 m \frac{(1 - m^2)^2}{(1 + m^2)^2} \quad (1.35)$$

where $m = M/M_{sat}$ and $\rho_0 \propto \lambda$.

1.2.5 CaMnO₃

1.2.5.1 Bulk properties

CaMnO₃ is a manganite which, in its bulk form, crystallizes into an antiferromagnetic and insulating perovskite. Its Mn ions are entirely 4+ while its Ca ions are 2+ [118]. It is an insulator throughout a wide range of temperatures (see Fig. 1.23c), as one would expect from a single-valence manganite. X-ray photoemission experiments show that the bottom the conduction band is formed by Mn 3d states, while the top of the valence band by O 2p states [112]. CaMnO₃ is thus a charge-transfer insulator.

Neutron diffraction experiments show that CaMnO₃ relaxes into an orthorhombically distorted perovskite structure (shown in Fig. 1.23a), with symmetry group Pbnm (or Pnma, although throughout this thesis we will use the Pbnm convention), [113], consistently with its tolerance factor $t = 0.74$. Its oxygen octahedra feature a $a^-a^-c^+$ tilt.

CaMnO₃ features a non-collinear $\mathbf{G}_x\mathbf{A}_y\mathbf{F}_z$ magnetic ordering, shown in Fig. 1.23b, with a Néel temperature $T_N = 120$ K. The dominant order is G-type antiferromagnetism, where each spin is antiferromagnetically aligned aligned to all of its first neighbors. This order is stabilized by superexchange [156], as CaMnO₃ is an insulat-

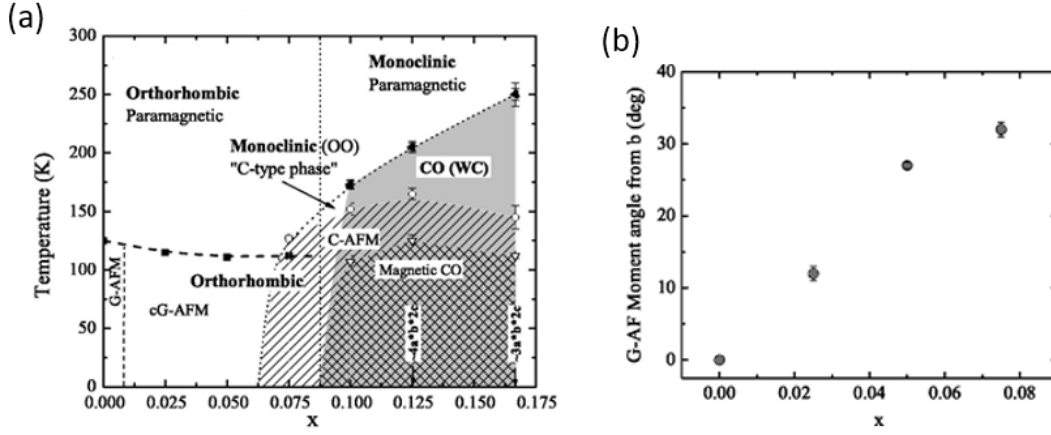


Figure 1.24: (a) Magnetic phase diagram of bulk Ce-doped CaMnO_3 . (b) Ferromagnetic z canting as a function of Ce doping [113].

ing, single-valence manganite. A second magnetic ordering is an A-type ferromagnetic canting in the y direction. This is caused by the oxygen octahedral tilt, which locally breaks inversion symmetry between different Mn ions and causes their spins to cant due to DMI [117]. The antiferromagnetism caused by this tilt is A type, which corresponds to ferromagnetically aligned (010) planes, antiferromagnetically aligned to each other. The last ordering is a small uniform ferromagnetic canting in the z direction. This could be caused by magnetoelectric coupling [114], but also by DMI due to the in-phase c^+ oxygen octahedra rotations along z . The resulting canting angles are small ($\approx 1^\circ$), but give CaMnO_3 a net measurable magnetic moment of about $0.04 \mu_B$.

1.2.5.2 Ce doping

CaMnO_3 can be doped by substituting Ca by Ce ions, obtaining the mixed valence manganite $\text{Ca}_{1-x}\text{Ce}_x\text{MnO}_3$, where x represents the fraction of Ce ions. X-ray absorption spectroscopy shows that each Ce atom, in the 2+ oxidation state, donates two electrons to the system and transforms two Mn^{4+} ions into one Mn^{3+} [118].

As Ce is doped into the material, the increasingly mixed-valence state brings about double exchange which starts to compete with superexchange [120, 119], and increases the net ferromagnetic canting up to 30° for 8% doping (Fig. 1.24b). Together with this weak ferromagnetism, Ce doping stabilizes a metallic, weakly ferromagnetic phase between 6% and 8% doping (Fig. 1.24a) [113]. Although this phase is due to Jahn-Teller-active Mn^{3+} ions, there is no measurable structural change in this region.

At $x = 10\%$ $\text{Ca}_{1-x}\text{Ce}_x\text{MnO}_3$ becomes insulating again, due to charge ordering. In this region the Jahn-Teller effect becomes apparent as it distorts the oxygen octahedra, elongating them along z and shortening them along x and y . Due to this change in

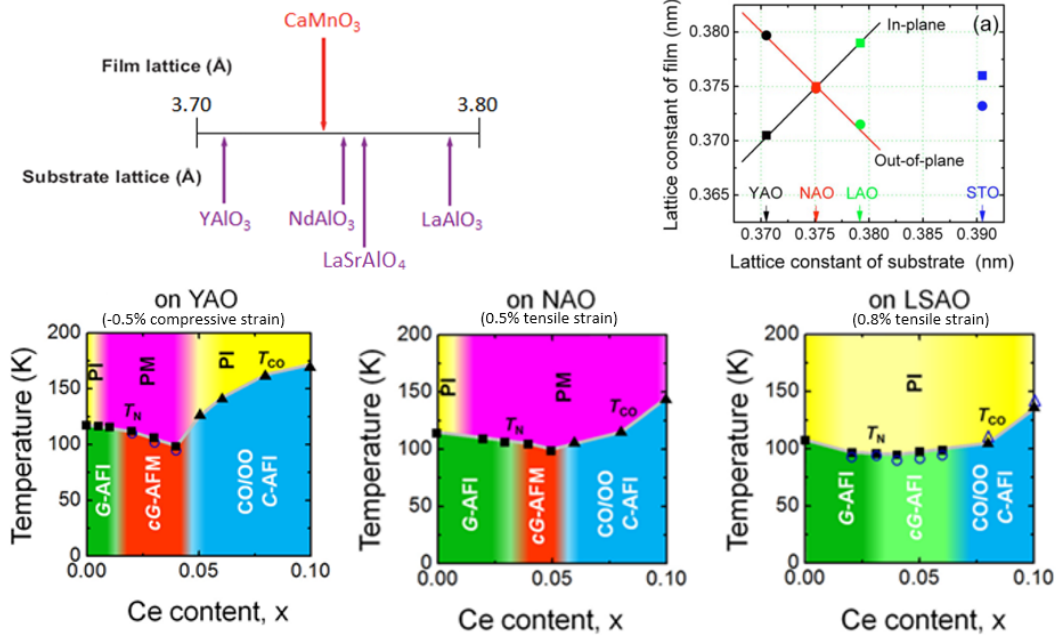


Figure 1.25: (a) Pseudocubic lattice parameter of CaMnO_3 compared to that of YAlO_3 , NdAlO_3 , LaAlO_3 , and SrTiO_3 . (b) In-plane (square) and out-of-plane (circle) lattice constants of 5% Ce-doped CaMnO_3 thin films deposited on YAlO_3 , NdAlO_3 , LaAlO_3 , and SrTiO_3 substrates [124]. (c) Phase diagram of Ce-doped CaMnO_3 thin films [125].

Mn-O-Mn bond length, the manganite transitions from an orthorhombic perovskite to a monoclinic perovskite.

1.2.5.3 CaMnO_3 thin films

Thin films of CaMnO_3 can be grown epitaxially with up to $\pm 1.5\%$ strain. Fig. 1.25b shows that the out-of-plane lattice parameter varies linearly with the mismatch with the substrate lattice, as one would expect in epitaxial growth due to elastic deformation. With larger strains, for example by growing thin films on SrTiO_3 substrates with a 5% tensile strain, the growth ceases to be epitaxial.

When Ce-doped, the phase diagram of these thin film strongly depends on strain. Fig. 1.25c shows the phase diagrams of the thin films of YAlO_3 , NdAlO_3 , LaAlO_3 , and SrTiO_3 substrates. When grown on NdAlO_3 , the phase diagram is the most similar to that of bulk, with a low-temperature metallic phase occurring close to 5% doping. This is consistent with the out-of-plane lattice parameters with 5% doping, in the middle of this phase diagram, showing no elastic deformation of its crystal structure and thus no strain. With an increase of the tensile strain, by growing thin films on LaSrAlO_4 substrates, the metallic phase is not present. This is consistent with Mott transition theory: by increasing the lattice spacing an insulating behavior is favored

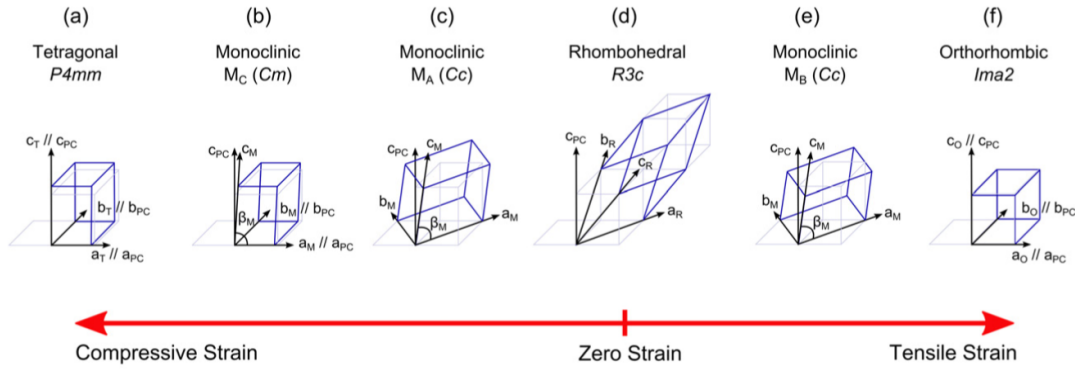


Figure 1.26: Summary of the various crystal structures of thin BiFeO_3 thin films as a function of strain [126].

[48]. Compressive strain, on the other hand, favors this metallic state. When grown on YAlO_3 with a -1% compressive strain, the metallic phase not only occurs in a larger doping range, but the onset is lowered to 2% Ce doping. This shows how strain engineering can increase the strong sensitivity to doping of CaMnO_3 .

1.3 Oxide ferroelectric devices

Ferroelectrics are materials which feature a spontaneous electric net polarization, which can be switched by an external electric field. Their reversible polarization is thus hysteretic, much like the magnetization of ferromagnets (hence the name *ferro*electrics). This occurs in polar materials when the crystal structure becomes non-centrosymmetric, granting a net polarization due to dipoles forming in the single unit cells of the material.

Most ferroelectrics used for both applications and academic research are perovskite oxides, such as BaTiO_3 or $\text{PbZr}_x\text{Ti}_{1-x}\text{O}_3$. Perovskite oxides with purely ionic bonds have inherently centrosymmetric crystal structures where no spontaneous polarization can arise. However, when there is a degree of hybridization between the oxygen orbitals and the orbitals of either A or B cations, anisotropic orbitals are formed which destabilize the cation which is then displaced. Thus, centrosymmetry is broken and a spontaneous polarization arises, in a direction given by the distortions present in the crystal structure.

1.3.1 BiFeO_3

In recent years, BiFeO_3 has garnered a lot of attention due to its highest ferroelectric polarization ever measured, and being the only room-temperature multiferroic (i.e. a material that exhibits more than one ferroic property). In its bulk form, BiFeO_3 crystallizes into a rhombohedrally distorted perovskite structure, with an antiferro-

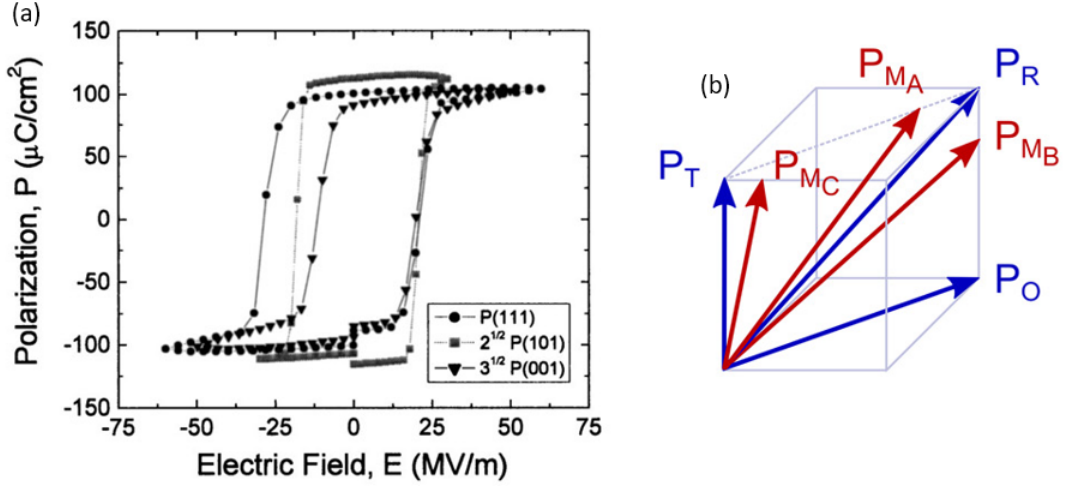


Figure 1.27: (a) Polarization hysteresis loops of BiFeO_3 thin films grown on SrTiO_3 substrates with (111), (101) and (001) orientations, normalized by their projection on the (111) direction (1 , $\sqrt{2}$ and $\sqrt{3}$ respectively) [127]. (b) Polarization direction of BiFeO_3 for different crystal structures [126].

magnetic magnetic structure and a Néel temperature $T_N = 640$ K. Its saturation magnetization is $100 \mu\text{C cm}^{-2}$ and its Curie temperature, i.e. the ferroelectric ordering temperature, is $T_C = 1100$ K.

As with all perovskite oxides, thin films can be grown epitaxially on single-crystal substrates, controlling its structure and properties by strain. BiFeO_3 thin films grown with small epitaxial strain (between -2.6% and 1.2%) possess bulk-like structural properties with a small additional monoclinic distortion, and above 2% the structure becomes orthorhombic. Compressive strain between -3% and -4.2% transforms BiFeO_3 into a mix of rhombohedral phase and a tetragonal-like phase called T-phase with a large saturation polarization of up to $150 \mu\text{C cm}^{-2}$. The defining feature of this T-phase is its high $c/a = 1.2 - 1.3$ ratio, indicative of strong tetragonality. However, there is a debate regarding its space symmetry as there is a small monoclinic distortion along [100]. In this mixed phase, a third polymorph is present. The structure of this intermediate phase is monoclinic, either M_A or M_C depending on the temperature. For compressive strains larger than -4.2% , BiFeO_3 may be stabilized in a pure T-phase. The strain dependence of the crystal structure of BiFeO_3 is schematized in Fig. 1.26.

In BiFeO_3 , ferroelectricity arises from Bi lone pairs. Fig. 1.27a shows the polarization of a BiFeO_3 thin films on SrTiO_3 substrates with bulk-like rhombohedral structure, demonstrating that its polarization lies in the [111] direction. When BiFeO_3 assumes other crystal structures, the ferroelectric polarization re-orient itself in the $(\bar{1}10)$ pseudocubic plane, as shown in Fig. 1.27b. M_A monoclinic is oriented slightly towards [001] while M_B monoclinic is slightly towards [110]. M_C monoclinic is tilted

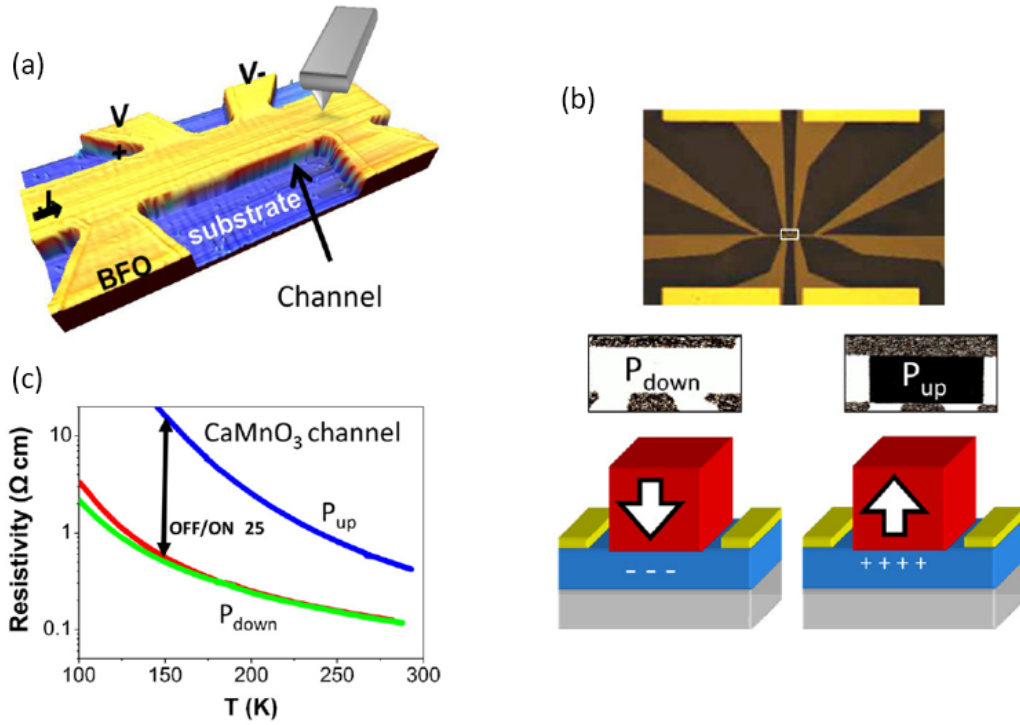


Figure 1.28: (a) Topography of a ferroelectric field-effect device [129]. (b) Schematic of the operation of such device: optical microscopy images of an ideal device with polarization images before and after the polarization switch and sketches of the device in the two polarization states [130]. (c) Temperature dependence of the resistivity of a BiFeO₃/CaMnO₃ device, modulated by ferroelectric field effect [130].

slightly away from [001], towards [111]. T-phase BiFeO₃ is polarized in the [001] direction while the orthorhombic phase is towards [110]. By comparing the polarization vectors in Fig. 1.27b with the strain phase diagram in Fig. 1.26 that increasing compressive strain ($R \rightarrow M_A \rightarrow M_C \rightarrow T$) brings the polarization vector from the unstrained [111] direction towards [001], and increasing tensile strain ($R \rightarrow M_B \rightarrow O$) towards [110].

1.3.2 Ferroelectric control of Mott insulators

Ferroelectric materials can be used in ferroelectric field-effect transistors, bilayer devices where, by switching the polarization of the ferroelectric layer, the properties of the underlying electrode are modified. The nominal accumulation or depletion of the surface carrier density at the ferroelectric/electrode interface is given by the magnitude of the polarization of the ferroelectric. Hence, to achieve a substantial modulation, one has to use a ferroelectric material with large polarization, and an electrode material strongly sensitive to changes in carrier density. A family of such kind of materials are oxide Mott insulators where doping influences functional properties and can be controlled by the ferroelectric field effect [128].

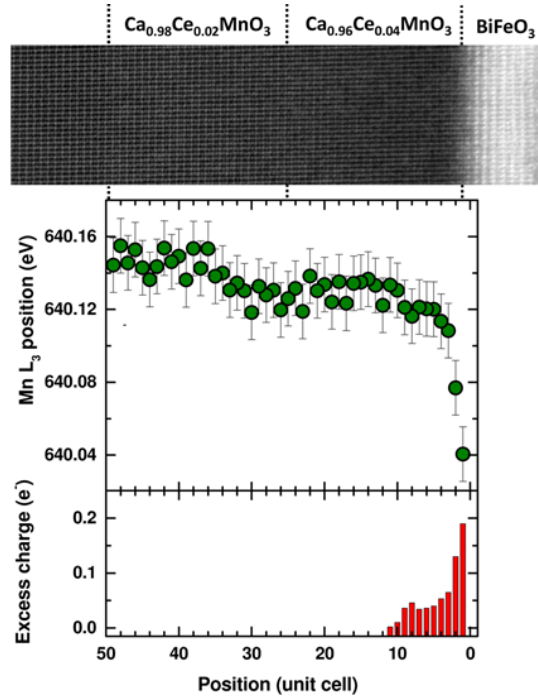


Figure 1.29: Transmission electron microscopy image of $\text{BiFeO}_3/\text{Ca}_{0.96}\text{Ce}_{0.04}\text{MnO}_3/\text{Ca}_{0.98}\text{Ce}_{0.02}\text{MnO}_3$ heterostructures with the Mn- L_3 peak position and the derived excess charge [131].

BiFeO_3 is an ideal candidate as ferroelectric gate material due to its large polarization and ability to accommodate a broad range of lattice mismatches. CaMnO_3 is a Mott insulator where a metallic state is reached at low doping. By growing $\text{BiFeO}_3/\text{CaMnO}_3$ bilayers epitaxially on YAlO_3 (001) substrates, both materials are compressively strained, increasing the sensitivity to doping of CaMnO_3 and increasing the ferroelectric polarization of BiFeO_3 , while re-orienting it in the (001) direction, perpendicular to the interface. Thus, these bilayers are ideal candidates for ferroelectric field-effect transistors where properties of a Mott insulators are controlled by ferroelectricity.

In 2013, Yamada et al. reported a strong modulation of the resistivity of CaMnO_3 by switching the polarization of the overlying BiFeO_3 layer [130]. Micrometer-sized devices were patterned by optical lithography (Fig. 1.28a) and the polarization of BiFeO_3 switched locally by piezoresponse force microscopy (Fig. 1.28b), inducing a change in the carrier density of CaMnO_3 . The ON/OFF resistivity ratio reaches 25 at low temperatures. The variation of the sheet carrier density is in the order of magnitude of previously reported values in similar heterostructures [132, 133] ($\Delta n_S = 0.4 \times 10^{14} \text{ cm}^{-2}$), though it corresponds to a polarization one order of magnitude smaller than the nominal value expected from the polarization of BiFeO_3 .

Scanning transmission microscopy experiments were carried out in similar bilayers

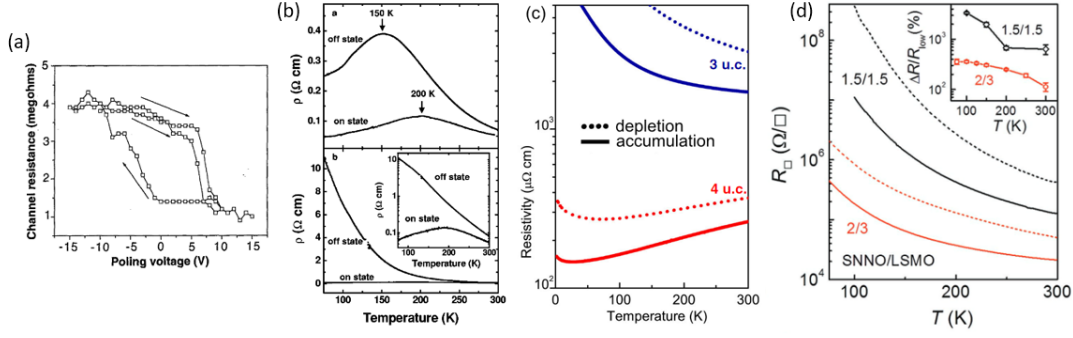


Figure 1.30: (a) Resistance hysteresis loop of $\text{PbZr}_{0.2}\text{Ti}_{0.8}\text{O}_3/\text{La}_{0.7}\text{Ca}_{0.3}\text{MnO}_3$ bilayers [135]. Temperature dependence of the resistivity, before and after ferroelectric switching, of (b) $\text{PbZr}_{0.2}\text{Ti}_{0.8}\text{O}_3/\text{La}_{0.7}\text{Sr}_{0.3}\text{MnO}_3$ (top: 4 nm-thick manganite, bottom: 3.8 nm-thick manganite) [136], (c) $\text{PbZr}_{0.2}\text{Ti}_{0.8}\text{O}_3/\text{LaNiO}_3$ bilayers [134], and (d) $\text{PbZr}_{0.2}\text{Ti}_{0.8}\text{O}_3/\text{Sm}_{0.5}\text{Nd}_{0.5}\text{NiO}_3/\text{La}_{0.67}\text{Sr}_{0.33}\text{MnO}_3$ heterostructures [138].

[131]. Here the atomically-resolved and element-specific electronic properties of the film was measured by electron energy loss spectroscopy and the charge accumulation was estimated from the position of the Mn-L₃ position. Fig. 1.29 shows the depth-profiling of this excess charge, where we can see that the BiFeO₃ layer, polarized towards the CaMnO₃, induces an excess charge of 0.65 e^- in the first 10 unit cells of the doped CaMnO₃ at the interface. This value is smaller than the nominal value given by the polarization of BiFeO₃ of 0.9 e^- per surface u.c., but it is also larger than the effective charge accumulation extracted from transport. This suggests that either a fraction of this interface accumulated charges are not mobile, or that ferroelectric switching is not complete.

Other reports ferroelectric control of a Mott insulator used $\text{PbZr}_{0.2}\text{Ti}_{0.8}\text{O}_3$ as the ferroelectric material. The first report is from Matthews and colleagues in 1997 [135], who showed that $\text{PbZr}_{0.2}\text{Ti}_{0.8}\text{O}_3/\text{La}_{0.7}\text{Ca}_{0.3}\text{MnO}_3$ bilayers exhibited a three-fold change of resistance by switching the polarization of $\text{PbZr}_{0.2}\text{Ti}_{0.8}\text{O}_3$. Fig. 1.30a shows the channel resistance hysteresis loop, which follows the polarization loop of $\text{PbZr}_{0.2}\text{Ti}_{0.8}\text{O}_3$. In 2005, Hong et al. reported a metal-insulator transition in similar bilayers [136]. The temperature dependence of the resistivities of such devices are shown in Fig. 1.30b. More recently, in 2014 Marshall and colleagues reported similar results in $\text{PbZr}_{0.2}\text{Ti}_{0.8}\text{O}_3/\text{LaNiO}_3$ bilayers, although a full metal-insulator transition of LaNiO₃ was not reached [134]. Chen et al. showed how the efficiency of the ferroelectric field-effect in $\text{PbZr}_{0.2}\text{Ti}_{0.8}\text{O}_3/\text{Sm}_{0.5}\text{Nd}_{0.5}\text{NiO}_3$ can be improved up to ON/OFF ratios of 30, by using the exchange coupling between the nickelate layer and a manganite buffer layer [138].

Despite intensive efforts, a complete metal-insulator transition has not been successfully demonstrated in such devices. The variations of sheet carrier resistance

achieved by polarization switching are always smaller than what is expected by the polarization of the ferroelectric gate. Ferroelectric domain dynamics or interface effects, for example, can play a role in limiting the accumulation and depletion of charge carriers. This shows that the ferroelectric field effect in ferroelectric/Mott insulator devices is much more complex than one could think, warranting further studies.

Chapter 2

Manganite thin film growth and properties

2.1 Pulsed laser deposition

All of the thin films presented throughout this thesis were grown by pulsed laser deposition (PLD). In this technique, laser pulses are shot at a target of the desired material, placed inside a vacuum chamber with a controlled background gas content. The laser vaporizes the target material, creating a plasma plume which deposits the material onto a heated substrate positioned in front of the target. This technique is frequently used to grow oxide thin films as it permits stoichiometric growth without the need for ultra-high vacuum.

The PLD setup used a commercially available Nd:YAG pulsed laser (Quantel Q-smart 850) with a fundamental wavelength of 1065 nm. A frequency tripler and a set of dichroic lenses are used to create a 355 nm pulse and to separate it from the fundamental wavelength which is then dumped. The frequency of the 7 ms-long pulses can range from 1 to 10 Hz, and the energy of the pulse is controlled by an external attenuator. The well-tuned pulse is then focalized by a converging lens and shot into the vacuum chamber through a quartz window, hitting the target at a 45° angle. The effective laser spot size is measured by shooting 10 pulses on a fixed target and then its surface is measured through an optical microscope. Throughout the changes in setup of the PLD during the three years of this PhD, the spot size has stayed in the 4.5 – 5.5 mm² range.

We used oxygen as the background gas in the vacuum chamber during growth, as is normally the case for oxides. The oxygen pressure was controlled by controlled by introducing the oxygen through a tunable valve, while simultaneously pumping the chamber with a turbomolecular pump. This enabled us to control the oxygen pressure with a precision of about 10⁻⁴ mbar. The temperature of the substrates is

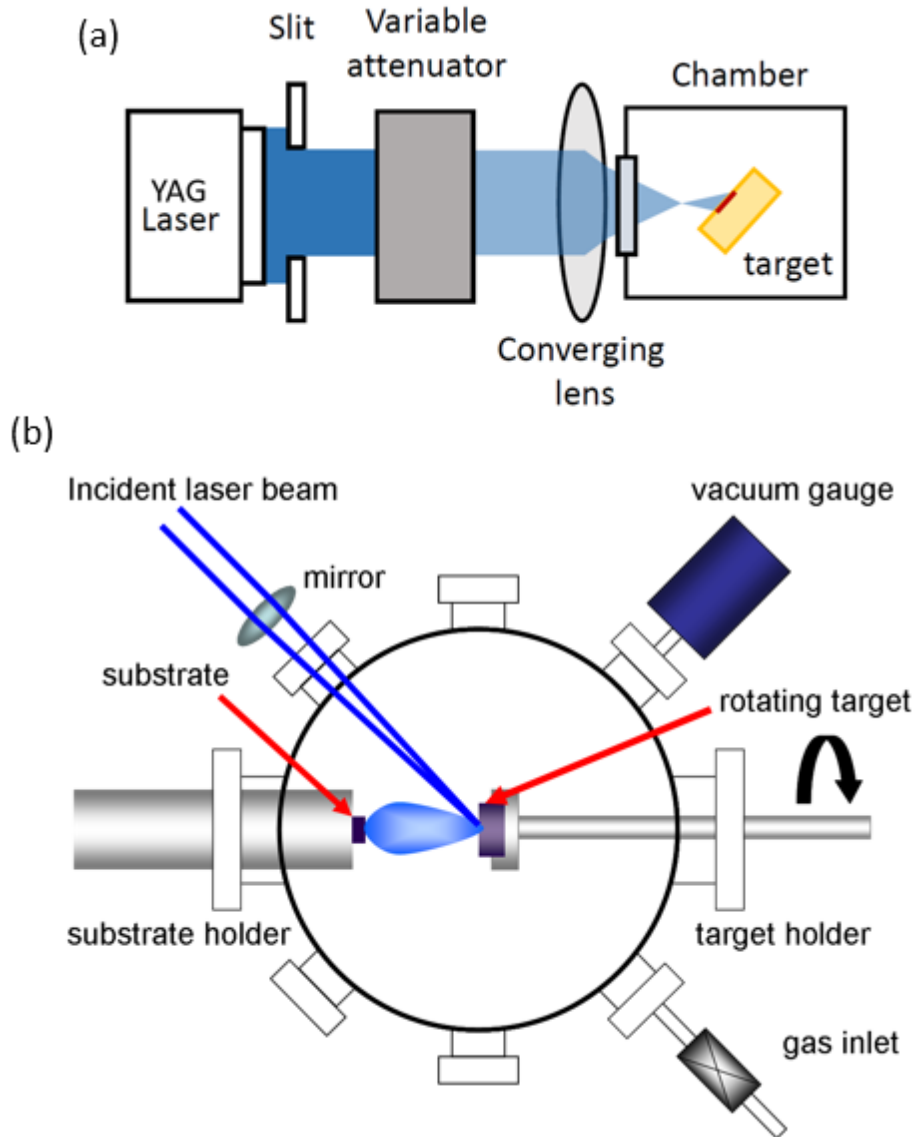


Figure 2.1: Schematic of our operation of a pulsed laser deposition setup. (a) The energy laser pulse is controlled by an external attenuator, and the pulse is focused on the sample with a converging lens. The target is set after the focus of the lens and thus spot size of the laser pulse can be controlled by moving the lens. Adapted from [142]. (b) Inside the vacuum chamber, the oxygen atmosphere is controlled by a small inlet. The focused laser hits the target, creating a plasma plume which hits the substrate, whose temperature is controlled by a heater set on the back of the substrate holder. Adapted from [143].

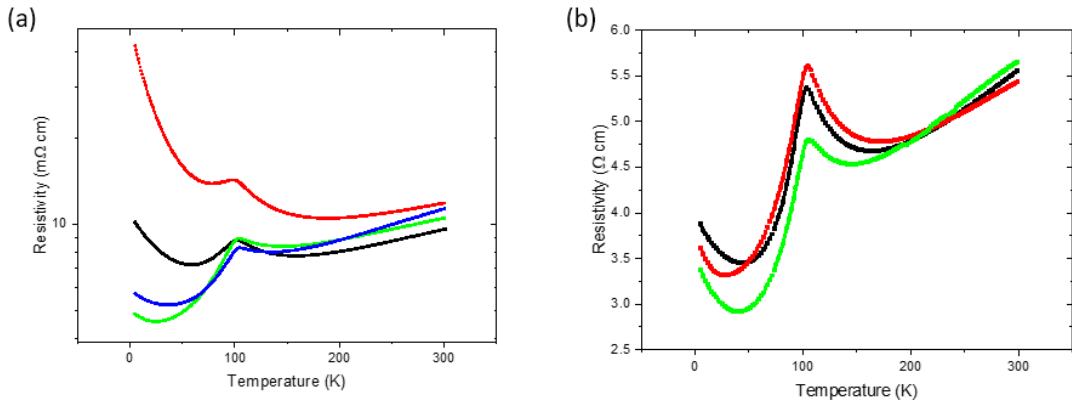


Figure 2.2: Temperature dependence of the resistivity of two sets of three 20 nm thick, 4% doped CaMnO_3 thin films on YAlO_3 before (a) and after (b) optimization.

controlled by a heater located in the back of the substrate heater. To measure the temperature, we used a non-contact pyrometer as the setup did not allow any local temperature measurement. The temperature could not be directly measured on the sample, as the infrared reading depended strongly on the opacity of the samples, and as such changed during the growth itself as the opaque CaMnO_3 is grown on transparent substrates. To counter this issue, we measured the temperature on the substrate holder, next to the substrate itself, where we found the temperature to be about 5°C less than center of the holder.

The bulk of the research shown in this thesis was focused on CaMnO_3 thin films on YAlO_3 substrates. Hence, the first step of our PhD work was to improve the growth conditions for Ce-doped CaMnO_3 thin films used in previous work of our research group [131, 130]. In particular, the main focus was to increase the reproducibility of the electronic properties of the Ce-doped CaMnO_3 thin films. This is an issue in the low-doping regime as a small change in dopant concentration can lead to a large change in carrier density and thus in resistivity, and this is exacerbated by the strong sensitivity of CaMnO_3 to Ce doping. At first there was little control over the metallic quality of the samples. Fig. 2.2 shows the temperature dependence of the resistivity of 20 nm thick samples grown with pulses in the 55 – 70 mJ range. The resistivity varies to a degree that its value at low temperature fluctuates around a whole order of magnitude with no clear trend with pulse energy.

We found that the lack of reproducibility was due to improper substrate preparation. The substrates were annealed in the vacuum chamber, at 700 K and 0.4 mbar of oxygen pressure. With low annealing times (less than 15 minutes) the substrates would retain dirty surfaces, and with higher annealing times the dirt was removed but the then-visible surface terraces featured holes and fragmented steps, which increase the roughness of the substrate and degrade the quality of the samples.

We tried annealing the substrates in a separate furnace where high oxygen pressure

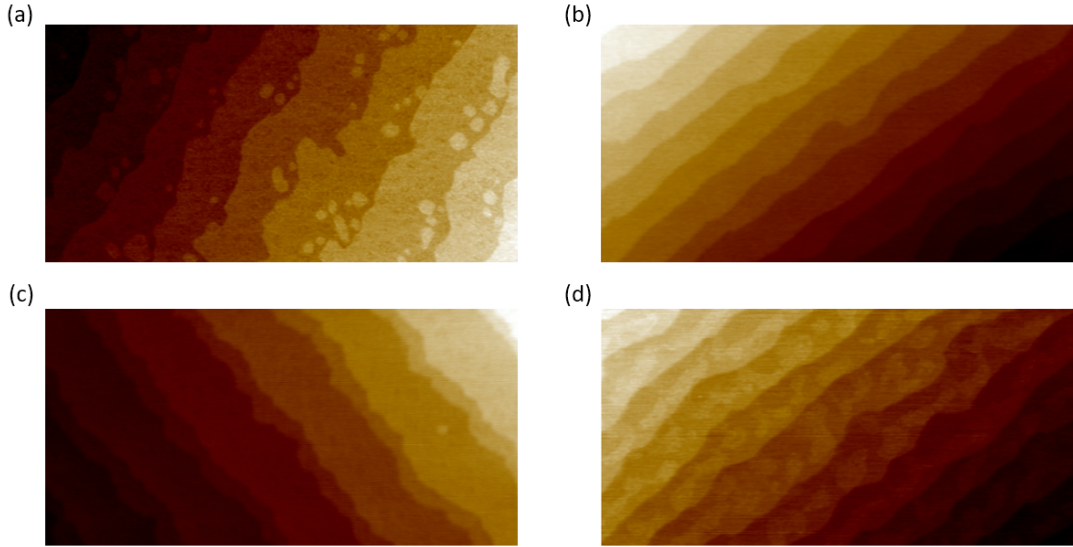


Figure 2.3: Substrates annealed for (a) 2, (b) 2.5 and (c) 3 hours at 1000°C after acetone cleaning and isopropanol ultrasound bath. (d) Shows a substrate treated with a 3-hour annealing at 1000°C after 3 minutes of HF etching.

and higher temperatures were possible. After cleaning the YAlO_3 substrate in acetone and an isopropanol bath in ultrasound, we annealed the substrates in an oxygen-rich environment at 1000°C . Fig. 2.3 shows the surfaces of substrates annealed for different times. Substrates annealed for 2 hours had rough step edges, with many islands and small dents in the terraces. With 3 hours of annealing these features disappeared, but instead the substrates showed step bunching, a signature of over-annealing. Samples annealed for 2.5 hours showed neither signs of under- or over-annealing, with flat, even terraces and well-defined steps (Fig. 2.3b). We also tried different HF etching techniques, but found that they did not improve the surface of the substrates compared to simple annealing: the HF recipes that gave good results for most of the substrates would unpredictably give rise to rough terraces with half unit cell-high bumps (Fig. 2.3d), or with mixed termination (measurable by the phase of tapping AFM).

After optimizing the surface of the YAlO_3 substrates, we tweaked the growth parameter of Ce-doped CaMnO_3 to optimize the surface and metallicity of our samples. The optimal conditions we found are a substrate temperature $T_{sub} = 620^{\circ}\text{C}$, oxygen pressure $P_{O_2} = 0.2$ mbar, with a substrate-target distance of 44 mm. The laser pulses had a frequency $f = 2.5$ Hz and a fluence of 1.45 J/cm². Post-growth annealing was performed by increasing the oxygen pressure to $P_{O_2} = 300$ mbar for 30 minutes, keeping the same heater power. Here the substrate temperature drops to $T_{sub} \approx 580^{\circ}\text{C}$ due to the higher oxygen pressure.

The topography of the Ce-doped CaMnO_3 samples strongly depends on that of the YAlO_3 substrates. Samples grown on substrates with terrace widths smaller than

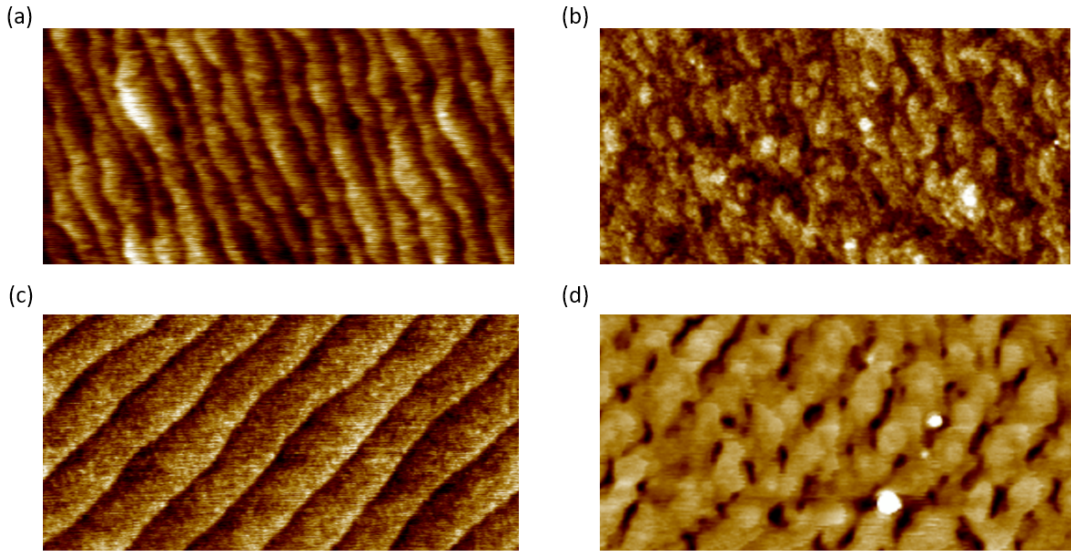


Figure 2.4: Topography of 4% doped, 20 nm thick CaMnO_3 thin films (b,d) on YAlO_3 substrates (a,c).

100 nm (Fig. 2.4a) showed surfaces with visible terraces and small root mean square roughnesses of ≈ 0.2 nm (Fig. 2.4b). Samples grown on substrates with wider terraces (Fig. 2.4c) showed 3 – 5 nm-deep holes in the otherwise flat surfaces. These holes are aligned along the terrace edges (Fig. 2.4d) and indicate a low surface mobility of the ions of the plasma. Nonetheless, with these large terrace widths the transport properties of the Ce-doped CaMnO_3 samples are reproducible and comparable to those of sample grown on smaller terraces. The structural properties of the samples also did not degrade in the presence of the surface holes.

2.2 Structural properties

Both YAlO_3 and CaMnO_3 feature a $Pbnm$ orthorhombic perovskite crystal structure due to a $a^-a^-c^+$ oxygen octahedra tilt. Fig. 2.5 shows a cubic perovskite crystal structure together with an orthorhombically distorted one. When the oxygen octahedral tilt is present, the period increases. The primitive vectors become

$$\vec{a}' = \frac{\vec{a} + \vec{b}}{\sqrt{2}} \quad (2.1)$$

$$\vec{b}' = \frac{\vec{b} - \vec{a}}{\sqrt{2}} \quad (2.2)$$

$$\vec{c}' = 2\vec{c} \quad (2.3)$$

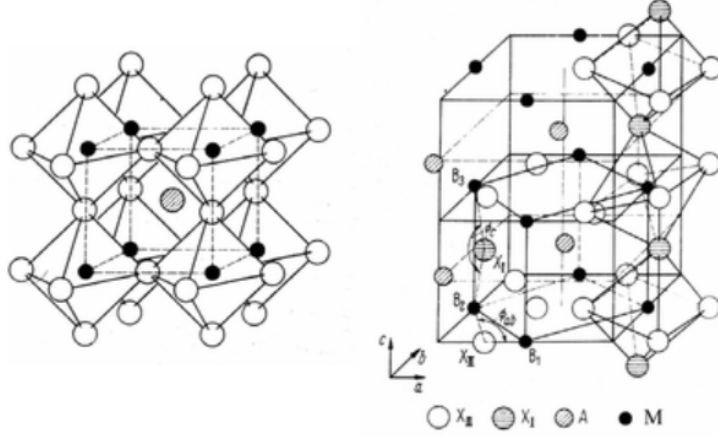


Figure 2.5: Cubic perovskite (left), and orthorhombic perovskite structure (right), with the undistorted cubic cell embedded for reference [141].

where \vec{a} , \vec{b} and \vec{c} are the cubic perovskite primitive vectors, or

$$[100]_o = [110]_c \quad (2.4)$$

$$[010]_o = [\bar{1}10]_c \quad (2.5)$$

$$[001]_o = [002]_c. \quad (2.6)$$

The corresponding planes become

$$(100)_o = \left(\frac{1}{2} \frac{1}{2} 0\right)_c \quad (2.7)$$

$$(010)_o = \left(\frac{\bar{1}}{2} \frac{1}{2} 0\right)_c \quad (2.8)$$

$$(001)_o = \left(00 \frac{1}{2}\right)_c. \quad (2.9)$$

To verify the crystalline quality of the Ce-doped CaMnO_3 samples we performed X-ray diffraction measurements. First, we performed reciprocal space maps around the (004), (208) and (028) planes of the orthorhombic structure. Fig. 2.6 shows these three maps for a 20 nm thick, 4% Ce-doped sample. The sample peaks can be clearly seen widened along Q_z , due to the low sample thickness, while the in-plane Q is well-defined and narrow, indicating a uniform strain state. In all of the maps the in-plane components of the peaks of the sample and its substrate coincide, indicating that the sample is grown epitaxially with no relaxation.

Owing to the good epitaxial growth, we can study the structure of our samples with $2\theta - \omega$ scans. Fig. 2.7a shows such scan for the same 20 nm thick, 4% Ce-doped sample, with Laue fringes attesting to the structural coherence of the sample. The out-of-plane lattice parameter increases with doping (Fig. 2.7b). Ce has a larger ionic

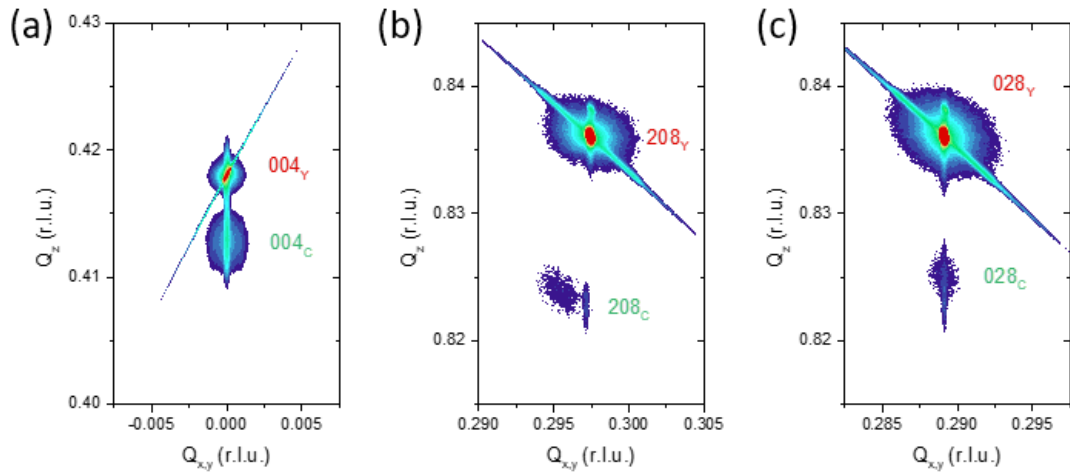


Figure 2.6: Reciprocal space maps showing the (004), (208) and (028) reflections of the YAlO_3 substrate and a 4% doped Ce-doped CaMnO_3 thin film.

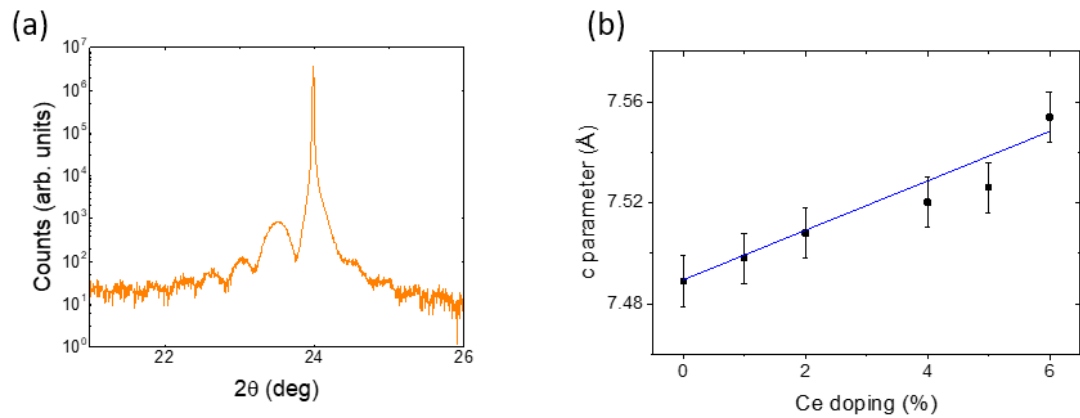


Figure 2.7: (a) X-ray diffraction $2\theta - \omega$ (004) peaks of the YAlO_3 substrate and a 4% doped Ce-doped CaMnO_3 thin film. (b) Measured unit cell c as a function of doping. The blue line is the fit giving a Poisson ratio $\nu = 0.18$, using Vegard's law to compute the doped bulk unit cell.

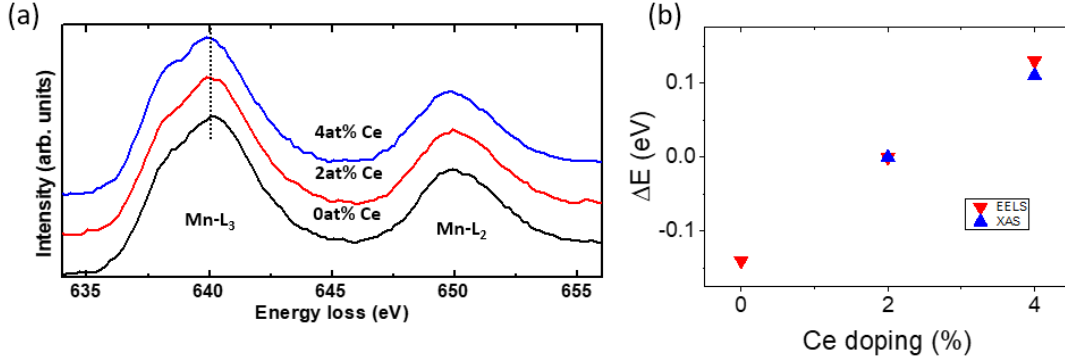


Figure 2.8: (a) Electron energy loss spectroscopy 30 K in total electron yield mode, for 2% and 4% Ce doped CaMnO_3 . (b) Dopning dependence of the energy shift from X-ray absorption spectroscopy and electron energy loss spectroscopy.

radius than Ca (115 and 100 pm respectively), and thus by substituting Ca with Ce increases that size of the unit cell. Quantitatively, Vegard's law states that

$$\vec{V}_{\text{Ca}_{1-x}\text{Ce}_x\text{MnO}_3} = (1-x)\vec{V}_{\text{CaMnO}_3} + x\vec{V}_{\text{Ce}_x\text{MnO}_3} \quad (2.10)$$

where $\vec{V} = \vec{a}, \vec{b}, \vec{c}$ is one of the unit cells of the $Pbnm$ structure. The \vec{c} increases with Ce in bulk, but in thin films compressive strain additionally increases the out-of-plan \vec{c} according to Poisson's law

$$\nu = -\frac{d\epsilon_z}{d\epsilon_{x,y}} \quad (2.11)$$

where ϵ_z is the out-of-plane strain, $\epsilon_{x,y}$ is the in-plane strain and ν is the Poisson's ratio. By combining the last two equations we can fit the doping dependence of \vec{c} , obtaining a Poisson's ratio $\nu = 0.18$, assuming a constant constant ν (Fig. 2.7).

2.3 Electronic properties

We performed X-ray absorption spectroscopy and electron energy loss spectroscopy to understand the electronic and orbital structure of our Ce-doped CaMnO_3 thin films. Fig. 2.8a shows Mn L_2 and L_3 edges at 30 K for 0%, 2% and 4% doping. Upon increasing doping, the Mn L_3 edge shifts to a lower energy, indicating an shift to lower valence states. In Fig. 2.8b this shift is plotted against doping [131]. Its linear trend indicates that Ce doping indeed dopes CaMnO_3 with electrons.

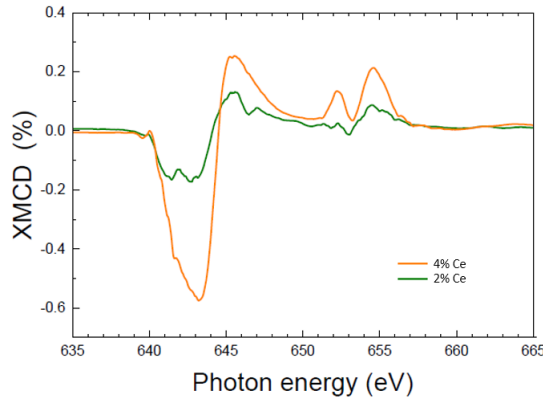


Figure 2.9: X-ray magnetic circular dichroism for 2% and 4% Ce doped samples at 10 K and 2 T.

2.4 Magnetic measurements

Fig. 2.9 shows X-ray magnetic circular dichroism data for 2% and 4% thin films. Consistently with literature (see 1.2.5), the magnetic signal increases with doping. Its amplitude is comparable to data in literature [139] and the general shape of the signal is similar to that for other pseudocubic manganites such as $\text{La}_{2/3}\text{Sr}_{1/3}\text{MnO}_3$ [140] suggesting a comparable electronic and orbital structure with spin-polarized e_g conduction bands.

We measured the magnetization of thin film samples of different dopings in-house with a superconducting quantum interference device, shown in Fig. 2.10a. Undoped CaMnO_3 samples showed a small magnetic moment ($10 \text{ emu}\cdot\text{cm}^{-3}$) at low temperature, confirming the canted antiferromagnetic nature even without doping. By adding Ce doping the magnetization increases, evidencing the weakly-ferromagnetic nature of the films. The doping dependence of the low temperature magnetization is linear (Fig. 2.10b), as one would expect in this low doping regime (cfr. Fig. 1.24b). Throughout all dopings the transition temperature T_C is in the 110 – 115 K range, since the transition is driven by superexchange, which is not influenced by doping.

Magnetization loops can also be measured with this technique, however at field higher than those required to measure the remanent magnetization, the paramagnetic signal from the substrate becomes large and cannot be disentangled from that of the sample (Fig. 2.10c). Additionally, the magnetization of patterned samples is hard to measure due to the small volume of already weakly-ferromagnetic manganite that remains after the patterning process. For this reason, we measured the magnetization loops of our samples with a magneto-optic Kerr effect setup.

The magneto-optic Kerr effect (MOKE) is the change in polarization of incident light as it is reflected by a magnetized surface. As the magnetization of Ce-doped CaMnO_3 thin films is out of plane, we measured the light reflected at a near-normal

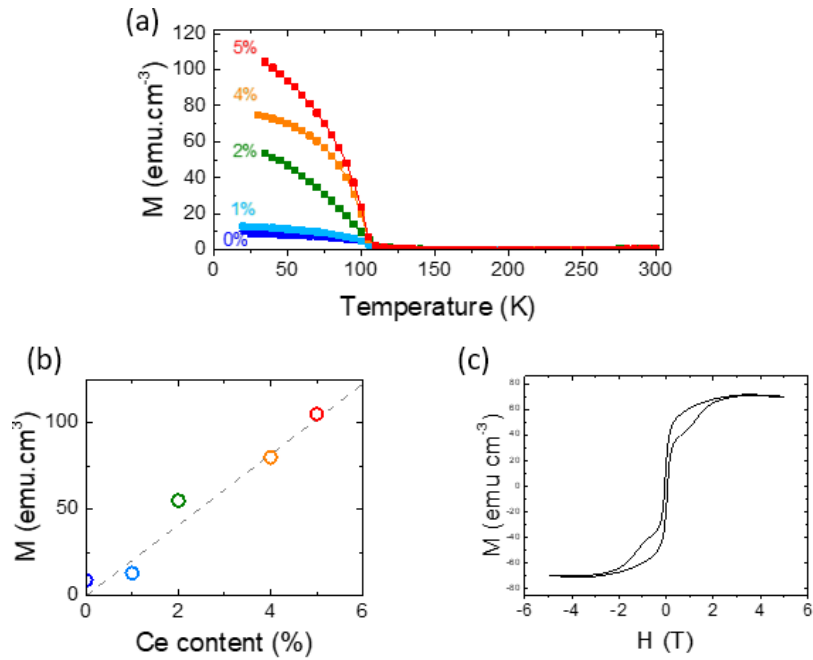


Figure 2.10: (a) Temperature dependence of the magnetization measured with a superconducting quantum interference device in a field of 1 kOe for different doping levels. (b) Doping dependence of the magnetization. (c) Magnetization loop for a 4% Ce doped sample at 30 K

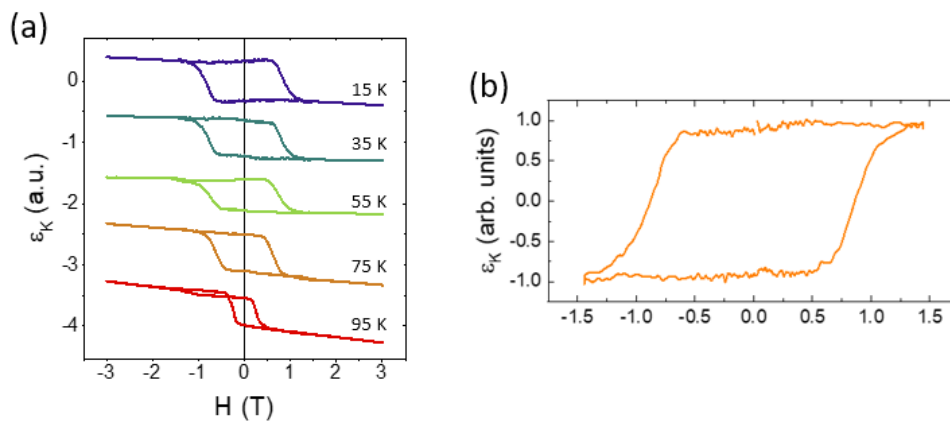


Figure 2.11: Kerr ellipticity of the 20 nm 4% Ce-doped CaMnO_3 thin film sample from Fig. 4.1 at different temperatures, measured at 600 nm.

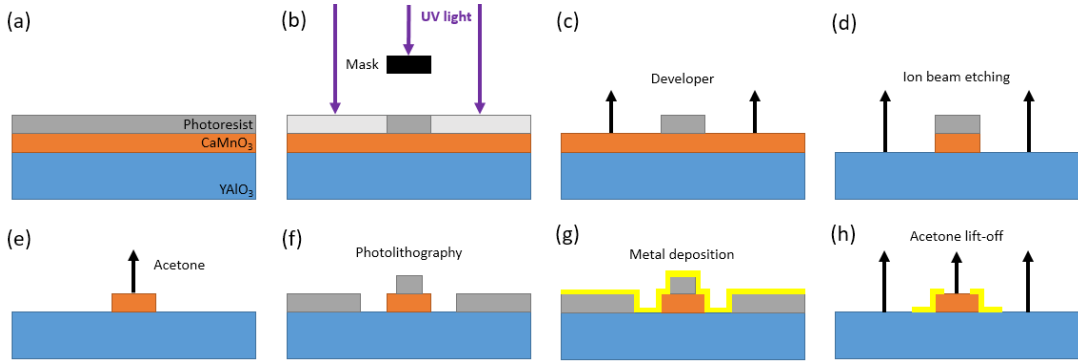


Figure 2.12: Fabrication process of Ce-doped CaMnO_3 Hall bar devices. (a) The manganite thin film is coated with a positive photoresist. (b) The sample is exposed in UV light through a mask with the desired pattern. (c) The irradiated areas of the photoresist are dissolved in a developed solution. (d) Ion-beam etching is used to remove the manganite material in the areas not covered by photoresist. (e) The remaining photoresist is dissolved and the sample cleaned. (f) Processes (a)-(e) are repeated in order to define the metal electrode areas. (g) The sample is covered with a 50 nm-thick layer of Pt by sputtering. (h) The photoresist is lifted off, leaving the Pt only in the electrode areas.

angle. In this geometry, when shining linearly-polarized light, the magnetization creates a difference in amplitude between the electric field components parallel and perpendicular to the plane of incident light. This ratio is the Kerr ellipticity ϵ_K , which is proportional to the magnetization.

The used light source is a 150 W Xe arc lamp, and the produced light was then monochromated, collimated and polarized. The light is then reflected by the sample and collected in an analyzer that can be set to measure s- and p-polarized light. The signal is then collected from the detector and brought to a lock-in amplifier.

The measured Kerr ellipticity of the a 4% Ce-doped 20 nm-thick CaMnO_3 thin film on YAlO_3 is shown in Fig. 2.11. This figure shows a remanence of 100%, confirming that shows the typical behavior of a ferromagnet, with its coercive field decreasing upon heating.

2.5 Device fabrication

We performed transport experiments with Hall bars, fabricated with a combination of optical lithography, ion beam etching and lift-off techniques. Here we will describe the process, divided into the steps shown in Fig. 2.12.

- (a) A sample grown by PLD is soaked in acetone and placed in an ultrasound bath for 1 minute, then rinsed in isopropanol. A photoresist (S1813) is then spin-coated onto the sample at 4000 rpm for 30 seconds. The spun photoresist is baked by placing the sample on a hot plate at 90°C for 1 minute.

- (b) The photoresist is exposed to ultraviolet light through a positive mask, which defines the geometry of the Hall bars.
- (c) The photoresist is developed by shaking the sample by hand for 30 seconds in a developer solution (MF319), which removes the parts of the photoresist not exposed to the UV light. To stop the reaction, the samples is then shaken by hand in de-ionized water for 30 seconds.
- (d) The geometry of the photoresist defines the desired pattern on the sample, which is ion-beam etched, removing all of the parts of the sample not covered by the photoresist. This process is monitored by secondary ion mass spectroscopy (SIMS), which quantifies which elements are milled by the etching, allowing to visualize when the sample has been completely etched and the substrate is starting to be etched as well.
- (e) The remaining photoresist is removed by soaking the sample in a becker of acetone and placed in an ultrasound bath for 1 minute and rinsing in isopropanol. At this point the Hall bars are patterned onto the sample.
- (f) To fabricate metal contacts, steps (a)-(e) are repeated, with a mask defining the electrodes.
- (g) When the process is finished, a 50 μm layer of Pt is deposited onto the sample.
- (h) The sample is soaked in a becker of acetone and placed in an ultrasound bath for 1 minute to lift off the photoresist together with the Pt deposited on top, and then rinsed in isopropanol.

Fig. 2.13 shows a sample patterned with a conventional Hall bar mask, with its well defined edges attesting the good quality of the fabrication process.

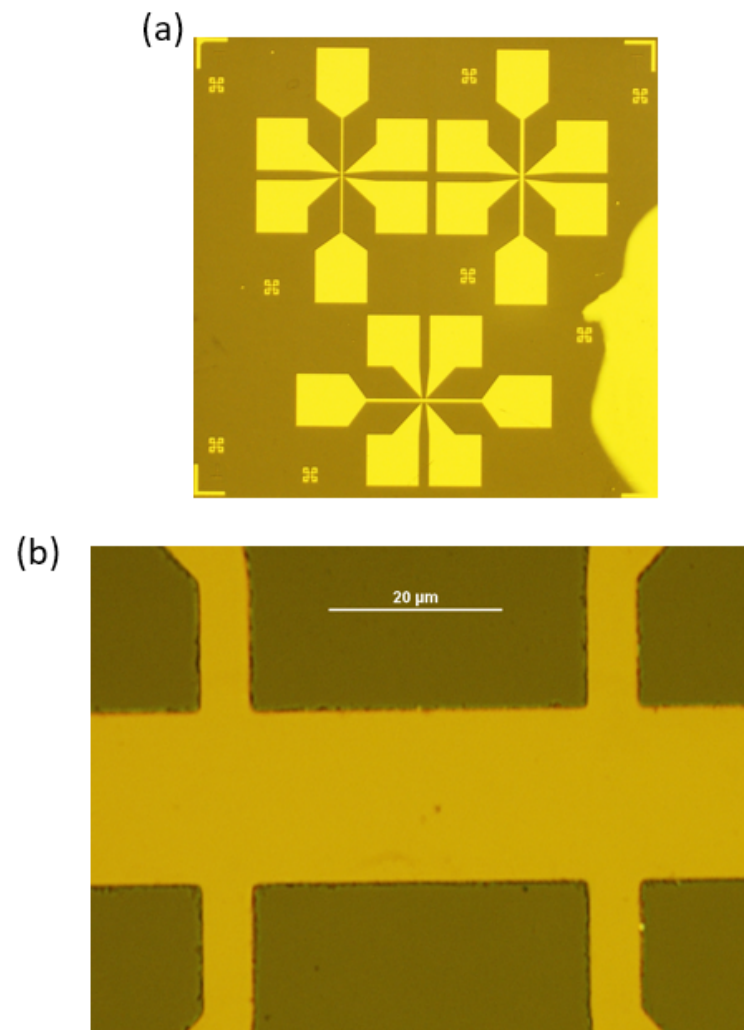


Figure 2.13: Optical microscope images of a patterned device (a) and zoom-in on the Hall bar probes (b).

Chapter 3

Electronic structure of Ce-doped CaMnO_3 thin films: doping a charge-transfer insulator

Bulk CaMnO_3 is an antiferromagnetic charge transfer insulator, and features a strong sensitivity to doping as it transitions to a weakly-ferromagnetic and metallic state at only 6% Ce doping. By growing compressively strained thin films on YAlO_3 substrates the sensitivity is increased as the transition occurs at only 2% Ce doping. This metal-insulator transition does not feature any measurable structural change, making CaMnO_3 an ideal platform to study the formation of metallic bands and their interactions with boson in manganites.

3.1 Transport measurements

We performed magnetotransport experiments on thin Ce-doped CaMnO_3 films grown with compressive strain on YAlO_3 . Firstly, the carrier density extracted from the normal Hall effect scales linearly with the Ce doping, and are in good agreement with the expected value considering two electrons per Ce ion doped in the system (Fig. 3.1a). This, together with the chemical shift with doping observed in X-ray absorption spectroscopy (see 2.3), confirms the good stoichiometry of the growth, and that chemical doping directly translates to adding charge carriers to the system.

Fig. 3.1c show the temperature dependence of the resistivity of 20 nm-thick CaMnO_3 thin films on YAlO_3 with various dopings, up to 5% Ce concentration. Undoped CaMnO_3 is completely insulating with a monotonic temperature dependence of the resistivity, in line with its expected charge-transfer insulating state. 1% doped samples features a low-temperature insulating behavior, although with a three orders of magnitude drop compared to the undoped sample, and a metallic behavior at room

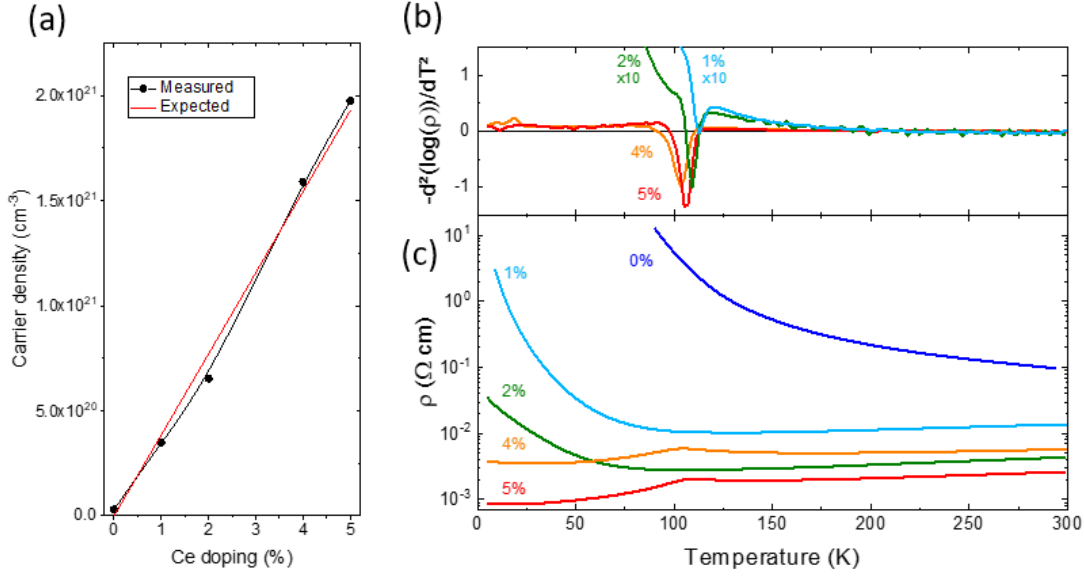


Figure 3.1: (a) Measured carrier density at 300 K of 20 nm thick Ce-doped CaMnO_3 thin films as a function of Ce doping of the target material, compared to the expected value from the nominal doping. Temperature dependence of the resistivity (b) and the second derivative of its logarithm (c) for different doping levels.

temperature. 2% doped CaMnO_3 feature a similar behavior, with lower resistivities. 4% and 5% are fully metallic at low temperature, and show a cusp at ≈ 110 K, a signature of the transition from a low temperature weakly ferromagnetic state to a paramagnetic state at high temperature. The precise transition temperature T_C can be inferred from the temperature dependence of $-d^2 \log(\rho)/dT^2$ (Fig. 3.1b), where a dip signals the transition. The obtained transition temperatures T_C are in the 110 – 115 K range, and decrease by increasing doping from 1% to 4% while increasing slightly as the doping reaches 5%.

Let us now focus on the low temperature resistivity. By increasing the doping CaMnO_3 transitions from an insulator to a metal. However, this transition is not sharp, with 2% doped samples featuring a monotonically decreasing resistivity, although with a magnitude far too low for a proper insulator. An upturn at very low temperatures occurs also in 4% doped samples under 30 nm of thickness. This behavior could be due to antiferromagnetic correlations, which tend to localize carriers, and would be a sign of the smooth transition from an antiferromagnet to a weak ferromagnet. Recently, it has been shown in $\text{La}_{0.7}\text{Sr}_{0.3}\text{MnO}_3$ that an upturn at low temperature could also be a signature of weak localization [144]. The reported effect is relatively smaller magnitude to what we observe, but we should also note that low doping intrinsically brings disorder to the system as the distribution of dopant ions in the crystal lattice is more aleatory the lower the dopings. Thus, the upturn at low temperatures may also signify heterogeneity of the doping, at the nanoscale.

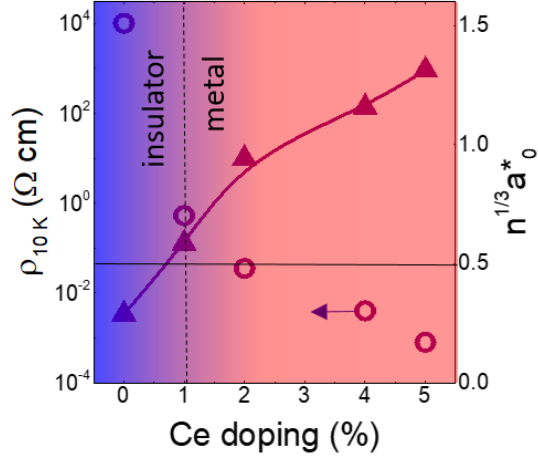


Figure 3.2: Doping dependence of the low-temperature resistivity (circles) and of the Mott parameter $n^{1/3}a_0^*$ (triangles)

A third possibility, suggested by results that we will show in this chapter, is that electron-phonon interactions enhance the mass of the carriers at lower temperatures.

The electronic transition can be clearly seen by plotting the resistivity at 10 K against Ce doping (Fig. 3.2): with only 1% Ce doping we have a four orders of magnitude drop of the resistivity, after which the resistivity decreases in a linear manner down to 5% doping. The $n^{1/3}a_0^*$ parameter is also plotted against Ce doping. The Mott criterion for the metal-insulator transition $n^{1/3}a_0^* > 0.5$ (see 1.2.1.3) is reached at 1% Ce doping.

What these results confirm is that CaMnO_3 is strongly sensitive to doping, reaching a metallic state at only 2% Ce doping when compressively strained. Structural measurements (see 2.2) confirm that throughout all dopings our thin films maintain a coherent strained crystal structure with no visible changes, ensuring that the observed electronic properties of the doped material are purely due to the chemical doping, which populates the conduction band.

3.2 Electronic structure

Preliminary calculations were performed in the orthorhombic Pbnm structure with 20 atoms in the primitive unit cell, using spin-polarized density-functional theory (DFT), as implemented in the Quantum Espresso package [145]. The obtained relaxed crystal structure is an orthorhombically distorted perovskite, shown in Fig. 3.3a, consistent to what was previously determined (see 1.2.1). The calculated density of states shows that the both valence and conduction bands are formed by a combination of Mn t_{2g} and e_g states (Fig. 3.3b). The band structure is shown in Fig. 3.3c, together with the Fermi level shift computed for 2% and 4% doping. What we see is that the

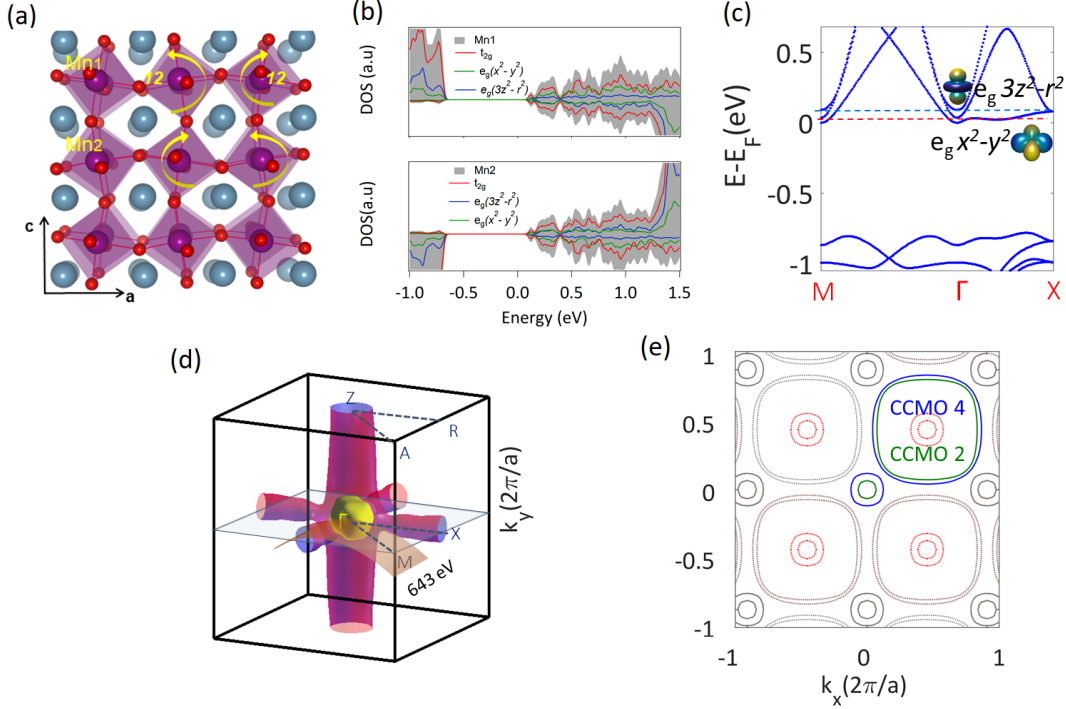


Figure 3.3: Density functional theory calculations of CaMnO_3 : (a) orthorhombically distorted lattice of CaMnO_3 ; (b) Electronic density of states of CaMnO_3 projected onto two Mn atoms with antiparallel spins; (c) band structure and Fermi energy shift of 2% (red) and 4% Ce doping (blue); (d) theoretical Fermi surface unfolded to the pseudocubic-lattice Brillouin zone and (e) its cut along the ΓXY plane; (f) calculated Fermi surface cuts in the ΓYX plane for 2% doping (green lines) and 4% doping (blue), where the doping increases the Luttinger volume.

2% Ce doping pushes the Fermi energy just above the edge of the conduction band, populating it with Mn $e_g x^2 - y^2$ states. Increasing the doping further up to 4% populates the conduction band additionally with Mn $e_g 3z^2 - r^2$ states. In Fig. 3.3d we show the Fermi surface of a 4% Ce-doped CaMnO_3 in the pseudo-cubic Brillouin zone, which consists of an electron sphere around Γ , populated with Mn $e_g x^2 - y^2$ and $3z^2 - r^2$ states, and electron cylinders protruding from Γ , in the x , y , and z directions, populated by Mn $e_g x^2 - y^2$ states. These cylinders are labeled as quasi-2D since the dispersion does not vary by moving along the length of the cylinders, and are characteristic of the electron structure of manganites in general.

A cut of this Fermi surface along the ΓMX plane is shown in Fig. 3.3e, for 2% and 4% doping. The sphere and the cylinders all expand as the doping is increased. This is because the Luttinger volume, i.e. the volume enclosed by the Fermi surface, is proportional to the carriers density. Thus, by increasing doping we increase carrier density and the Fermi surface expands. These Fermi surface cuts also show replicas

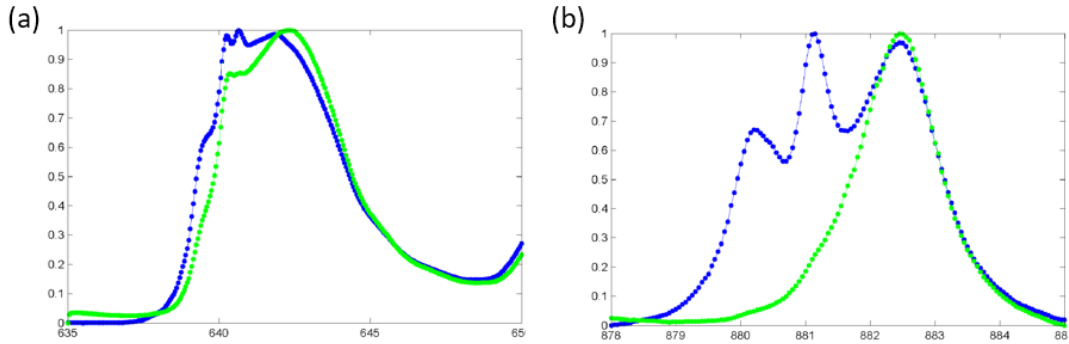


Figure 3.4: (a) Mn 2p and (b) Ce 4f X-ray absorption spectra recorded immediately after the X-ray beam hits the sample (green) and after longer exposure at the intense synchrotron radiation. The components at lower energies associated to Mn²⁺ and reduced Ce states are visible.

of the Γ spheres at the corners of the (pseudo-cubic) Brillouin zone ($\pm\pi/a, \pm\pi/a$). This is due to the orthorhombic distortion, which doubles the unit cell along x and y (and z) in real space, thus halving the unit cell in reciprocal space; the corners of the pseudo-cubic unit cell become the center of the orthorhombic unit cell and develop a Γ electron sphere. These replicas are analogous to those measured in $\text{La}_{1-x}\text{Sr}_x\text{MnO}_3$ [96]. This could be, in principle, due to the unit cell doubling caused by the antiferromagnetic ordering (which splits the lattice in two G-type antiferromagnetically aligned ferromagnetic lattices with doubled unit cell, in the x, y, z). This was confirmed not to be the case, as only the orthorhombic distortion without any magnetic ordering created these Γ electron sphere replicas in these calculations, whereas only antiferromagnetic ordering with no orthorhombic distortion produced no replicas.

We performed angle-resolved photoemission spectroscopy (ARPES) to gain further insights. The experiments were carried out at the ADDRESS beamline at the Swiss Light Source using circularly polarized X-ray beam with a flux of 10^{13} photons/sec/0.01% bandwidth. The samples were grown in our PLD setup, transferred in a high-vacuum case ex-situ, brought to the beamline, and inserted in the ultra-high vacuum ARPES setup. With this procedure, the samples stayed in open air for 5 – 10 minutes total, and showed no sign of contamination when measured. We also tried capping the samples with a thin layer of Pt in order to protect the sample from adsorption and chemisorption of atmospheric particles, but this capping layer also decreased the signal from Ce-doped CaMnO_3 , making any measurement impossible.

Another challenge for these experiments was sample degradation due to radiation damage: X-ray absorption spectra were taken immediately after exposure to the X-ray beam, and then after longer exposure. The spectra after long exposure showed an increase of the Mn²⁺ peak, and reduced Ce states, as shown in Fig. 3.4, signaling sample degradation due to radiation damage. This problem was solved by increasing

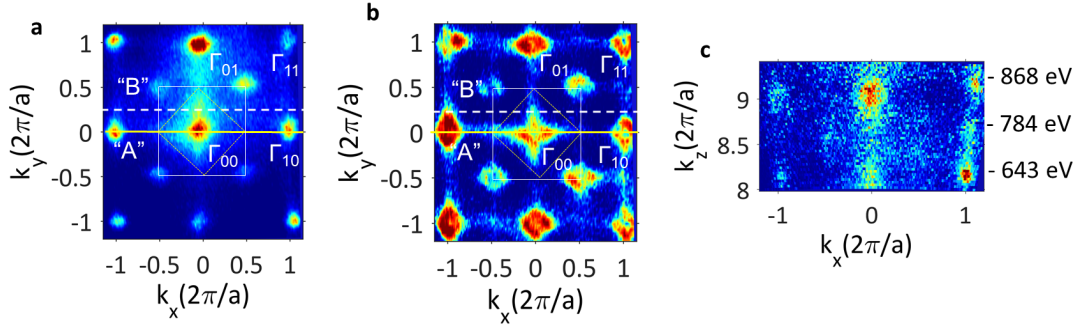


Figure 3.5: Fermi surface maps in the Γ XM plane for 2% (a) and 4% doping (b) measured at $h\nu = 643$ eV. The white square designate the pseudocubic surface Brillouin zone.(c) Out-of-plane Fermi surface map for 2% doping in the Γ ZR.

	3D electrons		Quasi-2D electrons	
Ce (%)	k_F (\AA^{-1})	n (cm^{-3})	k_F (\AA^{-1})	n (cm^{-3})
2	0.10 ± 0.02	$(0.35 \pm 0.06) \times 10^{20}$	0.13 ± 0.02	$(1.2 \pm 0.06) \times 10^{21}$
4	0.20 ± 0.02	$(2.8 \pm 0.06) \times 10^{20}$	0.15 ± 0.02	$(1.6 \pm 0.06) \times 10^{21}$

Table 3.1: Carrier density and Fermi wavevector of the 3D and quasi-2D carriers for 2% and 4% doping.

the oxygen pressure up to 7×10^{-7} mbar, which required modifying the whole beamline setup. Such an oxygen pressure was able to counteract the radiation damage, and the absorption spectra showed no signs of damage even after days of measurements.

The electron structure of CaMnO₃ was probed with a photon energy of $h\nu = 643$ eV. This energy was chosen for its chemical specificity: it increases the signals from the Mn 3d states since it is close to the resonant excitation through the Mn 2p levels. At the same time, it sits close to the Γ point of a Brillouin zone of CaMnO₃, which can be seen in the (k_x, k_z) electron dispersion (Fig. 3.5). At this energy, Fermi surface maps of 2% and 4% Ce doped CaMnO₃ were taken, shown in Fig. 3.5. These maps are in agreement with the theoretical calculations (Fig. 3.3e), as the Fermi surface indeed expands by increasing the chemical doping, and Γ electron sphere replicas are visible at the corners of the pseudo-cubic Brillouin zone.

The carrier densities and Fermi wavevectors are displayed in table 3.1. The carrier densities were computed from the Luttinger volume of the measured Fermi surface. The Fermi wavevector k_F for the 3D carriers in the Γ sphere is well defined, and is simply the radius of the sphere itself. For the quasi-2D electrons there is no well defined k_F ; however it can be extracted from the gradient of the ARPES intensity, integrated through the occupied bandwidth [146]. The quasi-2D carriers have a much high density compared to the 3D one. Notably, the 3D electron have a much sharper increase in density from 2% to 4% doping compared to the quasi-2D carrier.

We studied the properties of each type of carrier by their band dispersion and

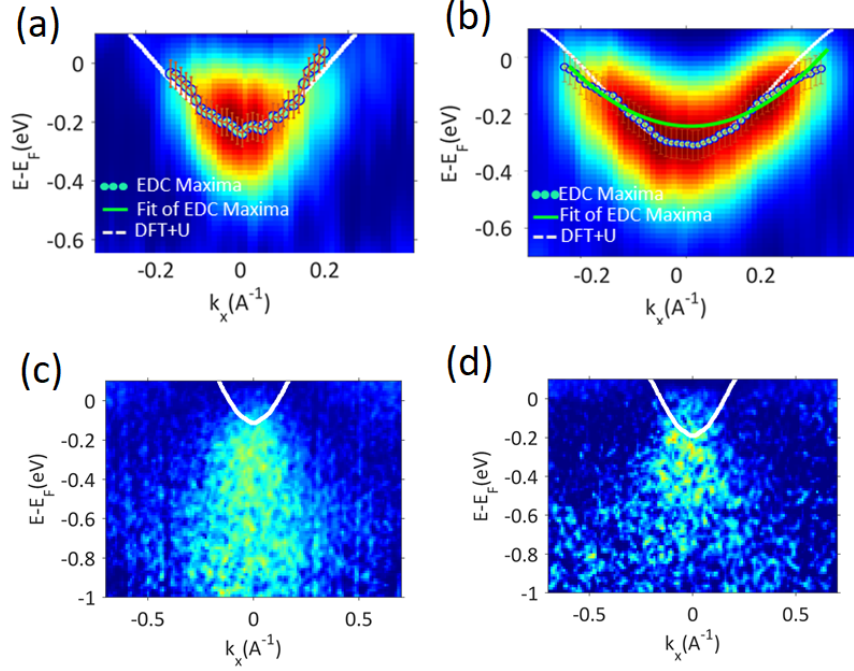


Figure 3.6: Band dispersion of the 3D bands around Γ for (a) 2% and (b) 4% Ce doping, together with the parabolic band from DFT calculations. Energy dispersion of the quasi-2D bands around $k_y = 0.5\pi/a$ for (c) 2% and (d) 4% Ce doping.

spectral functions. For the 3D carriers, the band dispersion was measured by measuring the k_x dispersion in the ΓX direction (cut A in Fig. 3.5a,b). This band dispersion is shown in Fig. 3.6a,b for 2% and 4% doping respectively. These band structures confirm the picture of doping-dependent band filling; the overlaid band calculated by DFT match are shifted to match the experimental k_F , compensating a deviation from the nominal doping by up to 25%. For 2% doping, the measured maxima of the energy distribution curve follows a parabolic curve with $m^* = 0.35m_e$, in agreement with the DFT calculations ($m^* = 0.38m_e$). On the other hand, in the case of 4% doping, at the minimum the band follows a parabolic curve with the same $m^* = 0.35m_e$, but at 80 ± 20 eV from the Fermi energy the band shows a kink, deviating from a parabolic behavior. This kink is indicative of interaction with a bosonic degree of freedom, with an energy ≈ 80 meV. This interaction stiffens the electron and increases its effective mass at energies above the kink. A similar kink may be present even at lower dopings, but is hidden due to the lower occupied bandwidth. Because of this, and due to the possible mixture between the e_g bands that fall into very similar energy ranges, it is not possible to quantify the structure and properties of the kink.

This kink may signify coupling to magnons, however it has been shown that in CaMnO_3 bosons are strongly coupled to phonons, but weakly coupled to electrons [149]. antiferromagnetic magnons in bulk CaMnO_3 have an energy ≈ 20 meV, below the measured kink energy. [150] The magnons associated to the weak ferromagnetism

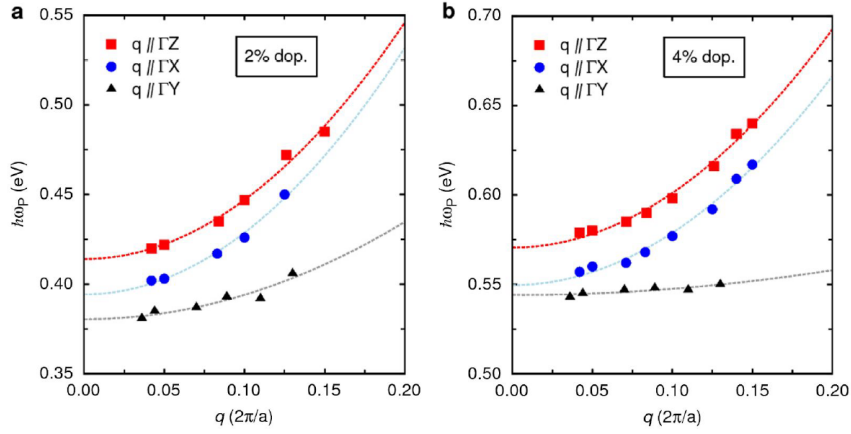


Figure 3.7: Simulated plasmon dispersions in (a) 2% and (b) 4% Ce-doped CaMnO_3 calculated for wavevectors q along the three Cartesian directions of the orthorhombic Brillouin zone.

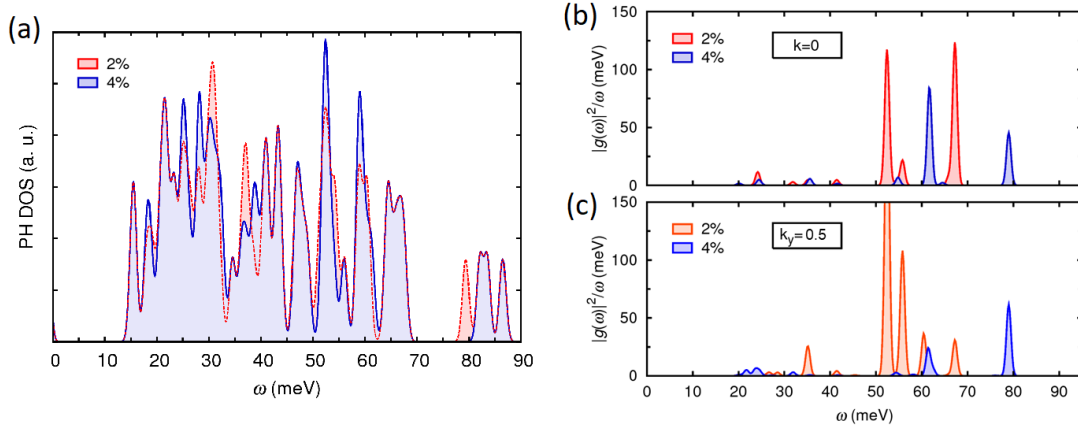


Figure 3.8: (a) Calculated electron-phonon density of states and interaction strength at (b) the Γ point and (c) $k_y = 0.5\pi/a$ points, for 2% and 4% doping.

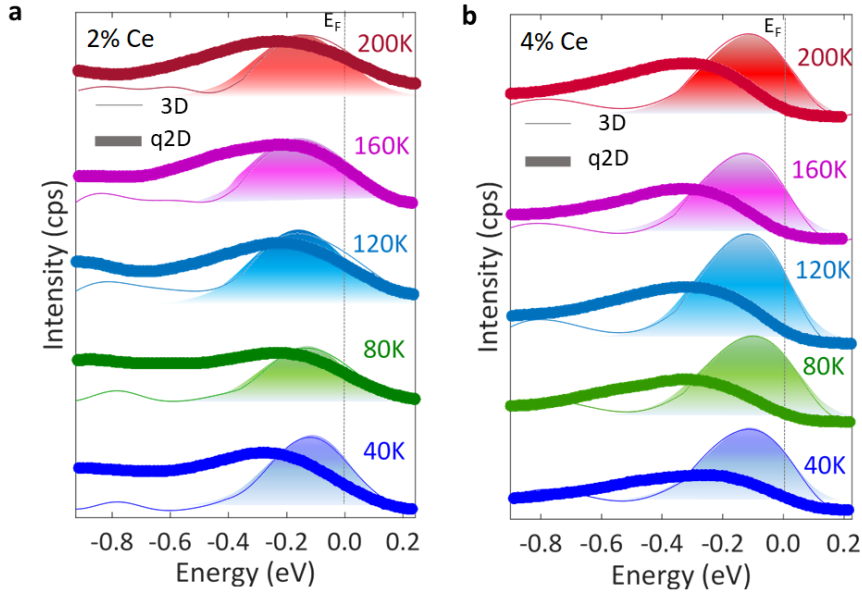


Figure 3.9: Spectral function (obtained by integration of Fig. 3.6) of the quasi-2D and 3D bands for (a) 2% and (b) 4% doping.

of our compressively strained thin films are expected to have an even lower energy, due to the ferromagnetic coupling being weaker than the antiferromagnetic coupling. Thus, magnons can be clearly ruled out as candidates for the electron-boson coupling induced kinks. Plasmons can also be ruled out as DFT calculations show that their energies are higher than 400 meV, much higher than the measured kink energy (Fig. 3.7). Phonons, on the other hand, are a more plausible source of coupling as many phonon modes with high electron-phonon interaction matrix elements are present in the 50 – 80 meV range (Fig. 3.8b), consistently with the experimental data. These combined results strongly suggest that this kink is a sign of electron-phonon interaction, ubiquitous in manganites. The fact that the band structure only manifests a kink, maintaining a band-like dispersion, shows that this electron-phonon interaction is in the light-to-intermediate interaction range and does not strongly enhance the effective mass of these carriers.

To probe the electronic structure of the second, quasi-2D carriers, we measured the k_x dispersion along the cylinders, at the $k_x = \pi/2a$ point (cut B in Fig. 3.5a). The resulting energy dispersion is shown in Fig. 3.6c,d, with the DFT calculations overlaid. These dispersion do not show any kind of band-like appearance, but rather a wide waterfall originating close to the Fermi level E_F . This spectrum, shown in Fig. 3.9 is also different from a sharp, symmetric peak of a well-defined quasi-particle, with a small quasi-particle weight (i.e. the area underlying the peak). This asymmetric waterfall extending down into the energies of the valence band is a signature of strong coupling between electrons and multiple bosonic degrees of freedom [147]. The

associated bosons are phonons, which interact strongly with the carriers and, as the carriers move they drag along the lattice distortion, increasing the effective mass of the electrons [148]. The resultant quasi-particles are polarons.

Since multiple phonon modes can be coupled to the carriers, the quasi-particle peak is distorted and loses definition. In other words, the wider the dispersion of the phonon modes, the wider the dispersion of the electron structure. Short-range phonons are confined in real space, and thus their k -space dispersion is broad and not well-defined. On the other hand, long-range phonons are dispersed in real space, and thus their k -space distribution is confined. As the polaron waterfall is confined in k -space, the associated phonon dispersion must be confined as well, strongly suggesting that the coupled phonons are long-range [147].

A more rigid proof of the long-range character would require the knowledge of the dispersion and overlap of different phonon modes to then compare the phonon spectral weight to the polaron spectral weight. However, the doping dependence of the polaron spectra (Fig. 3.9) shows that as the doping increases, the peaks shift upwards and the total spectral weight is reduced. This indicates that the electron-phonon interaction strength is reduced as the doping increases, since there is no significant change in the phonon density of states between the two dopings which could be behind this change (see Fig. 3.8a).

Electron-phonon interaction can be screened by the electrons themselves. If the plasma energy ω_{pl} is higher than the energy of a phonon mode ω_{ph} , the coupling to this phonon mode is screened; otherwise no screening occurs. The change in spectral weight with doping can be explained by this screening: light 3D electrons are more effective at screening the electron-phonon interaction due to their higher plasma frequency ($\omega_{pl} \propto 1/\sqrt{m^*}$) than the q2D heavy polarons. These electrons do not only screen the interaction with themselves but take part in the screening of both electron bands. Thus, by increasing the doping from 2% to 4%, the carrier density of the 3D electrons increases by an order of magnitude and contribute more to the screening of the electron-phonon interaction of the polarons, reducing their spectral weight.

3.3 Carrier-dependent electron-phonon coupling

In the previous section we show a stark difference in electron-phonon interaction between the two families of carriers. This can occur when the electron-phonon interaction is not constant for different wave functions, however our DFT calculations do not show any substantial difference between the matrix elements of the quasi-2D and 3D carriers (Fig. 3.8b,c). This is consistent with the similar orbital composition of the wavefunctions of the two carriers.

Our DFT calculations, as the vast majority of electron-phonon interaction calcula-

tions, use many-body perturbation theory and rely on the Migdal approximation, i.e. neglecting higher order terms of the Feynman-Dyson expansion (called vertex corrections), using only the lowest order [151]. Migdal's theorem states that this approximation is valid in metals, where the vertex correction is of the order of $\sqrt{m/M} < 10^{-2}$, where m is the mass of the carriers and M the mass of the crystal ions. The approximation is also valid in insulators and semiconductors [152], however Migdal's theorem can face problems when these are heavily doped, where $\Delta\epsilon_F$ (the bandwidth between the Fermi energy E_F and the bottom of the occupied conduction band) can become of the order of magnitude (or smaller of) the characteristic phonon energy ω_0 of the interacting phonon modes. Under these conditions, called non-adiabatic, Migdal's theorem does not hold anymore as there are higher order terms of the vertex correction of the order $\omega_0/\Delta\epsilon_F$ [153, 154]. This has been confirmed numerically by many-body Bold Line Diagrammatic Monte Carlo simulations which show that the vertex correction become non-negligible when $\Delta\epsilon_F = \omega_{ph}$ [159].

Thus we need to compare the relative Fermi energy $\Delta\epsilon_F$, measured with respect to the bottom of the valence band, to the energy of the active phonon modes $\omega_{ph} \approx 50-80$ meV. In the case of 3D bands, $\Delta\epsilon_F > \hbar\omega_{ph}$ and so the Migdal approximation holds and we are able to experimentally visualize the band structure in the presence of moderate coupling (i.e. the kinks). As one moves from Γ toward X, the valence band moves significantly upwards (Fig. 3.3c) and we reach the condition $\Delta\epsilon_F \approx \hbar\omega_{ph} = 80$ meV. Density functional theory simulations show that this upward shift is driven by correlations, as increasing the Hubbard U increases the shift itself. Thus, electron correlations reduce $\Delta\epsilon_F$ for the quasi-2D band. Here the Migdal approximation does not hold, so the electron-phonon coupling strength is enhanced due the now non-negligible vertex corrections.

Multi-band correlated systems can show different mass renormalization for carriers originating from different bands, as it features characteristic phonon energies close to that of the Fermi energy E_F , and at the same time distant from other bosonic degrees of freedom. However, this is normally directly caused by band-dependent correlations. To our knowledge, Ce-doped CaMnO_3 is the first material to have different effective masses for different carriers due to a band-dependent electron-phonon interaction. This is also an experimental confirmation that vertex corrections are indispensable to capture the strong coupling regime of polaronic renormalization, when $E_F \approx \omega_{ph}$, as predicted theoretically [159, 165].

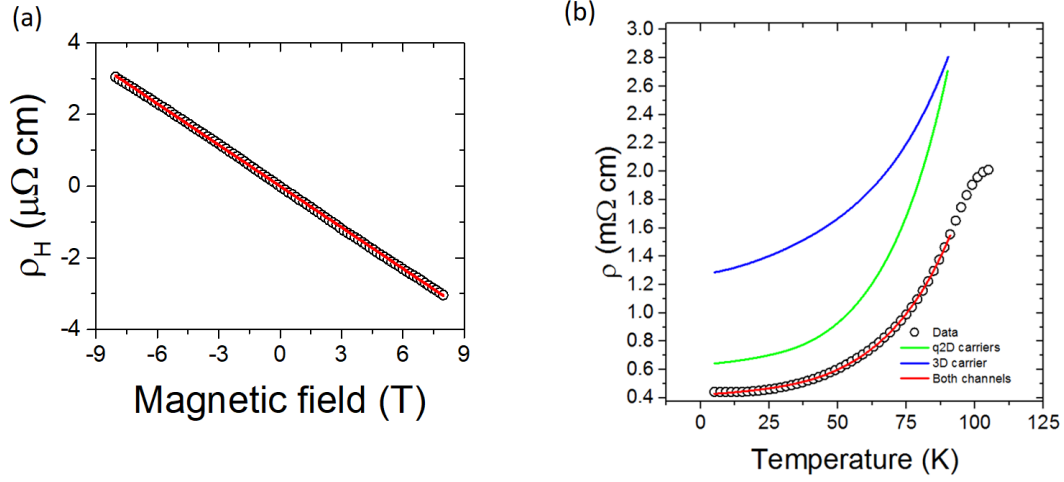


Figure 3.10: (a) Hall effect for a 30 nm 4% Ce-doped sample at 130 K, and its simulation with $n = 2.8 \times 10^{20} \text{cm}^{-3}$ and $\mu = 9.9 \text{ cm/Vs}$ for the light-carrier channel, and $n = 1.6 \times 10^{21} \text{cm}^{-3}$ and $\mu = 3.6 \text{ cm/Vs}$ for the heavy-carrier one. (b) Temperature dependence of resistivity of the same sample, and its fit using a two-band model with the light- and heavy-carrier channels plotted together with the individual contributions of the channels.

3.4 Light and heavy charge carriers in transport

One common way of probing the effect of two different bands in transport is by measuring the Hall effect. Each band is associated to its resistivity tensor

$$\boldsymbol{\rho}_i = \begin{pmatrix} \rho_i & \rho_i^H \\ -\rho_i^H & \rho_i \end{pmatrix} \quad (3.1)$$

where $i = 1, 2$ indicates the band. ρ_i is the longitudinal resistivity and ρ_i^H is the transverse (Hall) resistivity. The total resistivity tensor is

$$\boldsymbol{\rho}^{-1} = \boldsymbol{\rho}_1^{-1} + \boldsymbol{\rho}_2^{-1} = \begin{pmatrix} \rho & \rho^H \\ -\rho^H & \rho \end{pmatrix} \quad (3.2)$$

where

$$\rho = \frac{\rho_1 \rho_2 (\rho_1 + \rho_2) + \rho_1 (\rho_2^H)^2 + \rho_2 (\rho_1^H)^2}{(\rho_1 + \rho_2)^2 + (\rho_1^H + \rho_2^H)^2} \quad (3.3)$$

$$\rho^H = \frac{\rho_1 (\rho_2^H)^2 + \rho_2 (\rho_1^H)^2 + \rho_1^H \rho_2^H (\rho_1^H + \rho_2^H)}{(\rho_1 + \rho_2)^2 + (\rho_1^H + \rho_2^H)^2}. \quad (3.4)$$

3.4.1 Hall resistivity

In the case of normal Hall effect ($\rho_i^H(B) = B/n_i q$, with n_i the carrier density of the i -th band and $q = \pm e$ the charge of its carriers), by inserting $\rho_i = 1/n_i \mu_i e_i$, with μ_i the mobility of the i -th band, we obtain

$$\rho^H(B) = \frac{B}{q} \frac{n_1 \mu_1^2 + n_2 \mu_2^2 + (n_1 + n_2)(\mu_1 \mu_2 B)^2}{(n_1 \mu_1 + n_2 \mu_2)^2 + (n_1 + n_2)^2 (\mu_1 \mu_2 B)^2}. \quad (3.5)$$

This approach also considers the longitudinal resistivities as constants, i.e. assuming that these longitudinal resistivities vary much slower than the transverse resistivities. This assumption generally holds in oxides, and this equation is able to explain nonlinearities present in the Hall effect of LaAlO₃/SrTiO₃ interfaces [155].

Fig. 3.10a shows the Hall effect of a 30 nm thick, 4% doped sample. This curve can be simulated with Eq. 3.5 using values obtain from the ARPES measurements (table 3.1), with the heavy quasi-2D carriers' mobility smaller by a factor ≈ 3 compared to the light 3D carriers. This is consistent with the obtained effective masses of the two carriers: the 3D carriers have an effective mass $m^* = 0.35$ (Fig. 3.6) while the quasi-2D polarons have an effective mass that can be estimated as $m^* \approx 1$ (from DFT) and $m^* \approx 1.5$ (from the calculated electron-phonon interaction strength in Fig. 3.8), giving a ratio between the two masses $\approx 3 - 4$.

3.4.2 Longitudinal resistivity in the low temperature ferromagnetic phase

The longitudinal resistivity can also be interpreted in the framework of two separate carriers. In the low-temperature metallic and weakly ferromagnetic phase, doped CaMnO₃ is metallic due to its delocalized carriers. The quasi-2D polarons are subject to scattering with impurities, magnons and phonons, all the while under the influence of strong electron-phonon interaction that forms the polarons themselves. The effect of this electron-phonon interaction is a temperature-dependent enhancement of the effective mass:

$$m^* = m_0 \exp[g^2 \coth(\hbar\omega_0/2k_B T)] \quad (3.6)$$

where m_0 is the bare carrier mass, g^2 the band narrowing factor and $\hbar\omega_0$ the energy of the softest coupled phonon mode. This mass enhancement is caused by a strong band renormalization, which causes the conventional electron-phonon scattering to fail. In this situation, the scattering rate of the polaron is dominated by the softest coupled phonon mode:

$$\frac{1}{\tau} = \frac{A_0 \omega_0}{\sinh^2(\hbar\omega_0/2k_B T)} \quad (3.7)$$

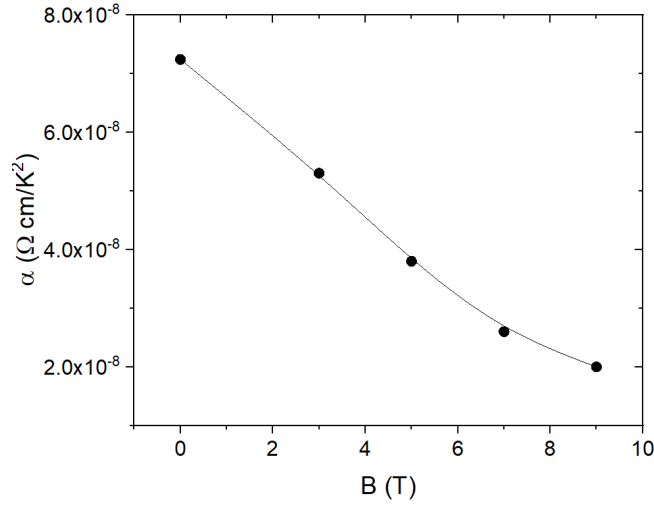


Figure 3.11: Electron-electron scattering coefficient α plotted as a function of applied magnetic field.

with A_0 a constant that depends on the conduction band width and the strength of the electron-phonon interaction.

As in other spin-polarized materials, electron-magnon scattering is present. This mechanism gives rise to a αT^ν power law, where $\nu = 2$ conventionally. The presence of this power law in the resistivity of manganites has also been attributed to electron-electron scattering. CaMnO₃ is a strongly correlated material so, in principle, one could expect electron-electron scattering to contribute to the low-temperature resistivity of the material. The electron-electron resistivity parameter α is empirically related with the coefficient of the electronic specific heat γ by the Kadowaki-Woods relation $\alpha/\gamma^2 \approx 1 \times 10^{-5} \mu\Omega \text{ cm} (\text{mole K/mJ})^2$ [70]. The parameter α for both carriers of CaMnO₃ can be extracted at low temperatures, where electron-phonon interaction can be neglected [156], obtaining $\alpha = 8 \times 10^{-8} \Omega \text{ cm/K}^2$ (with the procedure than we will subsequently describe). In manganites $\gamma \approx 1 - 10 \text{ mJ/mole K}^2$, and in particular in La_{1-x}Ca_xMnO₃ $\gamma = 5 \text{ mJ/mole K}^2$. With these values we see that our coefficient α is more than two orders of magnitude larger than the expected Kadowaki-Woods parameter γ . In addition, applying a strong magnetic field would enhance electron-electron scattering so one would expect that such mechanism would cause the α parameter to increase with increasing magnetic field. However, in our Ce-doped CaMnO₃, α is monotonically decreasing with the field (Fig. 3.11). Thus, this magnitude and trend of the parameter α are inconsistent with electron-electron scattering, and can be interpreted as electron-magnon scattering [72].

As mentioned before, electron-magnon scattering gives rise to a T^ν power law in the resistivity, with $\nu = 2$ conventionally. However, in the presence of strong Hund coupling this exponent becomes $\nu = 1.5$ [157]. As CaMnO₃ features such strong Hund

coupling ($J_H \approx 1$ eV), we expect an electron-magnon scattering contribution to the resistivity with a $T^{1.5}$ power law. By combining all of these elements we obtain the temperature dependence of the resistivity of the quasi-2D polarons:

$$\rho^{q2D}(T) = \rho_0^{q2D} + \rho_{1.5}^{q2D} T^{1.5} + \rho_{e-ph} \frac{\omega_0}{\sinh^2(\hbar\omega_0/2k_B T)} \exp[g^2 \coth(\hbar\omega_0/2k_B T)] \quad (3.8)$$

where ρ_0 accounts for the temperature-independent impurity scattering. A similar expression was first used to reproduce the resistivity of $\text{La}_{0.67}\text{Sr}_{0.33}\text{MnO}_3$ [81], although we note that it used an electron-magnon contribution T^2 rather than $T^{1.5}$.

The light 3D carrier do not exhibit an electron-phonon interaction strong enough to renormalize the band and enhance their mass. Thus, in this case electron-phonon scattering should exhibit a conventional contribution of T^5 , as the Bloch-Grüneisen temperature of CaMnO_3 is $\Theta_{BG} = 2\hbar v_S k_F / k_B \gtrsim 300$ K is much higher than the range of temperatures that we consider here ($v_S = 5$ km/s is the speed of sound in CaMnO_3 [163]). This power law is applicable in the case of 3D carriers since they have the required spherical Fermi surface [66]. Electron-magnon scattering should behave the same as in the case of the quasi-2D carrier and would thus contribute with the same $T^{1.5}$ power law. We thus have:

$$\rho^{3D} = \rho_0^{3D} + \rho_{1.5}^{3D} T^{1.5} + \rho_5^{3D} T^5. \quad (3.9)$$

These two expressions can be combined together to obtain the total resistivity of the material with Eq. 3.3. Since the longitudinal resistivity is in the order of $\text{m}\Omega$ cm while the Hall resistivity is in the order of $\mu\Omega$ cm, this expression reduces to

$$\frac{1}{\rho} = \frac{1}{\rho^{q2D}} + \frac{1}{\rho^{3D}}, \quad (3.10)$$

which corresponds to simple parallel between two independent channels.

This way, the two combined expressions have a total of eight free parameters, too many to properly fit our data. The dominant phonon energy for the polarons can be obtained from the transition temperature: $\hbar\omega_0 = 2k_B T_t = 20$ meV [71], similarly to other orthorhombic manganites [160]. This value is also consistent with Raman measurements of CaMnO_3 [161], which show an $A_g(2)$ mode with energy $\hbar\omega = 19$ meV.

Further constraints can be put on the coefficients of the two carriers for the same scattering mechanisms. From Matthiessen's rule

$$\frac{\rho_\alpha^{3D}}{\rho_\alpha^{q2D}} = \frac{m^{3D}}{m^{q2D}} \frac{n^{q2D}}{n^{3D}} \frac{\tau_\alpha^{q2D}}{\tau_\alpha^{3D}} \quad (3.11)$$

where τ represent the scattering time of the mechanism with $\alpha = 0$ for impurity

Carrier	ρ_0	$\rho_{1.5}$	ρ_5	ρ_{e-ph}	g^2
q2D	19.1	0.015		0.02	3.4
3D	38.2	0.03	6.3×10^{-9}		

Table 3.2: Fit parameters for the transport data. ρ_0 is in m Ω cm, $\rho_{1.5}$ in m Ω cm/K^{1.5}, ρ_{e-ph} in m Ω cm s, and g^2 is dimensionless.

scattering and $\alpha = 1.5$ for magnon scattering. If we assume that the scattering rates are the same for the two different carriers (for the electron-magnon scattering this equates to assuming that the scattering rate does not depend on the position on the Brillouin zone of the carriers), we obtain:

$$\frac{\rho_\alpha^{3D}}{\rho_\alpha^{q2D}} = \frac{m^{3D}}{m^{q2D}} \frac{n^{q2D}}{n^{3D}} = 2, \quad (3.12)$$

using the carrier densities from table 3.1 and assuming a ratio of the carriers ≈ 3 .

This model can be used to fit the longitudinal resistivity of a 30 nm thick, 4% doped CaMnO₃ sample. The fits are shown in Fig. 3.10 and the fitting parameters are in table 3.2. The fitted values are in agreement with literature [81]. What we can surmise from the fit is that the quasi-2D polarons dominate transport, in spite of their enhanced mass, due to their much larger carrier density compared to the 3D carriers.

This model cannot be applied for lower dopings of CaMnO₃ as lowering the doping close to the metal-insulator transition causes an upturn of the resistivity close to 0 K. This could be caused by localization of the carriers due to the disorder caused by the low doping, antiferromagnetic correlations that become stronger as the system approaches the antiferromagnetic phase, or an increase of the strength of the electron-phonon interaction at lower temperature. A deeper understanding of these phenomena is needed to fit the resistivities of lower dopings.

3.4.3 Longitudinal transport in the high temperature paramagnetic phase

In the paramagnetic regime above the transition temperature, we use the charge carrier collapse theory. In this regime, the resistivity obeys the equation

$$\rho = \rho_0 T \exp\left(-\frac{\Delta}{2k_B T}\right) \quad (3.13)$$

where Δ is the bipolaron binding energy. These bipolarons are typically immobile in manganites, but in materials with lower coupling such as cuprates [158], bipolarons can become mobile. This is reflected in Eq. 3.13, which features a metal-insulator transition at $T = \Delta/2k_B$. This is due to the thermal excitations that, at this temperature, become large enough to overcome the bipolaron binding (which favors localized

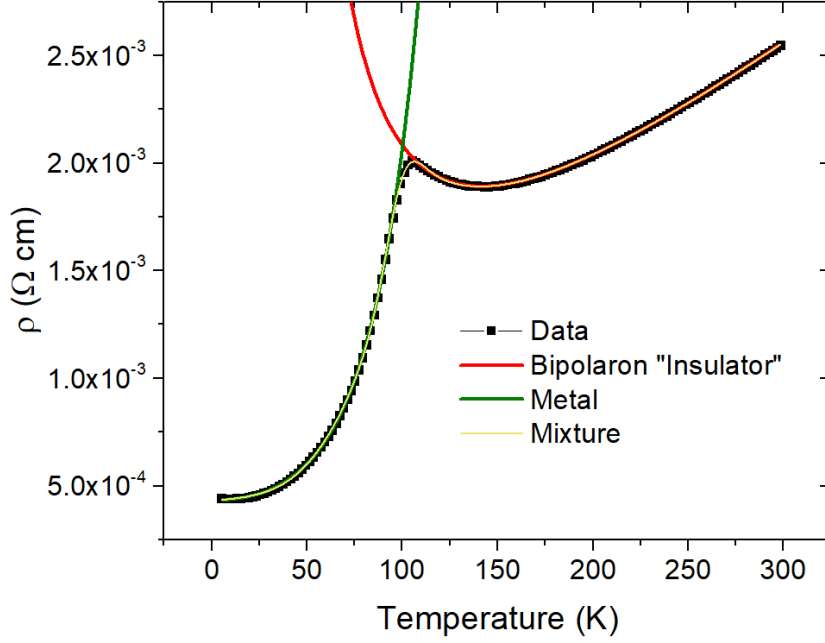


Figure 3.12: Temperature dependence of a 30 nm-thick 4% Ce-doped CaMnO_3 thin film, together with its low-temperature fit (Eq. 3.10), high-temperature fit (Eq. 3.13), and mixture (Eq. 3.14).

carriers).

The high temperature phase of 4% doped CaMnO_3 can be fit with this model (Fig. 3.12), subtracting a constant to correct the offset, obtaining $\Delta = 19$ meV. While the material does not feature a full metal-insulator transition, the bipolaron model is able to accurately describe the resistivity of the paramagnetic phase, with a crossover at $\Delta/2k_B = 135$ K. Thus, the electronic phase transition that occurs concurrently with the magnetic transition at T_C can be better understood as a polaron-bipolaron transition rather than necessarily a metal-insulator transition.

These two models can be combined into one single expression [158]

$$\rho(T) = \rho_M^{f(T)}(T) \cdot \rho_B^{f(T)}(T) \quad (3.14)$$

where $\rho_M(T)$ is the fit of the low temperature weakly ferromagnetic and metallic phase, $\rho_B(T)$ the fit of the high temperature paramagnetic bipolaron phase, and

$$f(T) = \left\{ \frac{1}{2} \left[1 - \operatorname{erf} \left(\frac{T - T_C}{T} \right) \right] \right\}^\varsigma \quad (3.15)$$

represent the fraction of the metallic phase, with ς is the non-ideality exponent [81] that takes into account the possible phase separation known to happen in transitions in manganites [162, 164]. This mixture is shown in Fig. 3.13.

In this high-temperature region we have not considered the light 3D carriers, but rather only the quasi-2D polarons. This is not only because polarons have been shown to dominate transport (Fig. 3.10), but also because the 3D carriers have a smaller electron-phonon coupling which cannot drive a transition such as polaron-bipolaron. As such, the resistivity of this single band will continue to increase monotonically after T_C , reducing its relative contributing compared to the quasi-2D polarons and becoming negligible after T_C .

Chapter 4

Giant topological Hall effect in electron-doped CaMnO_3 thin films

In 1.2.4 we showed the increasing interest of scientists in topological structures in manganites, and in this chapter we show how Ce-doped CaMnO_3 is an interesting candidate to study topological phenomena in manganites. While CaMnO_3 is an insulating antiferromagnet, upon doping by only a few percent of Ce in the Ca site, the material transitions to a metallic and weakly ferromagnetic state (see 1.2.5). Additionally, Ce-doped CaMnO_3 thin films grown on YAlO_3 substrates are compressively strained, leading to high magnetocrystalline anisotropy that dominates, causing the small net magnetization to be out of plane (as shown in 2.4). With high anisotropy K_u and low magnetization M_s , the condition

$$\frac{2K_u}{\mu M_S^2} > 1 \quad (4.1)$$

for the nucleation of topological bubbles during magnetization reversal [2, 107] is easily met. The coexistence of metallicity and perpendicular anisotropy makes Ce-doped CaMnO_3 a good candidate to study topological magnetic configurations in manganite thin films.

4.1 Hall effect measurements and isolation of the topological Hall effect

4.1.1 Hall effect of a 4% Ce-doped CaMnO_3 thin film

We performed transverse resistivity measurements as a function of temperature, for 20 nm samples of different doping grown on YAlO_3 . What we have consistently seen in these measurements is that there is always an additional contribution of longitudinal

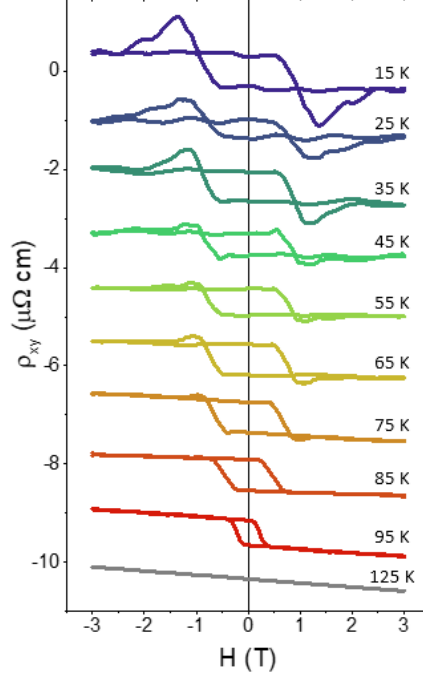


Figure 4.1: Anomalous and topological Hall effect at different temperatures up to 95 K for the 4% doped sample. Normal Hall effect at 125 K. The data are shifted vertically for clarity.

resistivity in our Hall resistivity, due to imperfections in the geometry of the Hall bar inherent to the optical lithography process. Practically, what we measure is

$$\rho = \rho_{xy} + \alpha\rho_{xx}, \quad (4.2)$$

where ρ_{xy} is the proper Hall resistivity, ρ_{xx} is the longitudinal resistivity and α is a constant factor. To separate the two contributions, we can use the fact that the two resistivities have different symmetries: ρ_{xy} is antisymmetric (i.e. $\rho_{xy}^{\uparrow}(H) = -\rho_{xy}^{\downarrow}(-H)$) and ρ_{xx} is symmetric (i.e. $\rho_{xx}^{\uparrow}(H) = \rho_{xx}^{\downarrow}(-H)$). So, to extract the Hall part,

$$\rho_{xy}^{\uparrow}(H) = \frac{\rho^{\uparrow}(H) - \rho^{\downarrow}(-H)}{2} \quad (4.3)$$

$$\rho_{xy}^{\downarrow}(H) = -\rho_{xy}^{\uparrow}(-H) = \frac{\rho^{\downarrow}(H) - \rho^{\uparrow}(-H)}{2} \quad (4.4)$$

The resulting ρ_{xy} of the 4% Ce-doped CaMnO_3 thin film are shown in Fig. 4.1. From room temperature down to 130 K, the Hall signal is linear with a negative slope, consistent with n-type transport. The obtained carrier density is $n = 1.7 \cdot 10^{21} \text{ cm}^{-3}$, close to the nominal value of $1.55 \cdot 10^{21} \text{ cm}^{-3}$ for 4%, assuming that each Ce ion brings two electrons. Below T_c , the Hall signal develops a hysteretic component (see 95 K). This component follows the magnetization, and is the anomalous Hall effect of

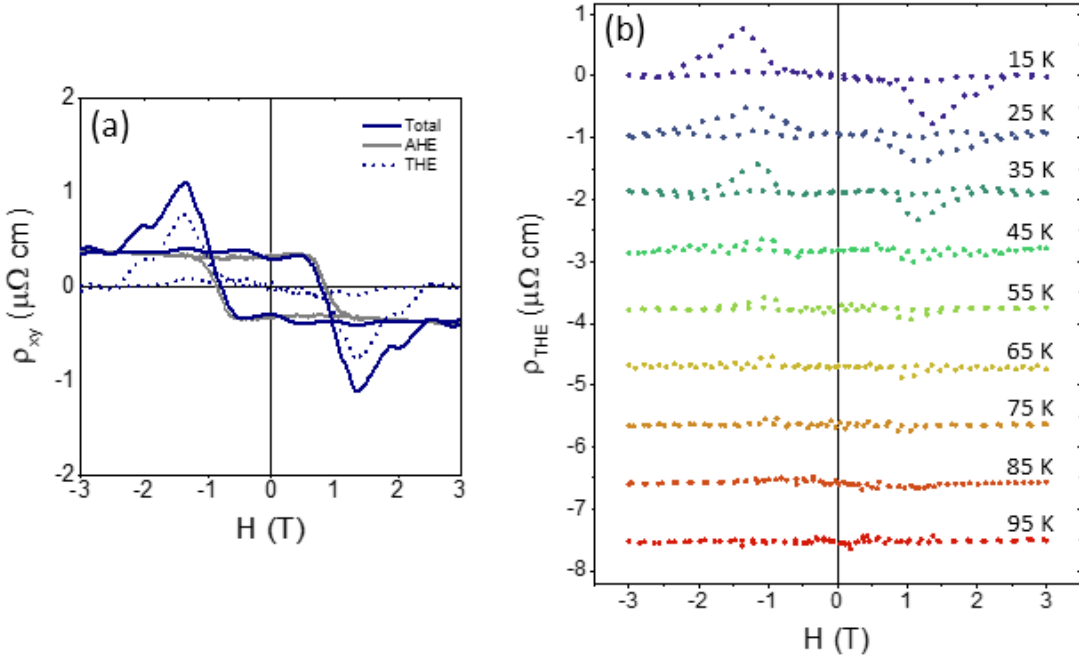


Figure 4.2: (a) Decomposition of the Hall effect into the anomalous Hall effect and the topological Hall effect using Kerr ellipticity data, at 15 K. (b) Extracted topological Hall effect at different temperatures for the 4% doped sample. The data are shifted vertically for clarity.

a perpendicularly magnetized samples (see 1.1.2.2). At even lower temperatures (see 75 K and below), a third component appears in the form of two antisymmetric peaks centered around 1 T. This third component has the peculiar shape of the topological Hall effect described in section 1.1.2.1. Thus in these samples the Hall resistivity comprises three parts:

$$\rho_{xy} = R_0 H + R_S M + \rho_{\text{THE}} \quad (4.5)$$

To study the third topological contribution we have to remove the first two: we can subtract the normal Hall effect simply by subtracting a high field slope, and to subtract the anomalous Hall effect we used magneto-optic Kerr effect measurements on the very same sample to obtain the magnetization loop (see 2.4).

4.1.2 Topological Hall extraction and phase diagram

Having measured the magnetization of the sample shown above with MOKE (see 2.4), we can now use it to subtract the anomalous Hall effect, which is proportional to the magnetization itself. The decomposition is shown in Fig. 4.2a, and the extracted topological Hall effect from Fig. 4.1 is in Fig. 4.2b. We can see that the field corresponding to the maximum of the topological Hall peak decreases with increasing temperature, following the coercive field. Its amplitude decreases with heating as well,

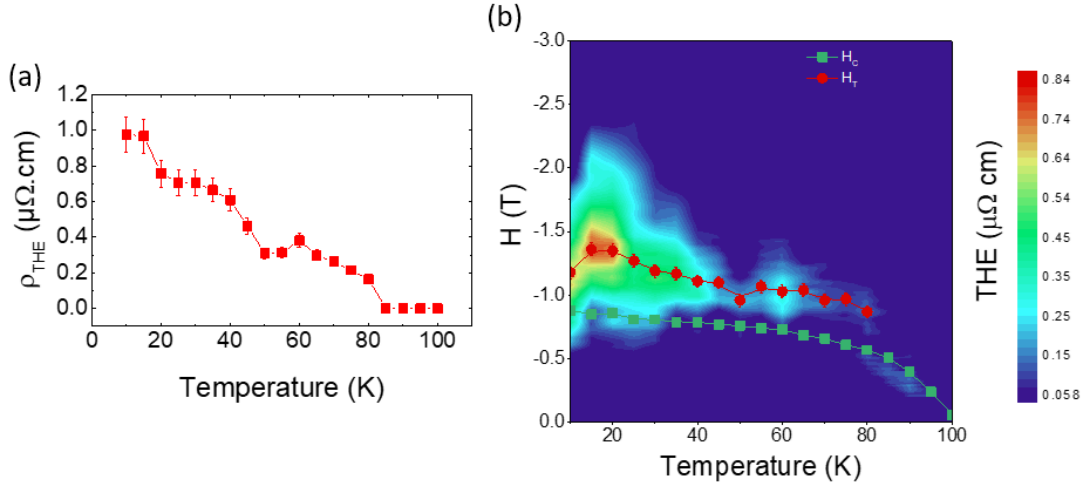


Figure 4.3: (a) Temperature dependence of the topological Hall resistivity. (b) Topological Hall effect vs temperature and magnetic field. The temperature dependence of the coercive field H_C and the position of the topological Hall effect maximum H_T are shown as green and red symbols, respectively.

disappearing between 75 and 95 K.

The maximum amplitude of the topological Hall effect, plotted against temperature in Fig. 4.3a, shows a nearly monotonic decrease with temperature. The topological Hall effect data for all temperatures can be combined in a 3D plot shown in Fig. 4.3b. The topological Hall effect peaks around 1 T at low temperature, and extends to 80 K where it disappears. The position of the topological Hall effect maximum H_T follows the trend in temperature of the coercive field H_C , as it is always shifted by ≈ 0.5 T from it.

4.1.3 Strain dependence of the topological Hall effect

We grew thin films of Ce-doped CaMnO_3 on NdAlO_3 substrates in order to probe the influence of lattice mismatch on the observed topological Hall effect, since epitaxial strain influences the magnetic properties of Ce-doped CaMnO_3 [125]. In Fig. 4.4 we show the Hall effect of a 22 nm-thick 4% Ce-doped CaMnO_3 thin film. Here, a clear anomalous Hall effect is visible under the transition temperature $T_C = 115$ K, but no topological Hall effect is present. On NdAlO_3 the compressive strain is much weaker than on YAlO_3 , although it is enough to induce an out-of-plane magnetization. Nonetheless, the weaker compressive strain induces a weaker anisotropy, which plays a role in stabilizing topological structures (see Eq. 4.1). This preliminary result shows how the topological Hall effect in manganites may be tunable by strain.

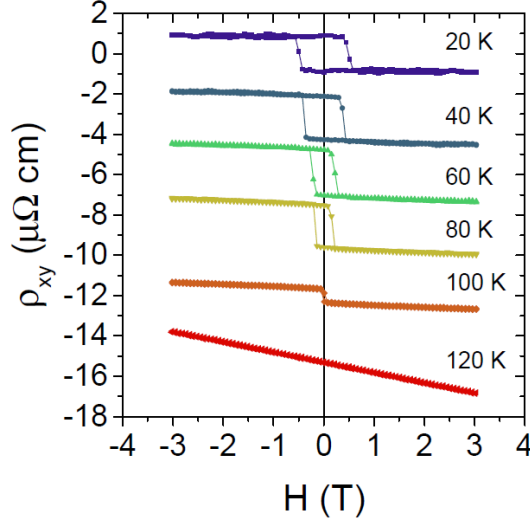


Figure 4.4: Hall effect in a 22 nm 4% Ce doped CaMnO_3 film grown on NdAlO_3 .

4.2 Micromagnetism of CaMnO_3 : interpretation of the topological Hall effect

Why does this topological Hall effect emerge? In 1.1.2.1 we showed how topological Hall effect is a result of charge carriers traveling through topological charges, i.e. spin configurations that vary in space with a non-zero winding number. Fig. 4.3b suggests that these topological charges are nucleated close to magnetization reversal. We have thus considered possible sources of topological charge, namely, Cerium doping (a heavy element that can create DMI), interface-induced DMI or global DMI (induced by a non-centrosymmetric crystal structure):

- Ce doping is a heavy element and it may be possible that it creates DMI and thus a non-collinear structure. However, this can be discarded because X-ray absorption spectroscopy data reveals that Ce is 4+ and thus has no f electrons (see 2.3). Also the period of such a non-collinear structure induced by Ce should decrease with Ce concentration and thus contribute more to the topological as Ce content increases, in contradiction with the experimental results (as we will show in the following section).
- Global DMI: The absence of any signal in Second Harmonic Generation experiments implies that the material is centrosymmetric and thus cannot possess a long-range non-collinear magnetic order as in non-centrosymmetric magnets including B20 alloys, MnP (fan structure) or hexagonal Mn_5Si_3 that all exhibit topological Hall effect. In addition, we have performed resonant magnetic X-ray diffraction experiments at the Mn L edge, and explored a broad area in reciprocal space to search for a possible long-range spin order, without success. Similar

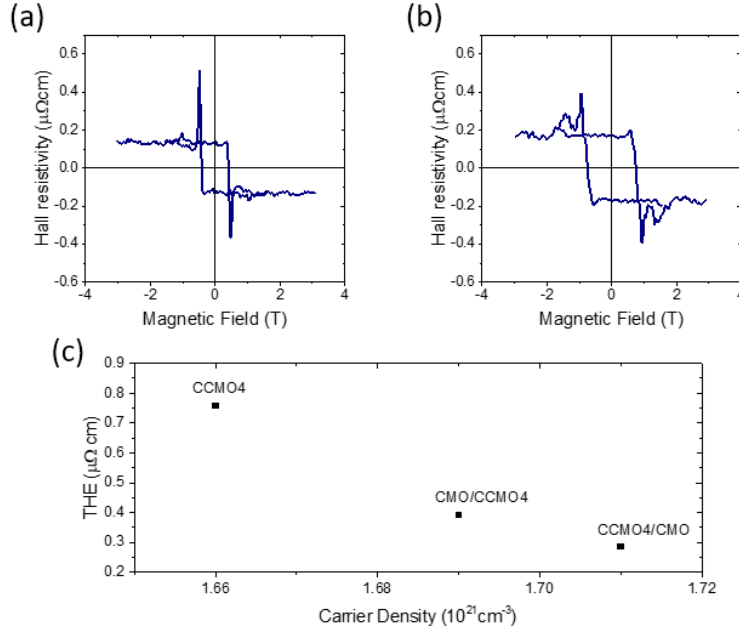


Figure 4.5: Hall effect of (a) CaMnO_3 (20 nm)/ $\text{Ca}_{0.96}\text{Ce}_{0.04}$ (20 nm)// YAlO_3 and (b) $\text{Ca}_{0.96}\text{Ce}_{0.04}$ (20 nm)/ CaMnO_3 (20 nm)// YAlO_3 bilayers measured at 20 K. (C) Amplitude of the topological effect at 20 K of 20 nm-thick bilayers of CaMnO_3 and $\text{Ca}_{0.96}\text{Ce}_{0.04}\text{MnO}_3$, and of bare $\text{Ca}_{0.96}\text{Ce}_{0.04}\text{MnO}_3$, plotted as a function of the measured carrier density.

experiments on 30 nm BiFeO_3 films however clearly revealed the signature of the 70 nm cycloid present in this material, ruling out experimental sensitivity as the reason for the absence of a signal for $(\text{Ca,Ce})\text{MnO}_3$.

- **Interface-driven DMI:** We performed similar Hall experiments on $\text{Ca}_{0.96}\text{Ce}_{0.04}\text{MnO}_3/\text{CaMnO}_3$ and $\text{CaMnO}_3/\text{Ca}_{0.96}\text{Ce}_{0.04}\text{MnO}_3$ bilayers and we observed a topological with a comparable amplitude (Fig. 4.5). The amplitude of the topological Hall effect is reduced in the bilayers compared to the bare $\text{Ca}_{0.96}\text{Ce}_{0.04}\text{MnO}_3$. We ascribe this effect to the increase in carrier density of the bilayers compared to the bare manganite, explained in the next section.

As no plausible scenario with DMI as the main cause of topological charge emerged, we have performed magnetic force microscopy (MFM) measurements to probe the micromagnetic configuration of our samples in relation to the topological Hall effect.

4.2.1 Magnetic force microscopy measurements

The low temperature magnetic force microscopy setup used commercial piezoresistive tips with 100 nm of Co deposited on top. The images were taken by scanning the surface at a constant height of ≈ 60 nm, and the magnetization of the sample

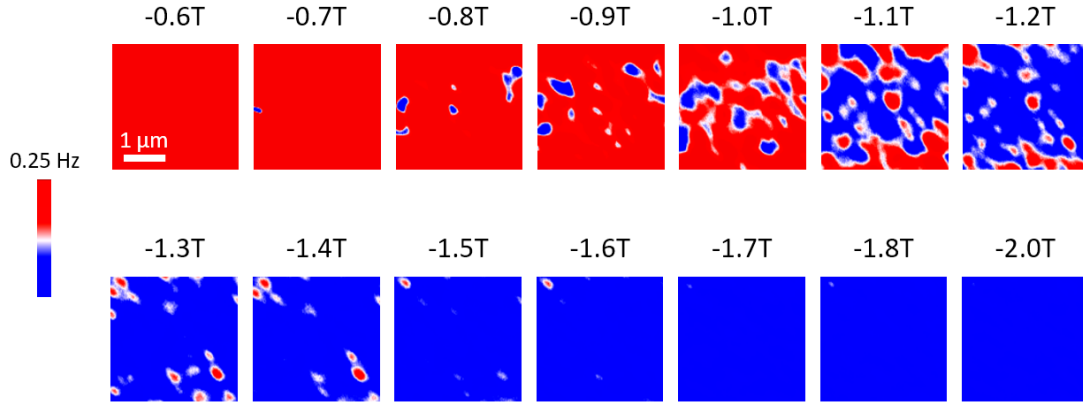


Figure 4.6: Magnetic force microscopy images at 10 K at different negative magnetic fields sweeping downwards after applying a positive perpendicular field of +3T.

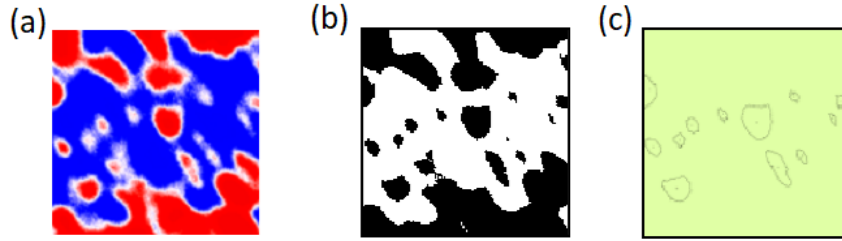


Figure 4.7: (a) Initial $3 \times 3 \mu\text{m}^2$ image. (b) Binarized image by using a threshold around the z scale. (c) Image showing the contours of particles of an automated particle counting program.

was obtained from the change of resonant frequency of the tip, proportional to the out-of-plane stray field gradient [166].

We measured the out-of-plane magnetization as a function of temperature of the same sample. In Fig. 4.8 we show such images, taken after saturating positively the magnetization (by applying +3 T), and then sweeping the field downwards. At -0.6 T the magnetization is still fully aligned in the positive direction (red color). As the manganite thin film nucleates domains with negative magnetization (blue), positively magnetized bubble domains (red) start to appear. At -1.2 T the red bubble domain density peaks, and gradually falls off with increasing field. These bubbles have diameters in the 100 – 300nm range, the same as topological bubbles reported in other centrosymmetric oxides [104, 101, 102, 107]. As these bubbles can carry topological charge, the topological Hall effect they cause would be proportional to their density (as in the Bruno model for a skyrmion array, Eq. 1.5).

We analyzed the images by binarizing the raw images. We set a threshold between the up (red) and down (blue) amplitudes and then processed the binarized images with a particle counting program, as shown in Fig. 4.7. In Fig. 4.8 we show the computed density of bubble domains vs topological Hall effect, at 10 K, 40 K and 80

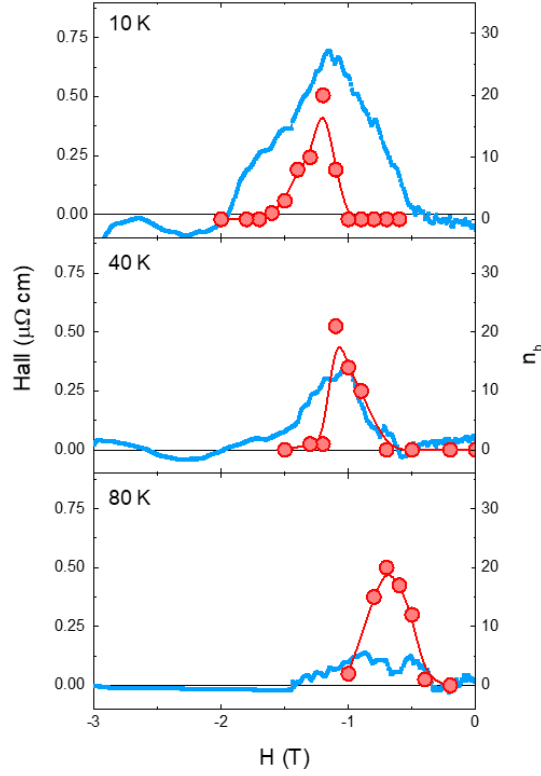


Figure 4.8: Field dependence of the topological Hall resistivity (blue line, left axis) and of the number of observed bubbles in the MFM images (red dots, right axis) at 10 K, 40 K and 80 K.

K. One can see that the density of bubbles varies strongly with field, and peaks at a field close to the topological Hall peak H_T . At different temperatures, the bubble density peaks shifts, closely following H_T . This suggests that the topological Hall effect arises from a specific spin texture associated to these magnetic bubbles.

4.2.1.1 Polarity and topological charge of magnetic bubbles

In the analysis of magnetic force microscopy images and the subsequent bubble counting we have purposely ignored bubble with negative magnetization (blue color). In principle, one should account for the contribution to the topological Hall effect of these blue bubbles as both kinds may carry topological charge. We have seen that, if these bubbles carry any topological charge, and magnetization changes smoothly (as is observed in our measurements), then bubbles with opposite polarities must have opposite vorticity v , and thus the same topological charge Q .

Fig. 4.9 a schematic of bubble nucleation. Blue skyrmion bubbles with a vorticity $v = +1$ are first nucleated (Fig. 4.9a), then expand as the magnetic field increases, reducing the size of the red domains that eventually become red skyrmion bubbles with $v = -1$ (Fig. 4.9c). The opposite would hold if the blue bubbles were nucleated

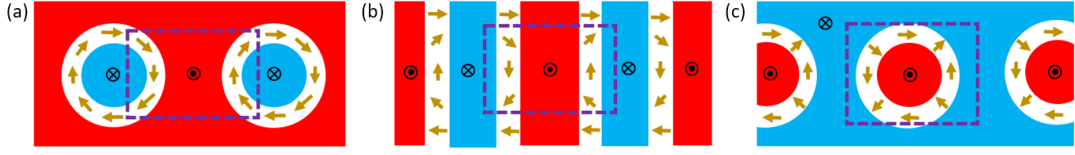


Figure 4.9: Representation of the topology of nucleated skyrmion bubbles. After magnetizing the sample positively (red) and sweeping down the magnetic field, at around -0.9 T the manganite starts nucleating bubbles with a downwards magnetization (blue bubbles) (a). The vorticity is given by energetics and is assumed in this case to be $v = +1$. Increasing the (negative) magnetic field, the skyrmion bubbles expand to the point that they merge with others while the red ones shrink and eventually become red bubbles. During this expansion, the domain walls that define different blue domains join to become the domains walls of the newly formed red bubbles (b), and as the outside of the blue domain walls becomes the inside of the red domain walls, the winding directions of the spins around the red bubbles is reversed compared to the blue ones. Thus these red bubbles have a vorticity $v = -1$ (c).

with $v = -1$, making the red bubbles have $v = +1$. This is because blue bubbles and red bubbles will always have opposite vorticity due to the topologically-charged domain walls that are turned inside-out during the magnetization reversal, reversing the winding direction of the spins. However, it should be noted that when a bubble is initially nucleated, the $v = +1$ case is more favorable energetically than the $v = -1$ as it minimizes the magnetic charge $\rho_{mag} \propto \nabla \cdot \vec{n}$ (where \vec{n} is the direction of the spin) and thus increases the dipole interaction [3].

This means that red bubbles will have opposite core polarity (p) and opposite vorticity (v) compared to the blue bubbles and then have the same topological charge $Q = pv$, giving rise to the same emergent magnetic field, both in amplitude and direction. Thus, these blue bubbles should not cause an opposite topological Hall effect but in principle rather contribute in the same way as the red bubbles. Lastly, the blue bubbles are very few and are present in a small window of magnetic field (Fig. 4.10), so this conclusion does not alter our analysis of the topological Hall effect in CCMO in relation to its micromagnetic structure.

4.2.2 Discussion on the possible origins of the topological Hall effect

The topological Hall effect occurs in the field region where micromagnetic corrugation is largest, strongly suggesting that the magnetic bubbles hold the topological charge giving rise to the topological Hall effect, especially after having ruled out the presence of topologically non-trivial structures created by DMI. One possibility is that the topological Hall effect is created by non-coplanar spin configurations at domain walls, with a mechanism similar to that of the anomalous Hall effect. $(\text{Ca,Ce})\text{MnO}_3$ has a high magnetic anisotropy, making the domain walls rather narrow in the 10 – 80

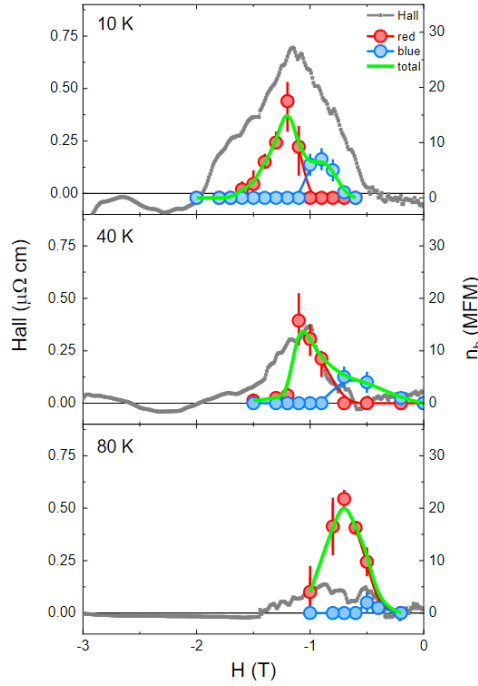


Figure 4.10: Field dependence of the topological Hall resistivity (grey line, left axis) and of the number of observed red and blue bubbles in the MFM images (red and blue dots, right axis) at 10 K, 40 K and 80 K.

nm range. The canting angles would be of the order of $\theta_d = 180 \times a/d_w = 3 - 6^\circ$, where d_w is the domain wall width and a the pseudo-cubic crystal lattice constant. This angle range is comparable to that of the saturated, highly non-coplanar spin ground state, and since the domain walls are a small fraction in volume they would not be able to create an effect with an amplitude as large as that of the anomalous Hall effect itself.

We argue that, while Dzyaloshinskii-Moriya interaction and domain walls cannot explain the topological Hall effect, the magnetic bubbles themselves can. As we have shown in 1.1.1.1, even in the absence of DMI, magnetic bubbles can carry a non-zero topological charge Q , which depends on the energetics of the magnetic structure of the domains walls. Magnetic bubbles that carry non-zero Q are called magnetic skyrmion bubbles as they are topologically equivalent to magnetic skyrmions. Lorenz transmission electron microscopy experiments would be able to sort out specifically which topological charge our magnetic bubbles carry, but unfortunately such experiments are technically prohibitive in oxide thin films, and were successfully reported for the first time only during the last months this PhD [107].

Thus, even though we cannot probe the bubbles' topology directly, these magnetic bubbles can, in principle, contribute to the topological Hall effect through a Berry phase mechanism. However, if we use the Bruno model (Eq. 1.5) with the measured

Material system	THE amplitude ($\mu\Omega \text{ cm}$)	Note	Ref.
MnSi	0.0045	Skyrmion system	[29]
MnP	0.01	Fan spin system	[31]
MnGe	0.16	Skyrmion system	[168]
SrRuO ₃ /SrIO ₃	0.2	Interface system	[111]
Fe _{0.7} Co _{0.3} Si	0.5	Skyrmion system	[169]
EuO	0.6	Centrosymmetric	[105]
Ce _{0.01} Ca _{0.99} MnO ₃	120	Correlated oxide	[167]

Table 4.1: Comparison of topological Hall effect amplitudes in various materials systems

bubbles density at 20 K (assuming each bubble carries a unit of topological charge Q), we obtain a topological Hall effect larger by a factor of 40. This could be because we are not able to measure smaller bubbles, although due to our domain wall width d_w of the order of 10–20 nm, our bubbles would have, in the smallest case, a diameter \approx 30 nm, which means that they would not escape detection. Even if, somehow, smaller bubbles were able to nucleate, they would have to be 40 times more abundant than the measured ones, which would be unrealistic.

If we assume that each of these bubbles carries more than an unit of topological charge Q , their size would not be able to accommodate $Q = 40$, as even the hardest magnetic bubbles cannot carry more than a charge $Q = 7$ every μcm of circumference (due to the size of Bloch lines necessary for multi- Q states). We conclude that, while the magnetic bubbles have been shown to be the most likely cause of the topological Hall effect, the latter’s large magnitude must still be explained.

4.3 Doping dependence and enhancement of the topological and anomalous Hall effect

In Fig. 4.11 we show the Hall effects at 20 K for samples of 1%, 2%, 4%, and 5% Ce-doped 20 nm thin film. The amplitudes of both topological and anomalous Hall effect vary strongly with doping, and diverge as we approach the metal-insulator transition at low dopings. For 1% Ce doping, this is the largest topological Hall effect ever reported, as shown in Table 4.1. In this section we will show the doping and temperature dependence of the two Hall effects, the relationship between topological Hall effect and micromagnetic configuration, and discuss the possible origins of both Hall effects. Unfortunately, a full study in temperature of the Hall effect of 1% Ce-doped samples was not done due to the technical difficulties of measuring the transverse resistivity of such an insulating sample.

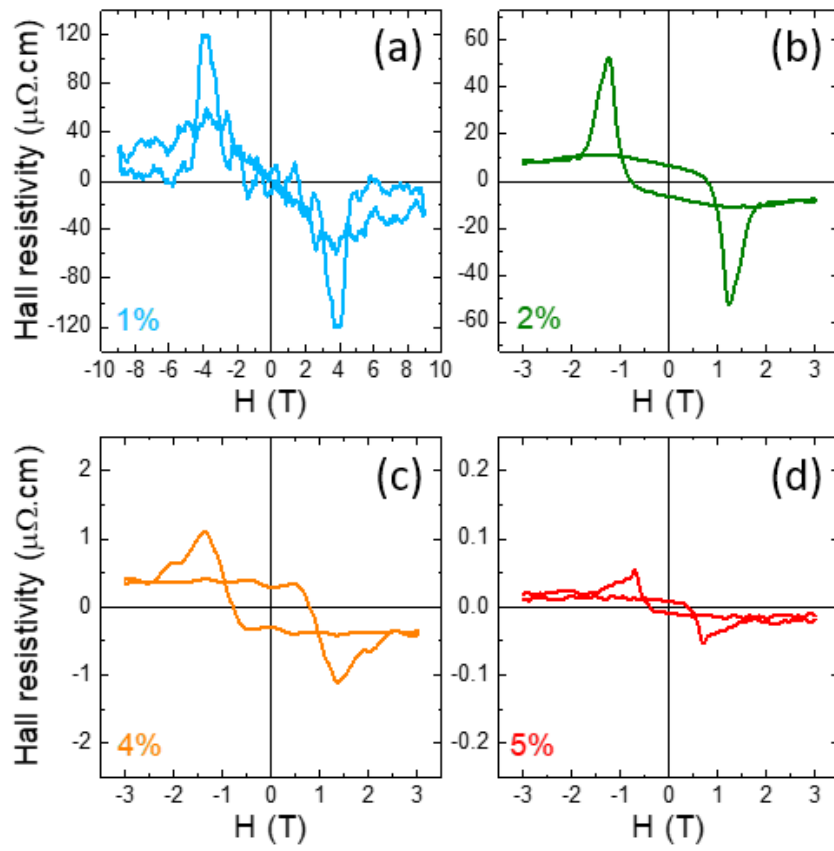


Figure 4.11: Topological and anomalous Hall effect at 20 K for 1% (a) and 15 K for 2% (b), 4% (c) and 5% doping (d).

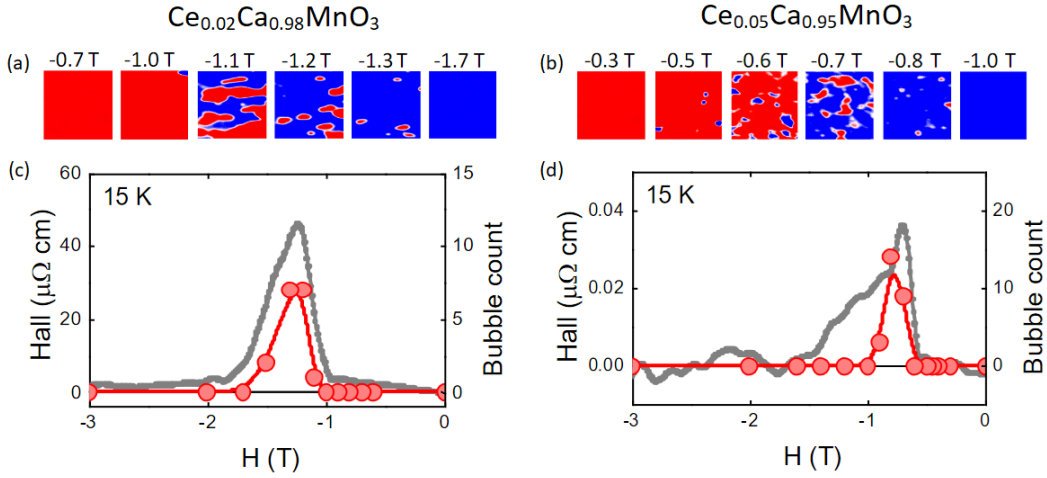


Figure 4.12: Magnetic force microscopy images at 15 K, at different negative magnetic fields, after applying a positive perpendicular field of +3 T for 2% Ce doping (a) and 5% Ce doping (b). Field dependence of the topological Hall resistivity (blue line, left axis) and of the number of observed bubbles in the MFM images (red dots, right axis) at 15 K, for 2% Ce doping (a) and 5% Ce doping (b).

4.3.1 Doping dependence of the micromagnetic structure

We performed magnetic force microscopy measurements on 2% and 5% Ce-doped thin films to probe their micromagnetic structure, which could be in principle related to the strong doping dependence of the topological Hall effect that we observe. Fig. 4.12a,b shows the out-of-plane magnetization of the same 2% and 5% Ce-doped sample whose Hall effect we show in Fig. 4.11. Similarly to what was shown in the previous section for the 4%-doped sample, we magnetized the sample positively with a +3 T field and swept the field downwards. Just as the 4% sample, both the 2% and 5% doped samples feature magnetic bubbles with a magnetic field dependence that tracks the topological Hall effect (Fig. 4.12c,d). Additionally, the maximum bubble density remains roughly constant and its peak follows the topological Hall effect throughout all temperatures. This corroborates our proposed picture of bubbles with a non-trivial topology which gives rise to the topological Hall effect.

The size distribution of the magnetic bubbles does not significantly vary between doping, as seen in Fig. 4.13a. In principle, thin films with different dopings can have magnetic bubbles of different size, owing to different magnetic properties: the magnetic anisotropy and the ferromagnetic stiffness. We extract the anisotropy energy $K = \frac{MH_C}{2}$ from the magnetization M (in Fig. 2.10) and the coercive field H_C (obtained from MOKE for 4%, in Fig. 2.11, and from anomalous Hall effect for 2% and 5%, in Fig. 4.11). The doping dependence of the anisotropy energy K is plotted in Fig. 4.13b. Within error bars, K is roughly constant with doping.

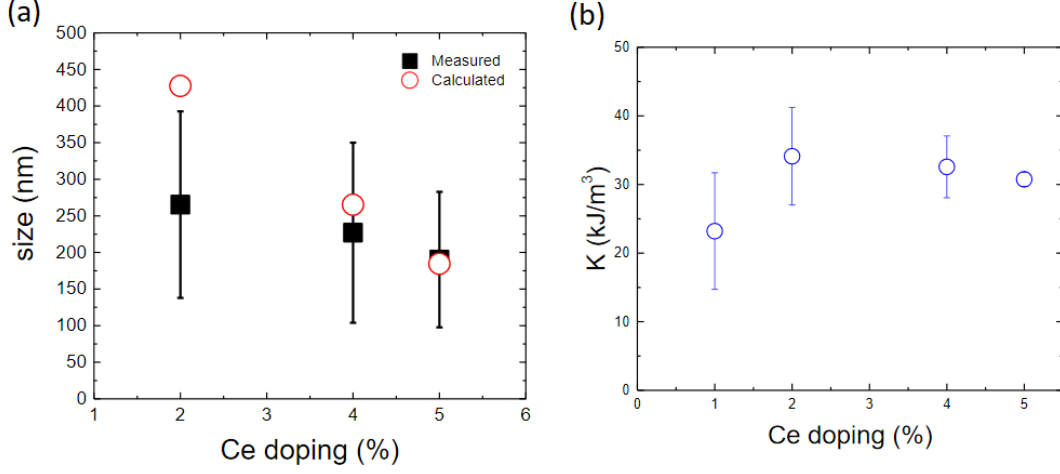


Figure 4.13: (a) Comparison of the experimental and calculated bubble sizes for different Ce dopings. (b) Doping dependence of the anisotropy constant at 20 K.

To obtain the ferromagnetic stiffness A , we first compute the canting angle θ_C assuming

$$\sin \theta_C = \frac{J_{FM}}{J_{AFM}} = \frac{M}{M_{full}}, \quad (4.6)$$

where J_{FM} and J_{AFM} are respectively the ferromagnetic and antiferromagnetic exchange constant, M is the magnetization and $M_{full} = 4 \mu_B/\text{u.c.} = 534 \text{ emu}\cdot\text{cm}^{-3}$ is the magnetization of a hypothetical fully ferromagnetic CaMnO_3 . Since the magnetic transition is driven by antiferromagnetic exchange, we can deduce J_{AFM} from the transition temperature [42, 43]:

$$T_C = \frac{2J_{AFM}zS(S+1)}{2k_B}, \quad (4.7)$$

where z is the number of magnetic sites in the unit cell (here $z = 1$). The ferromagnetic stiffness becomes [42]

$$A = 2J_{AFM} \frac{S^2}{a} \sin \theta_C, \quad (4.8)$$

where a is the lattice constant. Using these values, we calculate the average bubble size [2]:

$$l = 8 \frac{4(AK)^{1/2}}{\mu_0 M^2}. \quad (4.9)$$

The obtained values are in good agreement with the measured sizes (Fig. 4.13a).

Hence, in all three dopings, magnetic bubbles have a similar size distribution, consistently with their magnetic anisotropy. Their maximum density, which remains roughly constant with temperature, also does not strongly depend on doping (varying by a factor 2 between 2% and 5% doping).

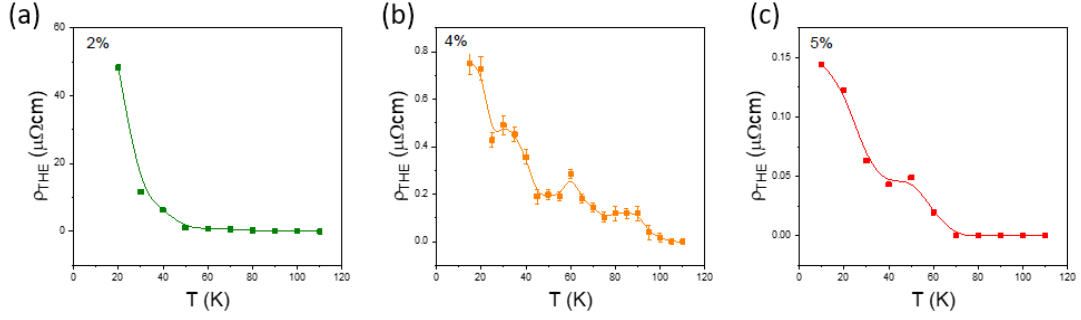


Figure 4.14: Temperature dependence of the topological Hall resistivity for (a) 2% Ce doping, (b) 4% Ce doping, and (c) 5% Ce doping.

4.3.2 Doping and temperature dependence the Hall effect

4.3.2.1 Topological Hall effect

The topological Hall effect (Fig. 4.14) decreases almost monotonically with temperature, disappearing at the critical temperature T_C throughout all dopings. Magnetic force microscopy experiments showed that the magnetic bubbles are follow closely the topological Hall effect with a maximum density that stays roughly constant in temperature. Hence, the change in temperature of the topological Hall effect cannot depend on a variation of the magnetic bubbles themselves. According to the Bruno model, the topological Hall resistivity is proportional to P (Eq. 1.5), which decreases with increasing temperature, consistently with our finding. In manganite thin films, one should expect the spin polarization to be proportional to the square of the magnetization [170], and thus roughly linear: $\rho_{THE} \propto P \propto M^2 \propto \left(1 - \frac{T}{T_C}\right)$. This linearity is present for the 4% and 5% samples (Fig. 4.14a,b), while the anomalous Hall effect of 2% doping (Fig. 4.14c) has a much stronger decrease.

Another shortcoming of the Bruno model is the fact that it cannot fully explain the doping dependence of the topological Hall resistivity. Since the density of the nucleated magnetic bubbles does not change significantly with doping ($\approx 10 - 20 \mu\text{m}^{-2}$), according to Eq. 1.5 the topological Hall effect can only be modified by doping through the carrier density ($\rho_{THE} \propto \frac{1}{n}$). However, comparing the topological Hall effect for 1% and 5% doping (Fig. 4.11) we can see that a fivefold increase in carrier density leads to a decrease by three orders of magnitude of the topological Hall effect.

4.3.2.2 Anomalous Hall effect

Let us now focus on the anomalous Hall effect, which has different trends in temperature for different doping levels. For 2% doping (Fig. 4.15a), the topological Hall effect is monotonically decreasing upon heating. At 4% doping (Fig. 4.15b) we have

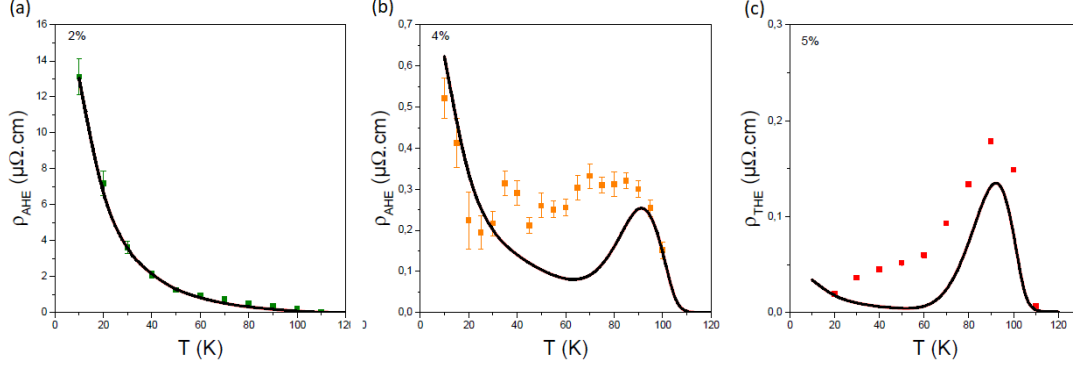


Figure 4.15: Temperature dependence of the topological Hall resistivity for (a) 2% Ce doping, (b) 4% Ce doping, and (c) 5% Ce doping. Temperature dependence of the anomalous Hall resistivity for (d) 2% Ce doping, (e) 4% Ce doping, and (f) 5% Ce doping. The red lines are fits using Eq. 4.10.

a more intermediate situation, with a broad peak close to the transition temperature T_C , but also an increase of the signal at low temperatures. The 5% doped sample (Fig. 4.15c) has a monotonically increasing signal up to 90 K, similarly to other colossal magnetoresistance manganites such as $\text{La}_{0.7}\text{Ca}_{0.3}\text{MnO}_3$ and $\text{La}_{0.7}\text{Sr}_{0.3}\text{MnO}_3$.

In such manganites, the anomalous Hall effect is vanishingly small at low temperatures and appears only at $T_C/2$. Upon heating, it increases, peaking around T_C and tailing off at higher temperatures in the paramagnetic phase (see 1.2.4.3). On the other hand, in $(\text{Ca,Ce})\text{MnO}_3$ the anomalous Hall effect is not only measurable at low temperatures, but it also has its maximum at close to 0 K rather than close to $T_C/2$. $\text{La}_{0.7}\text{Ca}_{0.3}\text{MnO}_3$ and $\text{La}_{0.7}\text{Sr}_{0.3}\text{MnO}_3$ are fully ferromagnetic, and so the spin triads that cause the anomalous Hall effect can be formed only by thermal excitation, thus the effect increases upon heating. In contrast $(\text{Ca,Ce})\text{MnO}_3$, in its ground state, has a highly non-coplanar spin structure featuring non-coplanar spin triads even in the absence of thermal excitations (see Fig. 1.23a).

If one considers the model developed by Calderon and Brey [99] (described in 1.2.4.3), in which the non-coplanar spin triads giving rise to the anomalous Hall effect are seen as skyrmion strings, we can factor in the presence of non-coplanar spin triads present in the 0 K ground state of the system. In the original model, the density of skyrmion strings is given by a simple Boltzmann distribution ($\propto e^{-E_c/k_B T}$), thus giving a vanishingly low anomalous Hall effect at low temperatures. Here, we add a constant to account for a non-zero density of skyrmion strings at zero temperature, and the equation for the resulting emergent magnetic field (Eq. 1.34) can be modified:

$$\langle b \rangle = \frac{\alpha}{6} a \lambda_{so} n S \frac{(\zeta + e^{-E_c/k_B T})}{T} \quad (4.10)$$

where $\alpha = 230$, a is the lattice parameter, λ_{so} is the spin-orbit coupling constant, n is

carrier density, S is the net localized spin, $E_C \approx 8.7k_B T_C$ is the skyrmion string core energy, and ζ is a dimensionless constant accounting for the non-coplanar spin triads at low temperature. This equation can be then plugged in the Bruno model (Eq. 1.5) to obtain the anomalous Hall resistivity. We can use this model to fit the temperature dependence of the anomalous Hall effect for these three doping levels. For this fit we supposed that the spin polarization P of the sample followed the square of the magnetization [170]: $P \propto M^2 \propto \left(1 - \frac{T}{T_C}\right)$. The fits are shown in Fig. 4.15.

The obtained parameters are $\zeta = 4 \times 10^{-5}$ for 2% doping, $\zeta = 1.8 \times 10^{-6}$ for 4% doping, and $\zeta = 1 \times 10^{-7}$. The 5% sample, which is the most ferromagnetic, has an anomalous Hall effect resembles that of $\text{La}_{0.7}\text{Ca}_{0.3}\text{MnO}_3$ and $\text{La}_{0.7}\text{Sr}_{0.3}\text{MnO}_3$ and can be simulated with a small ζ value. In this case, ζ is negligible ($\zeta \ll e^{-E_c/k_B T}$) and the original model from Calderon and Brey is applicable. In contrast, the 2% sample has the weakest magnetization (in other words that shows the stronger deviation from the collinear case), and its anomalous Hall effect decreases with temperature and a large ζ must be used to account for this dependence. In this case ζ dominates over the Boltzmann distribution ($\zeta \gg e^{-E_c/k_B T}$), and so, from Eq. 4.10, $\rho_{AHE} \propto \frac{1}{T}$ and thus the anomalous Hall effect is monotonically decreasing with temperature. The 4% sample corresponds to an intermediate situation where we can see both the increase at low temperature and the broad peak close to T_C .

While the agreement is not perfect, the model captures the main features of the temperature dependence of the anomalous Hall effect, namely a broad maximum close to the transition temperature T_C , and an increase at low temperature. As for the topological Hall effect, this model underestimates the magnitude of the effect as our data is fitted with a prefactor almost two orders of magnitude larger than what is expected from theory [98, 99].

4.3.3 Weak-coupling topological Hall effect

We have show that the conventional Bruno model is not able to explain not only the amplitude of the topological Hall effect that we measure, but also its behavior with different dopings and temperatures. This is because this model is in the strong coupling limit, which is not ideal for a weak ferromagnet such as $(\text{Ca,Ce})\text{MnO}_3$. Additionally, it does not consider non-adiabatic contributions which may, in general, play a role. Nakazawa et al. [171] recently developed a model which can account for both weak and strong coupling, and includes both adiabatic and non adiabatic contributions. The model works in the diffusive limit, i.e. $ql < 1$, where $1/q$ is the length scale of the topological spin texture (in our case the bubble size d_{sk}), and $l = \frac{6\pi^2\hbar}{e^2\rho k_F^2}$ is the electron mean free path. The transport phenomena that arise from topological spin textures depends on the scale of the exchange coupling. We can thus consider three regimes:

- Regime 0: strong coupling: $(ql)^2 < 1 < \tau/2\tau_{ex}$
- Regime 1: weak coupling and local effective field: $(ql)^2 < \tau/2\tau_{ex} < 1$
- Regime 2: weak coupling and non-local effective field: $\tau/2\tau_{ex} < (ql)^2 < 1$

$\tau = \frac{m^*}{e^2\rho n}$ is the momentum relaxation time and $\tau_{ex} = \frac{\hbar}{2J}$. Here $J = J_{sd}S_F$ where J_{sd} is the s-d exchange coupling constant and S_F is the ordered ferromagnetic spin, which causes the exchange splitting of the electron spectrum. Regime 0, where the Bruno model holds, considers only adiabatic processes such as Berry phase mechanisms, but there are other non-adiabatic effects that can occur in regimes 1 and 2.

To understand which regime to consider for CaMnO₃, we have to evaluate $(ql)^2$ and $\tau/2\tau_{ex}$; let us start with the latter. To estimate the exchange coupling constant, we note that the localized atomic spin is formed by the t_{2g} spins with $S = \frac{3}{2}$ so Hund coupling is going to take the place of s-d coupling. Thus $J_{sd} = J_H \approx 1$ eV. The exchange splitting in (Ca,Ce)MnO₃ is caused by the net ferromagnetic moment caused by canting S_F , and not the antiferromagnetic moment S_{AF} . This stems from the fact that there would be no topological Hall effect with no canting ($S_F = 0$), so the relevant moment behind exchange splitting is the net ferromagnetic moment. Therefore $J = J_H S_F = J_H S \sin \theta_C \approx 0.2$ eV, with $\theta_C = 8.5^\circ$ the canting angle for 4% doping. Thus $2\tau_{ex} = \frac{\hbar}{J} \approx 1.6$ fs. In our 4% doped sample $\rho = 4 - 8$ mΩcm, giving $\tau = \frac{m^*}{e^2\rho n} \approx 1.3 - 2.6$ fs, and so $\frac{\tau}{2\tau_{ex}} = 0.8 - 1.6$. So, the 4% doped sample sits right at the border between regime 0 and regime 1/2, defined by $\tau/2\tau_{ex} = 1$. Lower doping samples, on the other hand, have smaller J (because of the lesser canting) and thus larger τ_{ex} , and larger ρ and thus smaller τ . This means that the ratio $\tau/2\tau_{ex}$ decreases with decreasing doping, and so below the 4% Ce doping level we are well into the weak coupling regime (1 and 2).

To distinguish between the latter two regimes one has to take into account $(ql)^2$. In our 4% doped sample, from the previous chapter, we have $k_F \approx 1.5$ nm⁻¹, giving $l = \frac{6\pi^2\hbar}{e^2\rho k_F^2} = 1 - 2$ nm. The average bubbles size is $q^{-1} = 200$ nm, and therefore $(ql)^2 = 10^{-4}$. Thus we are well into the diffusive regime (defined by $(ql) < 1$), and $(ql)^2 \ll \tau/2\tau_{ex}$, meaning that effective field is local and we are in regime 1.

So far we have not taken the spin relaxation of the conduction electrons into account. If we do, we obtain two other regimes:

- Regime 1': strong spin relaxation, local effective field: $\tau_s/2\tau_{ex} < 1, ql_s < 1$
- Regime 2': strong spin relaxation, non-local effective field: $\tau_s/2\tau_{ex} < 1, ql_s > 1$

τ_s is the spin relaxation time and $l_s = \sqrt{D\tau_s}$ the spin diffusion length, with $D = \frac{1}{3}v_F^2\tau$ the diffusive constant. The complete phase diagram, with the five regimes, is in Fig. 4.16. Since τ_s is typically larger than $2\tau_{ex}$ by at least a factor 3, we are in regime 1, and not 1'/2'.

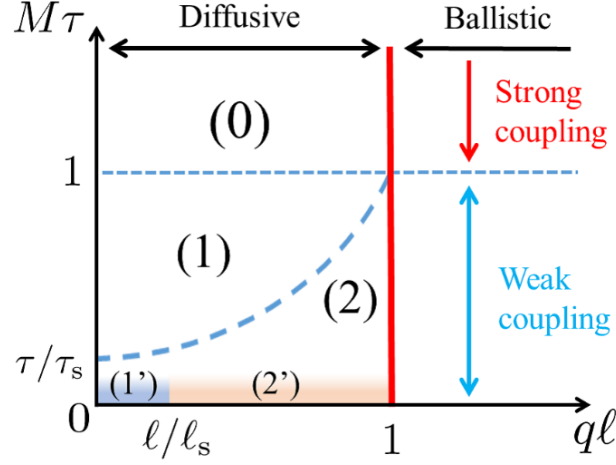


Figure 4.16: Phase diagram of the various diffusive regimes as a function of $M\tau = \tau/2\tau_{ex}$ and ql . [171]

In regime 1 the Hall resistivity is [171]

$$\rho_H = \frac{2 \langle b \rangle J}{3 en E_F}. \quad (4.11)$$

From

$$\frac{\langle b \rangle}{e} = \frac{h}{e^2} \sigma_{sk} = R_0 \sigma_{sk} \quad (4.12)$$

with $\langle b \rangle$ the emergent magnetic field from the topological charge, σ_{sk} the skyrmion density, and $R_0 = 25.8 \text{ k}\Omega$, we get

$$\rho_H = \frac{2R_0 \sigma_{sk} J}{3 n E_F} = \frac{4}{3(3\pi^2)^{2/3}} \frac{R_0 \sigma_{sk} J m^*}{\hbar^2 n^{5/3}}. \quad (4.13)$$

Unlike the strong coupling model from Bruno (Eq. 1.5), this expression has a stronger direct dependence on doping ($n^{5/3}$ versus n), and also depends on the effective mass of the carriers.

4.3.4 Discussion on possible mechanisms of mass enhancement

(Ca,Ce)MnO₃ shows both strong electron-phonon interaction and strong correlations. Both of these mechanisms, as we have shown in 1.2.3.2, are able to modify the effective mass of the carriers, and we have to be able to discriminate between the two. In the previous chapter, we have shown that (Ca,Ce)MnO₃ features two kinds of carriers: one, the quasi-2D electrons, feature a strong electron-phonon coupling that transforms them into polarons and enhances their mass; the other, the 3D electrons, are not subject to the same strength of electron-phonon coupling. The quasi-2D electrons, dragging phonons as they travel, have a higher mass compared to that of the

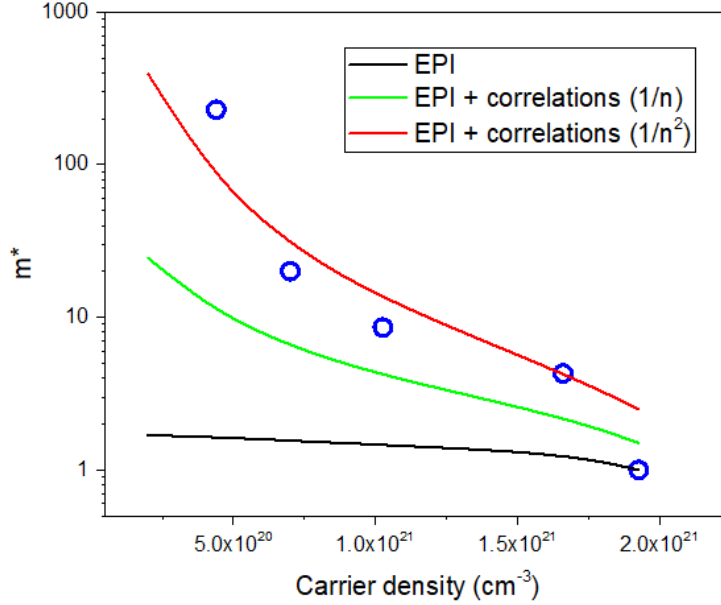


Figure 4.17: Extracted effective mass at low temperature, normalized by the value at 5% Ce doping, and assuming $m = \rho/ne^2\tau$ and no doping dependence of τ [174], with simulations of the effective mass with electron-phonon coupling (black line), and additional weak (green line) and strong correlations (red line).

3D electrons. However, the quasi-2D electrons are much higher in number and we have shown that they dominate longitudinal and transverse electron transport (Fig. 3.10).

Let us first focus on the dominant quasi-2D electrons and their electron-phonon coupling-driven mass enhancement. Since we do not see dispersions in the ARPES measurements, we are not able to measure the effective mass of these carriers directly, and we have to estimate them using the appropriate theory. The spectral function (Fig. 3.9) of these quasi-2D polarons strongly suggests that the coupled phonons are long range. In this regime, the Fröhlich model is valid and to estimate the effective mass one have to obtain the $\alpha = \frac{e^2}{4\pi\epsilon_0\kappa\hbar} \sqrt{\frac{m}{2\hbar\omega_0}}$ parameter (Eq. 1.23). DFT calculations estimate the unenhanced mass of the quasi-2D polarons to be $m = 0.66m_e$. The phonons that effectively modify the effective mass are the most infrared-active modes; DFT shows that these infrared-active modes have an energy of $\hbar\omega_0 = 30$ meV. In $(\text{Ca,Ce})\text{MnO}_3$ the high-frequency dielectric constant can be estimated from the optical index: $\epsilon_\infty \approx n_{opt}^2 \approx 5$ [123, 172]. This value is similar to that of most manganites and does not change with the doping level. To compute $\frac{1}{\kappa} = \frac{1}{\epsilon_s} - \frac{1}{\epsilon_\infty}$ we need the static and high frequency dielectric constants ϵ_s and ϵ_∞ . The static dielectric constant is $\epsilon_s = 55$ for pure CaMnO_3 [173], while for the 4% doped $\epsilon_s = 20$ [131]. For these estimates, we assume that ϵ_s varies linearly with doping between 0% and 5%. Thus, the α parameter varies with doping only due to the static dielectric constant ϵ_s , through the parameter

κ . With these parameters, we obtain $\alpha = 3.8$ for 0% Ce doping and $\alpha = 2.3$ for 5% doping. This means that we are in the weak electron-phonon coupling regime ($\alpha < 4$). Here, the mass enhancement is (see 1.2.3.1)

$$\frac{m^*}{m} = \frac{1}{1 - \alpha/6}. \quad (4.14)$$

In Fig. 4.17 we show the electron-phonon interaction-induced mass enhancement compared to experimental estimates. The measured effective mass shows a strong enhancement as the doping, and thus the carrier density, decreases as we get close to the metal-insulator transition at low doping. While the effective mass increases by 3 orders of magnitude between 5% doping and 1% doping, the electron-phonon interaction can only account for a change of a factor ≈ 2 .

One could argue that while the spectral function of these quasi-2D polarons strongly suggests that the coupled phonons are long-range, there still might be short-range electron-phonon interaction present and thus the effective mass enhancement could be better described with the Holstein model. In this case the mass enhancement is expected to be $m^*/m = (1 + \lambda)$, with $\lambda = E_p/D$ (see 1.2.3.1). Here, the mass enhancement would vary with doping since energy $E_p \approx \frac{q_D e^2}{\pi \kappa}$ depends on κ , which varies with doping. Thus, in the Holstein case the mass is approximately proportional to $1/\kappa$ and would have a doping dependence similar to that of the Fröhlich case, and both would have a dependence with doping much weaker than what is measured experimentally.

We conclude that, while the electron-phonon coupling may contribute to the effective mass enhancement, it cannot explain its large amplitude, particularly at low dopings. Ce-doped CaMnO_3 features strong correlations that enlarge the effective mass, diverging close to the Mott transition at low doping. This has been reported for Sr-doped LaTiO_3 and Ce-doped SrMnO_3 (very similar to Ce-doped CaMnO_3), where the effective mass is enhanced by 1-2 orders of magnitude as the doping level approaches the metal-insulator transition. This divergence follows $m^* \propto 1/n^\alpha$, where α has been reported between 1 and 2 (typically is $\alpha = 1$). The dimensionality of the system can come into play, as α reaches 2 at low thin film thicknesses. In Fig. 4.17 we also show the combined mass enhancement from electron-phonon interaction and correlations, both with $\alpha = 1$ and $\alpha = 2$. By including correlations the doping dependence becomes much sharper, particularly for the case of $\alpha = 2$, which is able to replicate well the measured effective masses.

These estimates neglect the existence of the minority 3D charge carriers, however in the previous chapter we have shown that the majority quasi-2D polarons dominate transport (Fig. 3.10) already at 4% doping, and the percentage of 3D carriers decreases with decreasing doping (reaching 3% of the total carriers at 2% doping). Moreover, while mass enhancement through electron-phonon interaction only appears in one of

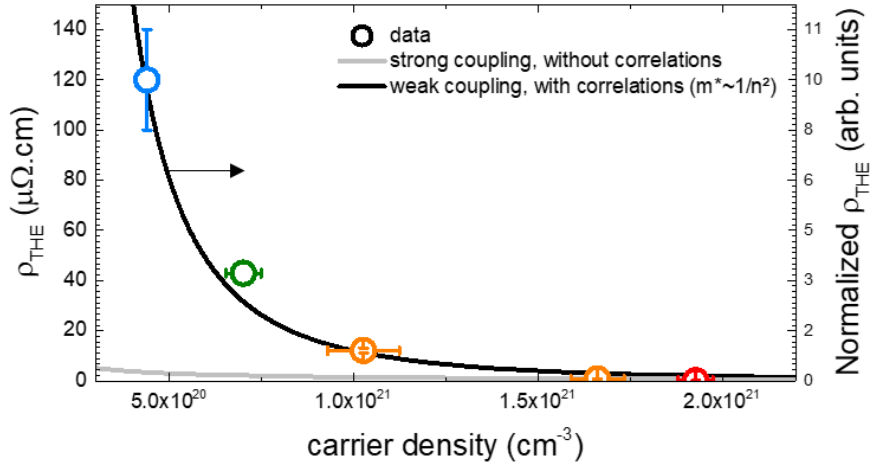


Figure 4.18: Relationship of the topological Hall effect with the carrier density. The model is shown normalized to the experimental value at $1.03 \times 10^{21} \text{ cm}^{-3}$.

the two bands, mass enhancement through correlations is expected to occur for both types of carriers in the same way. This means that we can use a simple $m \propto 1/n^2$ global behavior for mass enhancement in Ce-doped CaMnO_3 .

4.3.5 Enhancement of topological and anomalous Hall effect

If we then include the $1/n^2$ scaling of the effective mass due to correlations, from Eq. 4.13 we obtain

$$\rho_H \propto \frac{1}{n^{2/3+\alpha}} \quad (4.15)$$

since $J = J_H S_F$, so in other words J is proportional to the magnetization, which scales linearly with doping (see 2.4). In Fig. 4.18 we show the amplitude of the topological Hall effect for samples of varying doping, at 20 K, compared to the scaling laws of the strong coupling regime ($1/n$) and weak coupling regime ($1/n^{2/3+\alpha}$). We can see that the strong coupling regime fails to capture the strong amplification of the effect close to the Mott transition. On the other hand, the weak coupling regime with a $\alpha = 2$ mass enhancement reproduces very well the trend of the topological Hall effect. The numerical prefactor is slightly underestimated by this model compared to the data (by a factor of 3). This could be because of non-adiabatic processes such as vertex corrections, effects beyond the single-particle mass renormalization also coming from correlations, that would further increase the Hall signal.

The anomalous Hall effect has also a magnitude that cannot be explained by the adiabatic Bruno model: at 4% doping it is more than one order of magnitude large than what one could expect, and at 2% it is almost three order of magnitude large. Since the anomalous Hall effect stems from the same Berry phase mechanisms as the topological Hall effect, one would expect the former to be strongly enhanced by the

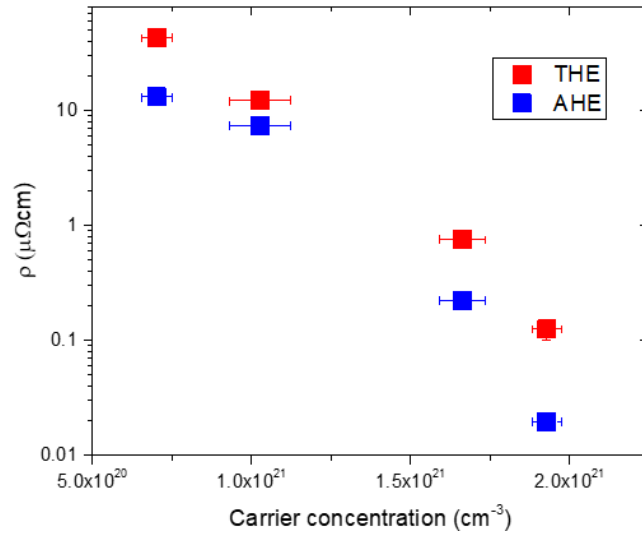


Figure 4.19: Topological and anomalous Hall effect at 20 K.

weak coupling regime as well. Fig. 4.19 shows that the anomalous and topological Hall effect have a very similar trend with doping. Although further studies need to be carried out in order to understand how the anomalous Hall effect behaves in strongly non-collinear ground state system, this shows that the anomalous Hall effect can be enhanced by weak coupling as well.

Chapter 5

Ferroelectric field effect in BiFeO₃/(Ca,Ce)MnO₃ bilayers

At the start of this PhD our main focus was to grow BiFeO₃/(Ca,Ce)MnO₃ bilayers to investigate the effects of the ferroelectric polarization effects on the electronic and magnetic properties of doped CaMnO₃, expanding the work done in our group using undoped CaMnO₃ as the electrode [130]. BiFeO₃/CaMnO₃ bilayers featured a large modulation of the resistivity of CaMnO₃ by the ferroelectric polarization of BiFeO₃. BiFeO₃/(Ca,Ce)MnO₃ bilayers are technologically attractive since, when the Ce concentration is close to that of a phase transition, a change in polarization of the BiFeO₃ layer could drive a phase transition, yielding switchable resistive and magnetic properties.

5.1 Ferroelectric field effect

We grew BiFeO₃/(Ca,Ce)MnO₃ bilayers on YAlO₃ (001) substrates by pulsed laser deposition, as described in 2.1. We first deposited the layer of Ce-doped CaMnO₃. Successively, instead of annealing the film in oxygen, we deposited the BiFeO₃ layer with a substrate temperature $T_{sub} = 450^\circ\text{C}$, oxygen pressure $P_{O_2} = 6 \times 10^{-3}$ mbar, and a substrate-target distance of 44 mm. The laser pulses had a frequency $f = 1$ Hz and a fluence of 0.42 J/cm². Post-growth annealing was then performed by increasing the oxygen pressure to $P_{O_2} = 300$ mbar for 30 minutes, keeping the same heater power.

Fig. 5.1a shows the topography of a typical BiFeO₃ (30 nm)/(Ca,Ce)MnO₃ (20 nm) bilayer grown on YAlO₃. The BiFeO₃ clearly does not grow layer-by-layer, but rather by islands with widths of 100 – 200 nm. The X-ray diffraction $2\theta - \omega$ scan of the same sample, in Fig. 5.1b, shows that the BiFeO₃ is in the highly strained super-tetragonal phase [175]. Additionally, Laue fringes of both the BiFeO₃ and CaMnO₃ peaks are visible, attesting the coherent growth of both films. By altering the growth

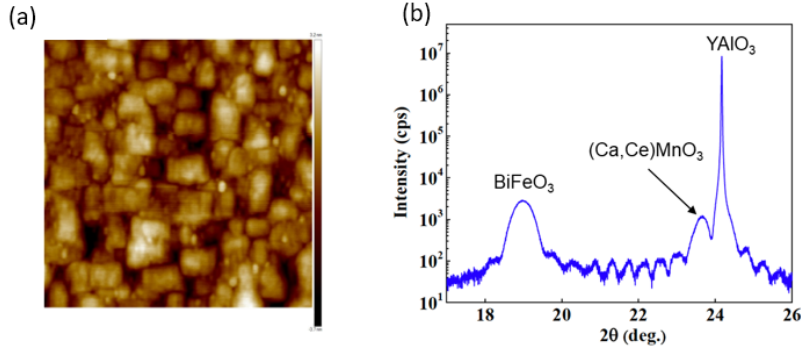


Figure 5.1: Topography (a) and $2\theta - \omega$ scan of an as-grown $\text{BiFeO}_3/\text{Ca}_{0.96}\text{Ce}_{0.04}\text{MnO}_3$ bilayer on YAlO_3 .

conditions of BiFeO_3 in order to obtain smoother BiFeO_3 surfaces (for example by increasing the laser fluence or decreasing the substrate temperature) we consistently saw a reduction of the out-of-plane (pseudo-cubic) lattice parameter c of BiFeO_3 from that of the super-tetragonal phase ($c = 4.6 \text{ \AA}$) to that of the rhombohedral phase ($c = 3.97 \text{ \AA}$), signifying a reduction of the epitaxial quality of the BiFeO_3 layer. On one hand, we can conclude that the island-like growth is caused by the high compressive strain (-6.6%) induced by the YAlO_3 substrates, but also that epitaxial growth can be achieved despite the lack of proper 2D growth shown by the topography.

We performed piezoresponse force microscopy to image and manipulate the polarization of the BiFeO_3 layer, a technique which uses the piezoelectric properties of ferroelectrics (which are also piezoelectrics by symmetry). Piezoresponse force microscopy uses a standard atomic force microscopy setup, while applying an alternating voltage between the cantilever tip and the sample. Due to the converse piezoelectric effect, the applied voltage excites a deformation which is then picked up by the cantilever tip. When the polarization is parallel to the applied electric field, the measured deformation is in phase with the applied field, while when the polarization is antiparallel to the applied electric field the deformation is in anti-phase (Fig. 5.2).

A hysteretic piezoresponce double loop of a $\text{BiFeO}_3/(\text{Ca,Ce})\text{MnO}_3$ bilayer is shown in Fig. 5.3a, showing good switchability of the polarization. $\text{BiFeO}_3/(\text{Ca,Ce})\text{MnO}_3$ bilayers were patterned into Hall bars with the techniques outlined in 2.5. The topography of these devices is shown in Fig. 5.3b. A piezoresponse force microscopy image of a $\text{BiFeO}_3/(\text{Ca,Ce})\text{MnO}_3$ Hall device in its virgin state is shown in Fig. 5.3c. Its polarization is entirely downwards, as expected [131]. We reversed the polarization by applying a voltage bias $V_{DC} = +7 \text{ V}$ (three times the coercive field shown in Fig. 5.3a) to the bottom $(\text{Ca,Ce})\text{MnO}_3$ electrode and scanning the desired area. The polarization after this process is in Fig. 5.3d, which shows a uniformly upward polarization.

We measured the resistivity of the Ce-doped CaMnO_3 film thin as a function

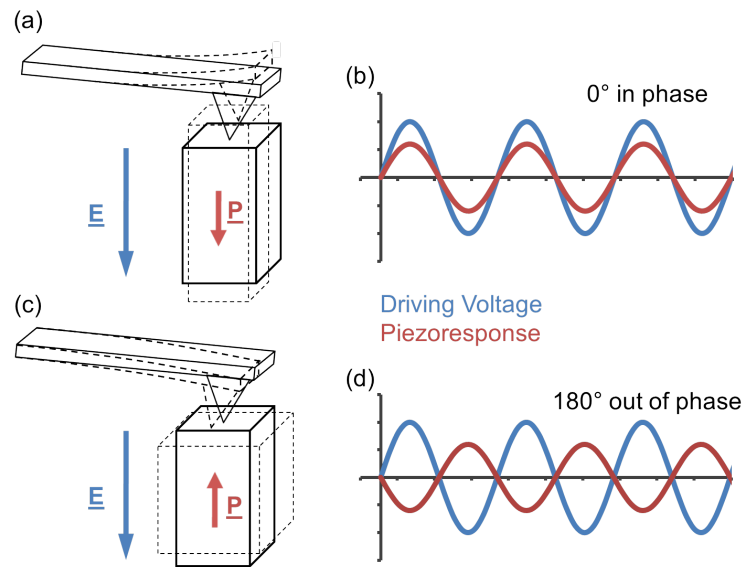


Figure 5.2: Schematic of the operation of a piezoresponse force microscopy. When the polarization is parallel to the electric field due to the voltage bias between the tip and the sample, the deflection is in phase with the applied AC voltage. When the polarization is anti-parallel to the electric field, the deflection is in anti-phase with the applied voltage.

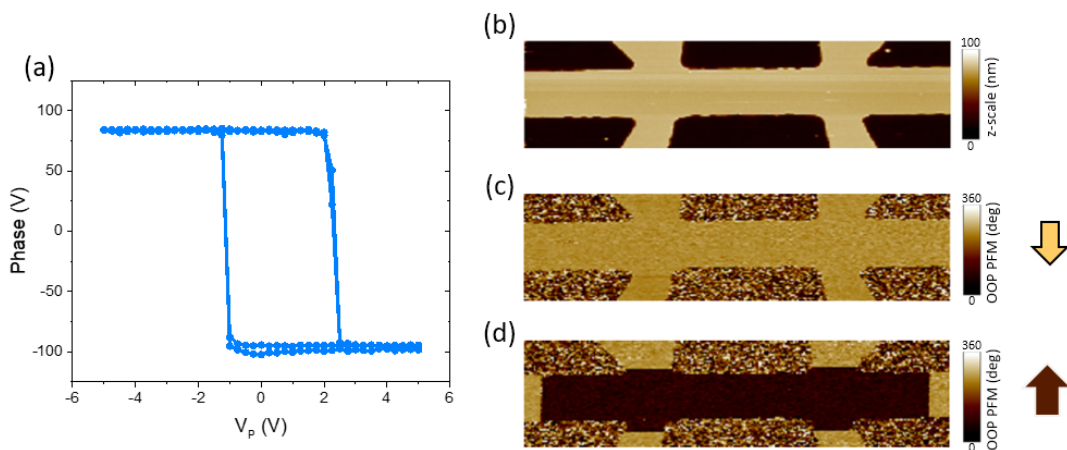


Figure 5.3: (a) Piezoresponce force microscopy phase loop of a $\text{BiFeO}_3/\text{Ca}_{0.98}\text{Ce}_{0.02}\text{MnO}_3$ bilayer. Topography (c) and ferroelectric polarization before (d) and after (e) ferroelectric switching of a $\text{BiFeO}_3/(\text{Ca,Ce})\text{MnO}_3$ Hall bar fabricated by optical lithography.

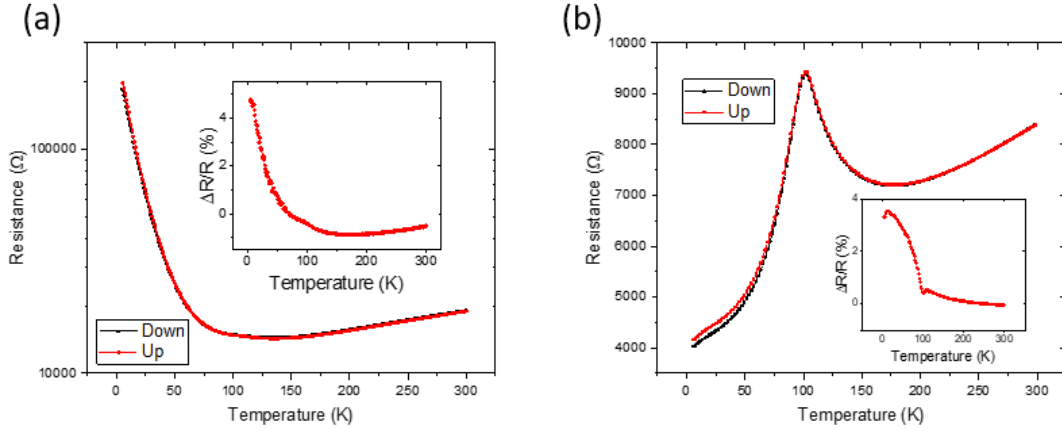


Figure 5.4: Temperature dependence of the resistivity of (a) BiFeO_3 (30 nm)/ $\text{Ca}_{0.98}\text{Ce}_{0.02}\text{MnO}_3$ (10 nm) and (b) BiFeO_3 (30 nm)/ $\text{Ca}_{0.95}\text{Ce}_{0.05}\text{MnO}_3$ (10 nm) on YAlO_3 for the virgin (black) and switched (red) states.

of BiFeO_3 polarization. Fig. 5.4 shows the temperature dependence of BiFeO_3 (30 nm)/ $(\text{Ca,Ce})\text{MnO}_3$ (10 nm) bilayers films with 2% and 5% doping, in the virgin down, and switched up polarizations. The temperature dependence of the virgin resistivity closely resembles that of the bare, doped CaMnO_3 thin films Fig. 3.1. The resistivity measured after switching the polarization upwards has a very similar value compared to that of the virgin state, with only a decrease of 4% at low temperature for both 2% and 5% doping. As the temperature increases, the resistance change decreases, and close to the transition temperature $T_C = 110$ K it changes sign. This effect is due to the non-monotonic change of resistivity with doping: at temperatures higher than the transition temperature $T_C = 110$ K, an increase in doping can correspond to a increase in resistivity while at lower temperatures the resistivity decreases with increasing doping. Regardless, the resistance change due to the ferroelectric field effect is of magnitudes much smaller than what measured with undoped CaMnO_3 electrodes [130].

Modifying the thickness of BiFeO_3 films (10 and 80 nm) did not significantly change the transport results compared to those in Fig. 5.4. Using higher voltages to switch the polarization was also unsuccessful using voltage biases V_{DC} up to 10 V, as biases any higher damage the devices.

Surprisingly, similar devices with undoped CaMnO_3 as electrode instead feature an order-of-magnitude change of resistivity by switching the polarization of the BiFeO_3 top layer [131]. To investigate the lack of measurable effects upon switching the polarization, we turned to transmission electron microscopy to study the polarization switching of BiFeO_3 and electron properties of the manganite electrode on the atomic scale.



Figure 5.5: (a) Schematic of the lamella used for the STEM experiments. $20 \times 20 \mu\text{m}^2$ images of (b) the topography and (c) the ferroelectric polarization of the bilayer with deposited metal markers before focused ion beam lithography.

5.2 Atomic scale analysis of polarization switching

We prepared $\text{BiFeO}_3/(\text{Ca,Ce})\text{MnO}_3$ bilayers on YAlO_3 (001) to be analyzed by transmission electron microscopy. After growing the bilayers by PLD, we defined micron size metallic markers by laser lithography, in between which the polarization was switched in micron size rectangles by applying a DC voltage while scanning the conductive tip of the piezoresponse force microscope. The topography and piezoresponse force microscopy phase images of these devices are shown in Fig. 5.5. Cross section lamellas were then prepared by focused ion beam perpendicular to the metallic markers, to study the electronic and structural properties of these bilayers with scanning transmission electron microscopy (STEM).

In STEM, an electron beam is focused to a fine spot on the sample, which is then scanned while capturing the scattered electrons. High-angle annular dark-field imaging (HAADF) is a STEM technique where electrons scattered incoherently at high-angles are captured by an annular detector. The contrast obtained by an ion with atomic number Z is Z^2 . Thus, atoms with a higher atomic number appear brighter, making this technique more suitable to identifying heavier ions. Annular bright field (ABF) complements this technique. ABF detectors are placed in the beam path, collecting electrons that have not scattered. Here the contrast is Z^{-2} , making this technique useful for identifying lighter ions. By combining the two techniques one can obtain the chemical-sensitive structure of multi-element materials such as manganites.

HAADF images of a BiFeO_3 (30 nm)/ $\text{Ca}_{0.96}\text{Ce}_{0.04}\text{MnO}_3$ (20 nm) sample grown on YAlO_3 (Fig. 5.6a) show a highly epitaxial structure with well defined interfaces, and the reciprocal pattern by fast Fourier transform confirms that the BiFeO_3 is in its super-tetragonal state ($c/a = 1.23$). The atomic structure of BiFeO_3 , for both polarizations, is shown in Fig. 5.6b,c. HAADF and ABF images can be combined with RGB colors to observe the position of Bi, Fe and O ions, which indicate large and opposite displacements of Fe and O ions with respect to the Bi for the two polarizations. This both shows that the electric field switching by piezoresponse force microscopy is able to switch the polarization of the BiFeO_3 , and that the polarization is preserved during the sample preparation.

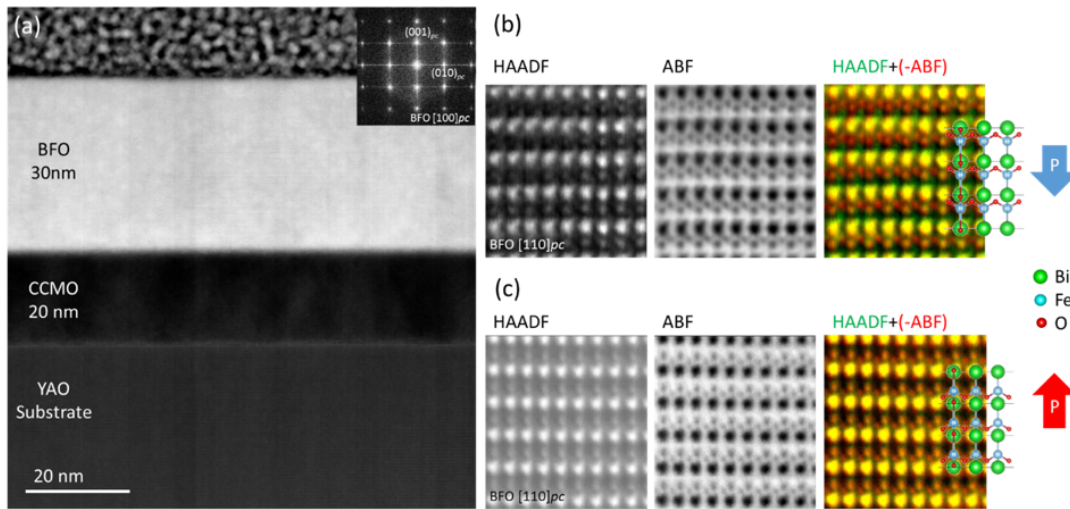


Figure 5.6: a) STEM-HAADF image of a $\text{BiFeO}_3/(\text{Ca,Ce})\text{MnO}_3$ heterostructure grown on YAlO_3 substrate, at the $[100]_{pc}$ zone axis. Insert is the fast Fourier transform of the BiFeO_3 thin film indicating a super-tetragonal structure. STEM-HAADF, ABF and the RGB mixture of the corresponding HAADF and ABF image for (b) downward and (c) upward polarization states, respectively, observed at $[110]_{pc}$ zone axis. The atomic models of different polarizations are overlapped with the corresponding RGB images.

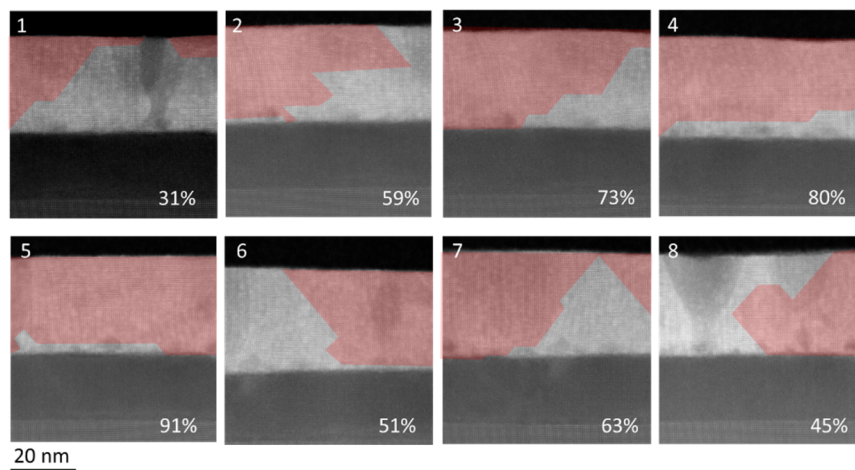


Figure 5.7: STEM-HAADF overview of the BiFeO_3 upward polarization region defined by piezoresponse force microscopy, the upward domains are marked with red shadow and their volume percentage in each image is written at the bottom right.

We analyzed the statistics of the ferroelectric switching by taking eight 64×64 nm² images over an area 700 nm wide in a region polarized upwards (Fig. 5.7). We determine the polarization on the atomic scale by the off-center displacement of the Fe cations. Surprisingly, the switching of polarization is incomplete, with 31% to 91% of the volume population with upward polarization (62% in average). The upward domains seem to be nucleated at the top surface of the BiFeO₃ layer, propagating downwards. As the domains reach towards the BiFeO₃/(Ca,Ce)MnO₃ interface, they are not able to reach the interface and switch its polarization, which is successfully switched only in 19% of the measured area. This explains the low resistance variation by ferroelectric field effect measured in these heterostructures, as only the 19%-switched interface polarization is active in the ferroelectric gating. Such a low percentage of interface switching is lower than the percolation threshold of most 2D models and is not expected to significantly influence the conductivity of the manganite electrode. We performed the same experiments with 10 nm thin BiFeO₃ layers, and by switching the polarization with higher voltages, but we obtained similar results in both cases.

The difference between the large switched volume in bulk and the small switched areas in the interface suggests the existence of an interfacial energy barrier limiting the switching dynamics. This may be caused by the intrinsic electric field at polar interfaces [176]. In BiFeO₃/CaMnO₃ interfaces, it has been shown that BiFeO₃ is B-site (i.e. FeO₂) terminated, due to the A-site (i.e. CaO) termination of CaMnO₃, which is in turn determined by the termination of the YAlO₃ substrate. Thus the interface is a (BiO)⁺¹-(FeO₂)⁻¹-(CaO)⁰-(MnO₂)⁰ sequence [131], which is inherently polar. This polar interface favors a downward polarization, explaining why BiFeO₃ has a virgin polarization pointing downwards after growth by PLD. This polar interface may be the cause of the limited switching at the interface.

This polarization pinning may even play a role in the previously reported switching dynamics of BiFeO₃/CaMnO₃. These bilayers had sizable resistance changes induced by the polarization switching, although with a variation of the sheet carrier density one order of magnitude smaller than the nominal value expected from the polarization of BiFeO₃ [131], similar to values reported in Pb(Zr,Ti)O₃/SrTiO₃ bilayers [132, 133]. This is consistent with our reported 19% of interfacial polarization switching, and points towards interface pinning as a major obstacle in realizing ferroelectrically-controlled Mott transistors.

5.3 Polarization-induced changes in electronic properties of $(\text{Ca,Ce})\text{MnO}_3$ at the atomic scale

Our study of the switching dynamics of BiFeO_3 revealed that the lack of measurable changes in the properties of $(\text{Ca,Ce})\text{MnO}_3$ induced by the polarization switching is due to the low fraction of switched interface polarization. Nonetheless, similar devices with undoped CaMnO_3 electrodes reported resistivity switching. To investigate this, we investigated the electronic properties in the manganite electrode on the atomic scale, by electron energy loss microscopy (EELS). The previously used HAADF and ABF techniques both rely on elastic scattering mechanisms. However, inelastic scattering is also present, as the ions in the sample inelastically scatter the focused electron. In electron energy loss spectroscopy (EELS), the energy lost by the electron beam is measured by an electron spectrometer and interpreted in terms of what caused the energy loss. EELS can hence be used to spectroscopically map the sample.

We used EELS to investigate the electrostatic carrier modulation in the doped CaMnO_3 by the ferroelectric gating. Two typical defect-free interfaces with an atomically sharp termination and opposite interfacial polarization are displayed in Fig. 5.8a-d. Through EELS, we mapped the chemical shift of the Mn-L₃ edge across the doped CaMnO_3 layer (Fig. 5.8e) from the nominal value. We identify three areas (1 to 3 in Fig. 5.8e) that are modulated differently by the polarization switch, and studied their change in electronic structure by their O-K and Mn-L_{2,3} spectra, shown in Fig. 5.8f,g. The O-K pre-edge (in Fig. 5.8f) represents the hybridization between O-2p and Mn-3d electrons. At position 1, near the interface, the pre-edge is shifted to a higher energy compared to positions 2 and 3 due to a change in hybridization, possibly due to oxygen octahedra distortions caused by the epitaxial strain. In all three positions, the O-K pre-edge is not modulated by the polarization orientation, indicating that the carrier modulation is not related to the O ion but rather the Mn cation, consistently with our findings in chapter 3. The Mn-L_{2,3} edges are shown in Fig. 5.8g. The effect of the polarization switch is a shift of the Mn-L₃ edge, and hence the chemical shift of this edge can be used to quantify the electron density in the manganite layer.

We thus extracted the electron density throughout the whole manganite layer from the Mn-L₃ edge shift (Fig. 5.9a), as explained by Marinova et al. [131]. Near the YAlO_3 interface, a large electron accumulation region of 5-6 e^- , 20 (pseudo-cubic) unit cells long, which does not depend on polarization, is attributed to the dead layer measured in transport. Above this dead layer, there is a 30 unit cell-long, bulk-like region (from the 10th to the 40th unit cell, represented by the position 3 in Fig. 5.8e), which features an usual accumulation of electrons in the downward polarized

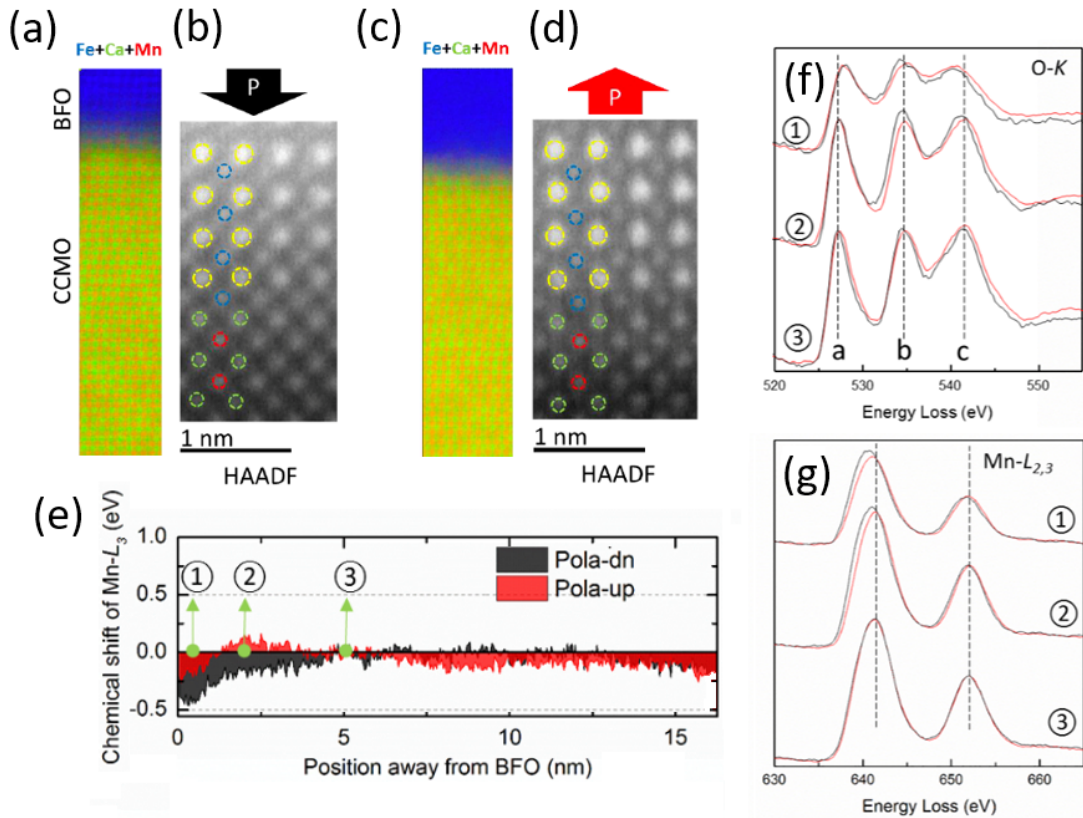


Figure 5.8: The RGB images constructed by the atomic EELS chemical mapping of Fe-L_{2,3} (blue), Ca-L_{2,3} (green) and Mn-L_{2,3} (red) across the $\text{Ca}_{0.96}\text{Ce}_{0.04}\text{MnO}_3$ thin film for (a) downward and (c) upward polarization states, respectively. HAADF images of the corresponding BiFeO₃/ $\text{Ca}_{0.96}\text{Ce}_{0.04}\text{MnO}_3$ interfaces for (b) downward and (d) upward polarization states, where the Bi, Fe, Ca, and Mn atoms are indicated by yellow, blue, green and red open circles, respectively. (e) Chemical shift of Mn-L₃ edge per unit cell across the (Ca,Ce)MnO₃ layer for the downward (black) and upward (red) polarization states. The zero reference of the profile is the nominal stoichiometry $\text{Ca}_{0.96}\text{Ce}_{0.04}\text{MnO}_3$ where the Mn valence is +3.92 with Mn-L₃ edge at 641.31 eV. The spectra of the (f) O-K and (g) Mn-L_{2,3} edge at three different positions indicated in (e) for both downward (black) and upward (red) polarization states.

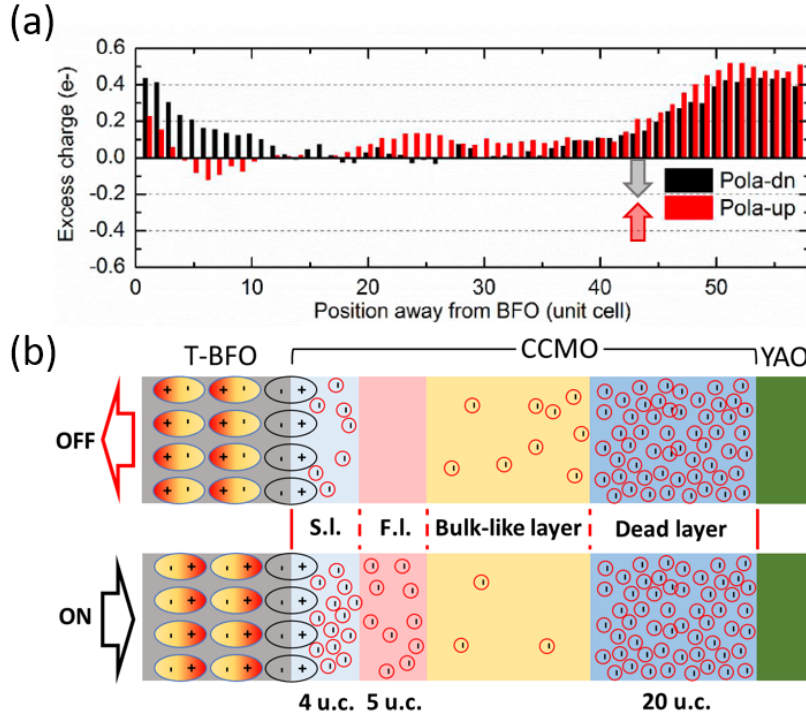


Figure 5.9: (a) Excess charge per unit cell scale across the $(\text{Ca,Ce})\text{MnO}_3$ layer for the downward (black) and upward (red) polarization states. The zero reference of the profile is the nominal stoichiometry $\text{Ca}_{0.96}\text{Ce}_{0.04}\text{MnO}_3$ where the Mn valence is $+3.92$ with Mn- L_3 edge at 641.31 eV. (b) Schematic illustration of the behavior of different layers of CaMnO_3 in response to the ferroelectric switching. S.l. stands for "screening layer" and F.l for "function layer".

state, although of a small magnitude. Regardless, its flat Mn- L_3 profile with low chemical shift is consistent with the metallicity of 4% Ce-doped CaMnO_3 samples. The electron distribution features a clear modulation in the first 13 unit cells of the manganite, where the excess of electrons is lowered for the upward polarization with an effective charge modulation of $2.38 e^-$ corresponding to a sheet carrier density variation of $10 - 20 \times 10^{14} \text{ cm}^{-2}$. This is within the range of the expected modulation of BiFeO_3 with a polarization of the order of $100 \mu\text{C cm}^{-2}$ ($12.5 \times 10^{14} \text{ cm}^{-2}$), showing the expected ferroelectric field-effect, although only at a local scale.

Ce-doped CaMnO_3 thin films are metallic only in a very small region, and for 4% doping a reduction in carrier density of only $0.04 e^-/\text{u.c.}$ is needed to reach the metal-insulator transition at 2% doping. According to the excess charge profile, this critical value is reached only between the 5th and the 9th unit cell. Hence, the first 4 unit cells (position 1 in Fig. 5.8e) can be regarded as the charge-screening layer, while the successive 5 unit cells (position 2 in Fig. 5.8e) are the function layer, which may achieve a metal-insulator transition upon switching the polarization of the BiFeO_3 top layer. This division into different functional layers is shown in Fig. 5.9b.

Overall, a proper switching of the polarization of BiFeO₃ induces a charge modulation of $2.3 e^-$ in the underlying Ce-doped CaMnO₃ layer. In 20 nm-thick manganite layers, this corresponds to a modulation of $0.048 e^-/\text{u.c.}$ Due to the interface being switched by only 19%, this brings the effective charge modulation to a small $9 \times 10^{-3} e^-/\text{u.c.}$ This is consistent with the 4 – 5% modulation of resistivity (Fig. 5.4). These results show that, while the bulk of the Ce-doped CaMnO₃ is not affected by the polarization change of BiFeO₃, due to the limited switching dynamics, there is a substantial electron accumulation/depletion in 10 u.c.-deep regions adjacent to the effectively switched interfaces. In these regions, the change in electron density is consistent with the polarization of BiFeO₃, but is insufficient to switch the bulk of the manganite electrode.

Chapter 6

Conclusions and Perspectives

In this thesis we have studied the electronic and topological properties of Ce-doped CaMnO_3 through magnetotransport measurements, angle-resolved photoemission spectroscopy and magnetic force microscopy. Here, we summarize the main results of our studies and possible future investigations based on our conclusions.

6.1 Summary

In chapter three we have reported our combined angle-resolved photoemission spectroscopy measurements and density functional theory simulations which showed the presence of two separate charge carriers: light 3D electrons in the $e_g 3z^2 - r^2$ -derived Fermi sphere around Γ , and heavy quasi-2D polarons in $e_g x^2 - y^2$ cylinders. The difference in band structure between the two carriers can be ascribed to a difference in electron-phonon interaction. In the quasi-2D bands, static correlations push the conduction band upwards, reducing the bandwidth between the bottom of the occupied band and the Fermi energy. This destroys the single-particle picture of these carriers, invoking vertex corrections that transform the electron band into a "waterfall", which corresponds to the formation of polaron quasi-particles. Although these polarons have a much higher mass compared to the 3D electrons, their carrier density is high enough so that they dominate electron transport nonetheless. These results suggest that, in manganites, as the metal-insulator transition is crossed, polarons form due to an enhancement of the electron-phonon coupling, if they interact with phonons of comparable energies.

In chapter four we have shown the Hall effect of a 4% doped CaMnO_3 thin film. At temperatures higher than the transition temperature T_C , the Hall effect was linear, as expected by the ordinary Hall effect in a paramagnetic manganite. At lower temperatures, the Hall effect started featuring a hysteresis loop, proportional to the magnetization of the sample, corresponding to an anomalous Hall effect. At even

lower temperatures, two asymmetric peaks started to develop after the coercive fields. This third component resembles the topological Hall effect, and suggests that there are topological charges nucleated after magnetization reversal. This topological Hall effect disappears when the epitaxial strain is reduced, suggesting a role of the anisotropy in stabilizing topological charge.

Magnetic force microscopy images show that there are magnetic bubbles nucleated over and beyond the coercive field, and that the density of measured bubbles closely follows the measured topological Hall effect throughout all temperatures. This suggests that the topological charges giving rise to the measured Hall effect are carried by the magnetic bubbles, although no direct measurement of the topology of the bubbles could be carried out due to the technical difficulties of performing Lorentz transmission electron microscopy in oxide thin films. A series of experiments showed how no Dzyaloshinskii–Moriya interaction is present. On the other hand, these magnetic bubble domains have the same size and behavior of skyrmion bubbles (i.e. topological magnetic bubbles) observed in bulk manganites, and recently thin films. Hence, we postulate that the measured topological Hall effect is caused by skyrmion bubbles nucleated at magnetization reversal, whose topology is stabilized by strong dipole interaction rather than Dzyaloshinskii–Moriya interaction.

The amplitude of the topological Hall effect of a 4% doped sample is two orders of magnitude higher than what one could expect from the measured density of skyrmion bubbles. As seen by measuring the doping dependence of the topological Hall effect, this disagreement increases at lower dopings, where the topological Hall effect diverges. This can be interpreted by a recently developed topological Hall theory in the weak coupling regime, where additional non-adiabatic contributions are relevant, compared to the conventional adiabatic strong-coupling model commonly used. In this model, the effect become proportional to the effective mass of the carriers, which is enhanced by correlations.

In chapter five we have shown how the strong sensitivity of the electronic of the manganite could be exploited by growing bilayers with a ferroelectric gate, where the polarization of the top layer induces a change in carrier density in the manganite electrode. By switching the polarization of the ferroelectric material, changes in the properties of the manganite can be induced. We grew $\text{BiFeO}_3/(\text{Ca,Ce})\text{MnO}_3$ bilayers with 2% and 5% dopings (close to metallic and magnetic transitions), where the polarization of the top ferroelectric layers could be measured and switched by piezoresponse force microscopy. However, we could not measure any induced change in the electronic properties of the samples.

To gain insight into the switching mechanisms of BiFeO_3 and the local electronic structure of the $(\text{Ca,Ce})\text{MnO}_3$, we performed scanning transmission electron microscopy measurements. These showed that the polarization of BiFeO_3 is switched

by nucleating domains with opposite polarization at the interfaces, which then propagate towards the manganite electrode. While the majority of the BiFeO_3 is switched, only a small fraction of the polarization at the interface is switched due to polarization pinning at the interface. By measuring the local carrier density underneath both switched and unswitched interfaces, we saw that the ferroelectric polarization indeed induces a change in the electron density of the manganite layer, but this change is not large enough to be measured in the whole manganite due to the small fraction of switched interface polarization.

6.2 Perspectives

Our findings on the formation of metallic bands and electron-phonon coupling show how the formation of polaron quasi-particles can depend on band filling. Thus, one way of tuning the electron-phonon coupling could be by tuning the strain, growing the same samples with smaller lattice mismatch, which would alter the band filling of both carriers. Additionally, samples with higher doping levels could be measured with the same angle-resolved photoemission spectroscopy techniques to investigate the band structure and electron-phonon interaction when orbital ordering and monoclinic distortions appear in the 6 – 10% Ce doping range. Previous works on the electronic structure of $\text{La}_{1-x}\text{Sr}_x\text{MnO}_3$ [96, 94] could also be expanded by studying in the detail the energies of the bosonic excitations, in order to study the role of electron-boson coupling in the formation of polarons in system with higher band filling than electron-doped CaMnO_3 .

Our work on the topological Hall effect of perovskite manganite, together with the recent report from Nakamura and colleagues [107], suggests that this novel phenomenon can be also tuned by strain engineering. For example, by growing the thin films on (111)-oriented YAlO_3 substrates would orient the magnetization diagonally out-of-plane, reducing its in-plane component compared to sample grown on (001)-oriented YAlO_3 while maintaining a strong magnetic anisotropy. This has been shown to enhance the formation of skyrmion bubbles and thus the topological Hall effect in $\text{La}_{0.7}\text{Sr}_{0.3}\text{Mn}_{0.95}\text{Ru}_{0.05}\text{O}_3$ thin films [107]. The topological Hall effect could also be tuned by gating our manganite thin films with a ferroelectric material in order to modulate the carrier density and thus the topological Hall effect by the ferroelectric polarization [177, 178]. Additionally, our work showed how correlations can influence electron transport in the presence of topological structures, and in particular enhance the topological Hall effect. As such enhancement appears to be a recurring feature in manganites [107], and oxides in general [111], which commonly host strong correlations, a detailed theoretical treatment of these phenomena should be initiated.

We have also shown how the ferroelectric control of Mott transistors is hindered

by polarization pinning at the interface. In our $\text{BiFeO}_3/(\text{Ca,Ce})\text{MnO}_3$ bilayers this effect may be diminished by reducing the dead layer of the manganite, by introducing a CaMnO_3 buffer layer between $(\text{Ca,Ce})\text{MnO}_3$ and the substrate. This would enable us to obtain a metallic ultra-thin film with a thickness of the effective functional layer we observed (10 u.c.). In order to remove the unswitchable ferroelectric dead layer, a 1 u.c. buffer layer could be introduced between the manganite and the ferroelectric in order to form a non-polar interface with the BiFeO_3 , optimizing the ferroelectric switching at the interface [176].

Bibliography

- [1] Skyrme, T. H. R. (1962). A unified field theory of mesons and baryons. *Nuclear Physics*, 31, 556-569.
- [2] Malozemoff, A. P. & Slonczewski, J. C. Magnetic Domain Walls in Bubble Materials. Academic press.
- [3] Nagaosa, N., & Tokura, Y. (2013). Topological properties and dynamics of magnetic skyrmions. *Nature Nanotechnology*, 8(12), 899.
- [4] Dzyaloshinsky, I. (1958). A thermodynamic theory of “weak” ferromagnetism of antiferromagnetics. *Journal of Physics and Chemistry of Solids*, 4(4), 241-255.
- [5] Moriya, T. (1960). Anisotropic superexchange interaction and weak ferromagnetism. *Physical Review*, 120(1), 91.
- [6] Grundy, P. J., & Herd, S. R. (1973). Lorentz microscopy of bubble domains and changes in domain wall state in hexaferrites. *physica status solidi (a)*, 20(1), 295-307.
- [7] Yu, X., Mostovoy, M., Tokunaga, Y., Zhang, W., Kimoto, K., Matsui, Y., ... & Tokura, Y. (2012). Magnetic stripes and skyrmions with helicity reversals. *Proceedings of the National Academy of Sciences*, 109(23), 8856-8860.
- [8] Ou-Yang, T. Y., Shu, G. J., Lin, J. Y., Hu, C. D., & Chou, F. C. (2015). Mn vacancy defects, grain boundaries, and A-phase stability of helimagnet MnSi. *Journal of Physics: Condensed Matter*, 28(2), 026004.
- [9] Mühlbauer, S., Binz, B., Jonietz, F., Pfleiderer, C., Rosch, A., Neubauer, A., ... & Böni, P. (2009). Skyrmion lattice in a chiral magnet. *Science*, 323(5916), 915-919.

- [10] Yu, X. Z., Onose, Y., Kanazawa, N., Park, J. H., Han, J. H., Matsui, Y., ... & Tokura, Y. (2010). Real-space observation of a two-dimensional skyrmion crystal. *Nature*, 465(7300), 901.
- [11] Heinze, S., Von Bergmann, K., Menzel, M., Brede, J., Kubetzka, A., Wiesendanger, R., ... & Blügel, S. (2011). Spontaneous atomic-scale magnetic skyrmion lattice in two dimensions. *Nature Physics*, 7(9), 713.
- [12] Fert, A., Cros, V., & Sampaio, J. (2013). Skyrmions on the track. *Nature Nanotechnology*, 8(3), 152.
- [13] Okubo, T., Chung, S., & Kawamura, H. (2012). Multiple-q states and the skyrmion lattice of the triangular-lattice Heisenberg antiferromagnet under magnetic fields. *Physical Review Letters*, 108(1), 017206.
- [14] Kurumaji, T., Nakajima, T., Hirschberger, M., Kikkawa, A., Yamasaki, Y., Sagayama, H., ... & Tokura, Y. (2018). Skyrmion lattice with a giant topological Hall effect in a frustrated triangular-lattice magnet. *arXiv preprint arXiv:1805.10719*.
- [15] Chen, G., Mascaraque, A., N'Diaye, A. T., & Schmid, A. K. (2015). Room temperature skyrmion ground state stabilized through interlayer exchange coupling. *Applied Physics Letters*, 106(24), 242404.
- [16] Legrand, W., Maccariello, D., Reyren, N., Garcia, K., Moutafis, C., Moreau-Luchaire, C., ... & Fert, A. (2017). Room-temperature current-induced generation and motion of sub-100 nm skyrmions. *Nano Letters*, 17(4), 2703-2712.
- [17] Hsu, P. J., Kubetzka, A., Finco, A., Romming, N., von Bergmann, K., & Wiesendanger, R. (2017). Electric-field-driven switching of individual magnetic skyrmions. *Nature Nanotechnology*, 12(2), 123.
- [18] Romming, N., Hanneken, C., Menzel, M., Bickel, J. E., Wolter, B., von Bergmann, K., ... & Wiesendanger, R. (2013). Writing and deleting single magnetic skyrmions. *Science*, 341(6146), 636-639.
- [19] Maccariello, D., Legrand, W., Reyren, N., Garcia, K., Bouzehouane, K., Collin, S., ... & Fert, A. (2018). Electrical detection of single magnetic skyrmions in metallic multilayers at room temperature. *Nature Nanotechnology*, 13(3), 233.
- [20] Fert, A., Reyren, N., & Cros, V. (2017). Magnetic skyrmions: advances in physics and potential applications. *Nature Reviews Materials*, 2(7), 17031.
- [21] Parkin, S., & Yang, S. H. (2015). Memory on the racetrack. *Nature Nanotechnology*, 10(3), 195.

- [22] Zhang, X., Ezawa, M., & Zhou, Y. (2015). Magnetic skyrmion logic gates: conversion, duplication and merging of skyrmions. *Scientific reports*, 5, 9400.
- [23] Pinna, D., Araujo, F. A., Kim, J. V., Cros, V., Querlioz, D., Bessiere, P., ... & Grollier, J. (2018). Skyrmion gas manipulation for probabilistic computing. *Physical Review Applied*, 9(6), 064018.
- [24] Ma, F., Zhou, Y., Braun, H. B., & Lew, W. S. (2015). Skyrmion-based dynamic magnonic crystal. *Nano Letters*, 15(6), 4029-4036.
- [25] Finocchio, G., Ricci, M., Tomasello, R., Giordano, A., Lanuzza, M., Puliafito, V., ... & Carpentieri, M. (2015). Skyrmion based microwave detectors and harvesting. *Applied Physics Letters*, 107(26), 262401.
- [26] Aharonov, Y., & Bohm, D. (1959). Significance of electromagnetic potentials in the quantum theory. *Physical Review*, 115(3), 485.
- [27] Berry, M. V. (1984). Quantal phase factors accompanying adiabatic changes. *Proceedings of the Royal Society of London. A. Mathematical and Physical Sciences*, 392(1802), 45-57.
- [28] Bruno, P., Dugaev, V. K., & Taillefumier, M. (2004). Topological Hall effect and Berry phase in magnetic nanostructures. *Physical Review Letters*, 93(9), 096806.
- [29] Li, Y., Kanazawa, N., Yu, X. Z., Tsukazaki, A., Kawasaki, M., Ichikawa, M., ... & Tokura, Y. (2013). Robust formation of skyrmions and topological Hall effect anomaly in epitaxial thin films of MnSi. *Physical Review Letters*, 110(11), 117202.
- ss
- [30] Neubauer, A., Pfleiderer, C., Binz, B., Rosch, A., Ritz, R., Niklowitz, P. G., & Böni, P. (2009). Topological Hall effect in the A phase of MnSi. *Physical Review Letters*, 102(18), 186602.
- [31] Shiomi, Y., Iguchi, S., & Tokura, Y. (2012). Emergence of topological Hall effect from fanlike spin structure as modified by Dzyaloshinsky-Moriya interaction in MnP. *Physical Review B*, 86(18), 180404.
- [32] Hall, E. H. (1881). XVIII. On the "Rotational Coefficient" in nickel and cobalt. *The London, Edinburgh, and Dublin Philosophical Magazine and Journal of Science*, 12(74), 157-172.
- [33] Pugh, E. M., & Lippert, T. W. (1932). Hall emf and intensity of magnetization. *Physical Review*, 42(5), 709.

- [34] Karplus, R., & Luttinger, J. M. (1954). Hall effect in ferromagnetics. *Physical Review*, 95(5), 1154.
- [35] Nagaosa, N., Sinova, J., Onoda, S., MacDonald, A. H., & Ong, N. P. (2010). Anomalous hall effect. *Reviews of modern physics*, 82(2), 1539.
- [36] Onoda, M., & Nagaosa, N. (2002). Topological *Nature* of anomalous Hall effect in ferromagnets. *Journal of the Physical Society of Japan*, 71(1), 19-22.
- [37] Smit, J. (1958). The spontaneous Hall effect in ferromagnetics II. *Physica*, 24(1-5), 39-51.
- [38] Berger, L. (1970). Side-jump mechanism for the Hall effect of ferromagnets. *Physical Review B*, 2(11), 4559.
- [39] Bowen, M., Bibes, M., Barthélémy, A., Contour, J. P., Anane, A., Lemaitre, Y., & Fert, A. (2003). Nearly total spin polarization in $\text{La}_{2/3}\text{Sr}_{1/3}\text{MnO}_3$ from tunneling experiments. *Applied Physics Letters*, 82(2), 233-235.
- [40] Goldschmidt, V. M. (1926). Die gesetze der krystallochemie. *Naturwissenschaften*, 14(21), 477-485.
- [41] Goldschmidt, V. M. (1970). *Geochemistry*, Oxford University Press .
- [42] Coey, J. M. (2010). *Magnetism and magnetic materials*. Cambridge university press.
- [43] S. Blundell, *Magnetism in Condensed Matter Physics*. Oxford University Press (2001).
- [44] Panwar, N., Coondoo, I., Sen, V., & Agarwal, S. K. (2011). Structural, Morphological, Magneto-Transport and Thermal Properties of Antimony Substituted (La, Pr) $_{2/3}\text{Ba}_{1/3}\text{Mn}_{1-x}\text{Sb}_x\text{O}_3$ Perovskite Manganites. *Advances in Ceramics-Electric and Magnetic Ceramics, Bioceramics, Ceramics and Environment*. In-Tech.
- [45] Jahn, H. A., & Teller, E. (1937). Stability of polyatomic molecules in degenerate electronic states-I—Orbital degeneracy. *Proceedings of the Royal Society of London. Series A-Mathematical and Physical Sciences*, 161(905), 220-235.
- [46] Jena, A., & Nanda, B. R. K. (2016). Unconventional Magnetism and Band Gap Formation in LiFePO_4 : Consequence of Polyanion Induced Non-planarity. *Scientific reports*, 6, 19573.
- [47] Coey, J. M. D., Viret, M. V., & Von Molnar, S. (1999). Mixed-valence manganites. *Advances in physics*, 48(2), 167-293.

- [48] Mott, N. F., & Peierls, R. (1937). Discussion of the paper by de Boer and Verwey. *Proceedings of the Physical Society*, 49(4S), 72.
- [49] Hubbard, J. (1964). Electron correlations in narrow energy bands III. An improved solution. *Proc. R. Soc. London, Ser. A*, 281, 401.
- [50] Emery, V. J. (1987). Theory of high- T_C superconductivity in oxides. *Physical Review Letters*. 58, 279.
- [51] Kittel, Charles (2005), Introduction to Solid State Physics (8th ed.), John Wiley & Sons, p. 407–409.
- [52] Varignon, J., Bibes, M., & Zunger, A. (2019). Origin of band gaps in 3d perovskite oxides. *arXiv preprint arXiv:1901.00829*.
- [53] Goodenough, J. B. (1955). Theory of the role of covalence in the perovskite-type manganites $[\text{La}, \text{M}(\text{II})]\text{MnO}_3$. *Physical Review*, 100(2), 564.
- [54] Kanamori, J. (1959). Superexchange interaction and symmetry properties of electron orbitals. *Journal of Physics and Chemistry of Solids*, 10(2-3), 87-98.
- [55] Zener, C. (1951). Interaction between the d-shells in the transition metals. II. Ferromagnetic compounds of manganese with perovskite structure. *Physical Review*, 82(3), 403.
- [56] Fujishiro, H., Fukase, T., & Ikebe, M. (1998). Charge ordering and sound velocity anomaly in $\text{La}_{1-x}\text{Sr}_x\text{MnO}_3$ ($x \geq 0.5$). *Journal of the Physical Society of Japan*, 67(8), 2582-2585.
- [57] Cheong, S. W., & Mostovoy, M. (2007). Multiferroics: a magnetic twist for ferroelectricity. *Nature materials*, 6(1), 13.
- [58] Talbayev, D., Mihály, L., & Zhou, J. (2004). Antiferromagnetic Resonance in LaMnO_3 at Low Temperature. *Physical Review Letters*, 93(1), 017202.
- [59] Millis, A. J., Littlewood, P. B., & Shraiman, B. I. (1995). Double exchange alone does not explain the resistivity of $\text{La}_{1-x}\text{Sr}_x\text{MnO}_3$. *Physical Review Letters*, 74(25), 5144.
- [60] Chattopadhyay, A., Millis, A. J., & Sarma, S. D. (2000). Optical spectral weights and the ferromagnetic transition temperature of colossal-magnetoresistance manganites: Relevance of double exchange to real materials. *Physical Review B*, 61(16), 10738.

- [61] Alexandrov, A. S., Zhao, G. M., Keller, H., Lorenz, B., Wang, Y. S., & Chu, C. W. (2001). Evidence for polaronic Fermi liquid in manganites. *Physical Review B*, 64(14), 140404.
- [62] Hartinger, C., Mayr, F., Deisenhofer, J., Loidl, A., & Kopp, T. (2004). Large and small polaron excitations in $\text{La}_{2/3}(\text{Sr/Ca})_{1/3}\text{MnO}_3$ films. *Physical Review B*, 69(10), 100403.
- [63] Hartinger, C., Mayr, F., Loidl, A., & Kopp, T. (2006). Polaronic excitations in colossal magnetoresistance manganite films. *Physical Review B*, 73(2), 024408.
- [64] Masee, F., De Jong, S., Huang, Y., Siu, W. K., Santoso, I., Mans, A., ... & Patthey, L. (2011). Bilayer manganites reveal polarons in the midst of a metallic breakdown. *Nature Physics*, 7(12), 978.
- [65] Weber, F., Aliouane, N., Zheng, H., Mitchell, J. F., Argyriou, D. N., & Reznik, D. (2009). SigNature of checkerboard fluctuations in the phonon spectra of a possible polaronic metal $\text{La}_{1.2}\text{Sr}_{1.8}\text{Mn}_2\text{O}_7$. *Nature materials*, 8(10), 798.
- [66] Ziman, J. M. (2001). *Electrons and phonons: the theory of transport phenomena in solids*. Oxford university press.
- [67] Egilmez, M., Chow, K. H., & Jung, J. (2008). Percolative model of the effect of disorder on the resistive peak broadening in $\text{La}_{2/3}\text{Ca}_{1/3}\text{MnO}_3$ near the metal-insulator transition. *Applied Physics Letters*, 92(16), 162515.
- [68] Snyder, G. J., Hiskes, R., DiCarolis, S., Beasley, M. R., & Geballe, T. H. (1996). Intrinsic electrical transport and magnetic properties of $\text{La}_{0.67}\text{Ca}_{0.33}\text{MnO}_3$ and $\text{La}_{0.67}\text{Sr}_{0.33}\text{MnO}_3$ MOCVD thin films and bulk material. *Physical Review B*, 53(21), 14434.
- [69] Jaime, M., Lin, P., Chun, S. H., Salamon, M. B., Dorsey, P., & Rubinstein, M. (1999). Coexistence of localized and itinerant carriers near T C in calcium-doped manganites. *Physical Review B*, 60(2), 1028.
- [70] Kadowaki, K., & Woods, S. B. (1986). Universal relationship of the resistivity and specific heat in heavy-fermion compounds. *Solid State Communications*, 58(8), 507-509.
- [71] Appel, J. (1968). Polarons. In *Solid State Physics* (Vol. 21, pp. 193-391). Academic Press.
- [72] Jaime, M., & Salamon, M. B. (2002). Electronic Transport in La-Ca Manganites. In *Physics of Manganites* (pp. 243-267). Springer, Boston, MA.

- [73] Bowen, M., Bibes, M., Barthélémy, A., Contour, J. P., Anane, A., Lemaitre, Y., & Fert, A. (2003). Nearly total spin polarization in $\text{La}_{2/3}\text{Sr}_{1/3}\text{MnO}_3$ from tunneling experiments. *Applied Physics Letters*, 82(2), 233-235.
- [74] Kubo, K., & Ohata, N. (1972). A quantum theory of double exchange. I. *Journal of the Physical society of Japan*, 33(1), 21-32.
- [75] Mercone, S., Perroni, C. A., Cataudella, V., Adamo, C., Angeloni, M., Aruta, C., ... & Petrov, A. Y. (2005). Transport properties in manganite thin films. *Physical Review B*, 71(6), 064415.
- [76] Mansuri, I., & Varshney, D. (2012). Structure and electrical resistivity of $\text{La}_{1-x}\text{Ba}_x\text{MnO}_3$ ($0.25 \leq x \leq 0.35$) perovskites. *Journal of Alloys and Compounds*, 513, 256-265.
- [77] Varshney, D., & Kaurav, N. (2004). Electrical resistivity in the ferromagnetic metallic state of La-Ca-MnO_3 : Role of electron-phonon interaction. *The European Physical Journal B-Condensed Matter and Complex Systems*, 40(2), 129-136.
- [78] Zhao, G. M., Smolyaninova, V., Prellier, W., & Keller, H. (2000). Electrical transport in the ferromagnetic state of manganites: Small-polaron metallic conduction at low temperatures. *Physical Review Letters*, 84(26), 6086.
- [79] Zhao, G. M., Kang, D. J., Prellier, W., Rajeswari, M., Keller, H., Venkatesan, T., & Greene, R. L. (2000). Strong oxygen-isotope effect on the intrinsic resistivity in the ferromagnetic state of manganites. *Physical Review B*, 63(6), 060402.
- [80] Lang, I. G., & Firsov, Y. A. (1963). Kinetic theory of semiconductors with low mobility. *Journal of Experimental and Theoretical Physics*, 16(5), 1301.
- [81] Graziosi, P., Gambardella, A., Prezioso, M., Riminucci, A., Bergenti, I., Homonay, N., ... & Busquets-Mataix, D. (2014). Polaron framework to account for transport properties in metallic epitaxial manganite films. *Physical Review B*, 89(21), 214411.
- [82] Sewell, G. L. (1958). Electrons in polar crystals. *Philosophical Magazine*, 3(36), 1361-1380.
- [83] Urushibara, A., Moritomo, Y., Arima, T., Asamitsu, A., Kido, G., & Tokura, Y. (1995). Insulator-metal transition and giant magnetoresistance in $\text{La}_{1-x}\text{Sr}_x\text{MnO}_3$. *Physical Review B*, 51(20), 14103.

- [84] Fröhlich, H. (1954). Electrons in lattice fields. *Advances in Physics*, 3(11), 325-361.
- [85] Alexandrov, A. S., & Mott, N. F. (1995). *Polarons & bipolarons* (p. 191). Singapore: World Scientific.
- [86] Mishchenko, A. S., Prokof'ev, N. V., Sakamoto, A., & Svistunov, B. V. (2000). Diagrammatic quantum Monte Carlo study of the Fröhlich polaron. *Physical Review B*, 62(10), 6317.
- [87] Holstein, T. (1959). Polaron motion. I. Molecular-crystal model. *Ann. Phys.*, 8(325), 343.
- [88] Hague, J. P., Kornilovitch, P. E., Alexandrov, A. S., & Samson, J. H. (2006). Effects of lattice geometry and interaction range on polaron dynamics. *Physical Review B*, 73(5), 054303.
- [89] Brinkman, W. F., & Rice, T. M. (1970). Application of Gutzwiller's variational method to the metal-insulator transition. *Physical Review B*, 2(10), 4302.
- [90] Dobrosavljevic, V., Trivedi, N. & Valles, J. M. *Conductor-Insulator Quantum Phase Transitions* (Oxford Univ. Press, Oxford, 2012).
- [91] Fujishima, Y., Tokura, Y., Arima, T., & Uchida, S. (1992). Optical-conductivity spectra of $\text{Sr}_{1-x}\text{La}_x\text{TiO}_3$: Filling-dependent effect of the electron correlation. *Physical Review B*, 46(17), 11167.
- [92] Sakai, H., Ishiwata, S., Okuyama, D., Nakao, A., Nakao, H., Murakami, Y., ... & Tokura, Y. (2010). Electron doping in the cubic perovskite SrMnO_3 : Isotropic metal versus chainlike ordering of Jahn-Teller polarons. *Physical Review B*, 82(18), 180409.
- [93] Zhang, J., McIlroy, D. N., & Dowben, P. A. (1995). Correlation between screening and electron effective mass across the nonmetal-metal transition in ultrathin films. *Physical Review B*, 52(15), 11380.
- [94] Chikamatsu, A., Wadati, H., Kumigashira, H., Oshima, M., Fujimori, A., Hamada, N., ... & Koinuma, H. (2006). Band structure and Fermi surface of $\text{La}_{0.6}\text{Sr}_{0.4}\text{MnO}_3$ thin films studied by in situ angle-resolved photoemission spectroscopy. *Physical Review B*, 73(19), 195105.
- [95] Krempaský, J., Strocov, V. N., Patthey, L., Willmott, P. R., Herger, R., Falub, M., ... & Heckmann, O. (2008). Effects of three-dimensional band structure in angle- and spin-resolved photoemission from half-metallic $\text{La}_{2/3}\text{Sr}_{1/3}\text{MnO}_3$. *Physical Review B*, 77(16), 165120.

- [96] Lev, L. L., Krempaský, J., Staub, U., Rogalev, V. A., Schmitt, T., Shi, M., ... & Tsetlin, M. B. (2015). Fermi Surface of Three-Dimensional $\text{La}_{1-x}\text{Sr}_x\text{MnO}_3$ Explored by Soft-X-Ray ARPES: Rhombohedral Lattice Distortion and its Effect on Magnetoresistance. *Physical Review Letters*, 114(23), 237601.
- [97] Matl, P., Ong, N. P., Yan, Y. F., Li, Y. Q., Studebaker, D., Baum, T., & Doubinina, G. (1998). Hall effect of the colossal magnetoresistance manganite $\text{La}_{1-x}\text{Ca}_x\text{MnO}_3$. *Physical Review B*, 57(17), 10248.
- [98] Ye, J., Kim, Y. B., Millis, A. J., Shraiman, B. I., Majumdar, P., & Tešanović, Z. (1999). Berry phase theory of the anomalous Hall effect: application to colossal magnetoresistance manganites. *Physical Review Letters*, 83(18), 3737.
- [99] Calderón, M. J., & Brey, L. (2001). Skyrmion strings contribution to the anomalous Hall effect in double-exchange systems. *Physical Review B*, 63(5), 054421.
- [100] Chun, S. H., Salamon, M. B., Lyanda-Geller, Y., Goldbart, P. M., & Han, P. D. (2000). Magnetotransport in manganites and the role of quantal phases: Theory and experiment. *Physical Review Letters*, 84(4), 757.
- [101] Nagai, T., Nagao, M., Kurashima, K., Asaka, T., Zhang, W., & Kimoto, K. (2012). Formation of nanoscale magnetic bubbles in ferromagnetic insulating manganite $\text{La}_{7/8}\text{Sr}_{1/8}\text{MnO}_3$. *Applied Physics Letters*, 101(16), 162401.
- [102] Nagao, M., So, Y. G., Yoshida, H., Isobe, M., Hara, T., Ishizuka, K., & Kimoto, K. (2013). Direct observation and dynamics of spontaneous skyrmion-like magnetic domains in a ferromagnet. *Nature Nanotechnology*, 8(5), 325.
- [103] Kotani, A., Nakajima, H., Ishii, Y., Harada, K., & Mori, S. (2016). Observation of spin textures in $\text{La}_{1-x}\text{Sr}_x\text{MnO}_3$ ($x = 0.175$). *AIP Advances*, 6(5), 056403.
- [104] Yu, X., Tokunaga, Y., Taguchi, Y., & Tokura, Y. (2017). Variation of topology in magnetic bubbles in a colossal magnetoresistive manganite. *Advanced Materials*, 29(3), 1603958.
- [105] Ohuchi, Y., Kozuka, Y., Uchida, M., Ueno, K., Tsukazaki, A., & Kawasaki, M. (2015). Topological Hall effect in thin films of the Heisenberg ferromagnet EuO . *Physical Review B*, 91(24), 245115.
- [106] Ahadi, K., Galletti, L., & Stemmer, S. (2017). Evidence of a topological Hall effect in $\text{Eu}_{1-x}\text{Sm}_x\text{TiO}_3$. *Applied Physics Letters*, 111(17), 172403.
- [107] Nakamura, M., Morikawa, D., Yu, X., Kagawa, F., Arima, T. H., Tokura, Y., & Kawasaki, M. (2018). Emergence of topological Hall effect in half-metallic

- manganite thin films by tuning perpendicular magnetic anisotropy. *Journal of the Physical Society of Japan*, 87(7), 074704.
- [108] Ziese, M., & Lindfors-Vrejoiu, I. (2018). Hall effect of asymmetric $\text{La}_{0.7}\text{Sr}_{0.3}\text{MnO}_3/\text{SrTiO}_3/\text{SrRuO}_3$ and $\text{La}_{0.7}\text{Sr}_{0.3}\text{MnO}_3/\text{BaTiO}_3/\text{SrRuO}_3$ superlattices. *Journal of Applied Physics*, 124(16), 163905.
- [109] Kan, D., Moriyama, T., Kobayashi, K., & Shimakawa, Y. (2018). Alternative to the topological interpretation of the transverse resistivity anomalies in SrRuO_3 . *Physical Review B*, 98(18), 180408.
- [110] Wang, L., Feng, Q., Kim, Y., Kim, R., Lee, K. H., Pollard, S. D., ... & Meng, W. (2018). Ferroelectrically tunable magnetic skyrmions in ultrathin oxide heterostructures. *Nature materials*, 17(12), 1087.
- [111] Matsuno, J., Ogawa, N., Yasuda, K., Kagawa, F., Koshibae, W., Nagaosa, N., ... & Kawasaki, M. (2016). Interface-driven topological Hall effect in $\text{SrRuO}_3/\text{SrIrO}_3$ bilayer. *Science advances*, 2(7), e1600304.
- [112] Bocquet, A. E., Mizokawa, T., Morikawa, K., Fujimori, A., Barman, S. R., Maiti, K., ... & Onoda, M. (1996). Electronic structure of early 3d-transition-metal oxides by analysis of the 2p core-level photoemission spectra. *Physical Review B*, 53(3), 1161.
- [113] Caspi, E. A. N., Avdeev, M., Short, S., Jorgensen, J. D., Lobanov, M. V., Zeng, Z., ... & Stephens, P. W. (2004). Structural and magnetic phase diagram of the two-electron-doped $(\text{Ca}_{1-x}\text{Ce}_x)\text{MnO}_3$ system: Effects of competition among charge, orbital, and spin ordering. *Physical Review B*, 69(10).
- [114] Bousquet, E., & Spaldin, N. (2011). Induced Magnetoelectric Response in Pnma Perovskites. *Physical Review Letters*, 107(19), 197603.
- [115] Molinari, M., Tompsett, D. A., Parker, S. C., Azough, F., & Freer, R. (2014). Structural, electronic and thermoelectric behaviour of CaMnO_3 and $\text{CaMnO}_{3-\delta}$. *Journal of Materials Chemistry A*, 2(34), 14109-14117.
- [116] Millis, A. J. (1997). Orbital ordering and superexchange in manganite oxides. *Physical Review B*, 55(10), 6405.
- [117] Bousquet, E., & Cano, A. (2016). Non-collinear magnetism in multiferroic perovskites. *Journal of Physics: Condensed Matter*, 28(12), 123001.
- [118] Zeng, Z., Greenblatt, M., & Croft, M. (2001). Charge ordering and magnetoresistance of $\text{Ca}_{1-x}\text{Ce}_x\text{MnO}_3$. *Physical Review B*, 63(22), 224410.

- [119] Ohnishi, H., Kosugi, T., Miyake, T., Ishibashi, S., & Terakura, K. (2012). Spin-canting in lightly electron-doped CaMnO_3 . *Physical Review B*, 85(16), 165128.
- [120] Solovyev, I. V., & Terakura, K. (2001). Spin canting in three-dimensional perovskite manganites. *Physical Review B*, 63(17), 174425.
- [121] De Gennes, P. G. (1960). Effects of double exchange in magnetic crystals. *Physical Review*, 118(1), 141.
- [122] Meskine, H., & Satpathy, S. (2005). Self-trapped magnetic polaron in electron-doped CaMnO_3 . *Journal of Physics: Condensed Matter*, 17(12), 1889.
- [123] Alexandrov, A. S., & Bratkovsky, A. M. (2000). Alexandrov and Bratkovsky reply. *Physical Review Letters*, 84(9), 2043.
- [124] Xiang, P. H., Yamada, H., Sawa, A., & Akoh, H. (2009). Strain-controlled electronic properties and magnetorelaxor behaviors in electron-doped CaMnO_3 thin films. *Applied Physics Letters*, 94(6), 062109.
- [125] Xiang, P. H., Yamada, H., Akoh, H., & Sawa, A. (2012). Phase diagrams of strained $\text{Ca}_{1-x}\text{Ce}_x\text{MnO}_3$ films. *Journal of Applied Physics*, 112(11), 113703.
- [126] Sando, D., Barthélémy, A., & Bibes, M. (2014). BiFeO_3 epitaxial thin films and devices: past, present and future. *Journal of Physics: Condensed Matter*, 26(47), 473201.
- [127] Li, J., Wang, J., Wuttig, M., Ramesh, R., Wang, N., Ruetter, B., ... & Viehland, D. (2004). Dramatically enhanced polarization in (001), (101), and (111) BiFeO_3 thin films due to epitaxial-induced transitions. *Applied Physics Letters*, 84(25), 5261-5263.
- [128] Ahn, C. H., Bhattacharya, A., Di Ventura, M., Eckstein, J. N., Frisbie, C. D., Gershenson, M. E., ... & Morpurgo, A. F. (2006). Electrostatic modification of novel materials. *Reviews of Modern Physics*, 78(4), 1185.
- [129] Crassous, A., Bernard, R., Fusil, S., Bouzouane, K., Le Bourdais, D., Enouz-Vedrenne, S., ... & Villegas, J. E. (2011). Nanoscale electrostatic manipulation of magnetic flux quanta in ferroelectric/superconductor $\text{BiFeO}_3/\text{YBa}_2\text{Cu}_3\text{O}_7$ heterostructures. *Physical Review Letters*, 107(24), 247002.
- [130] Yamada, H., Marinova, M., Altuntas, P., Crassous, A., Bégon-Lours, L., Fusil, S., ... & Bibes, M. (2013). Ferroelectric control of a Mott insulator. *Scientific reports*, 3, 2834.

- [131] Marinova, M., Rault, J. E., Gloter, A., Nemsak, S., Palsson, G. K., Rueff, J. P., ... & Garcia, V. (2015). Depth profiling charge accumulation from a ferroelectric into a doped mott insulator. *Nano Letters*, 15(4), 2533-2541.
- [132] Takahashi, K. S., Matthey, D., Jaccard, D., Triscone, J. M., Shibuya, K., Ohnishi, T., & Lippmaa, M. (2004). Electrostatic modulation of the electronic properties of Nb-doped SrTiO₃ superconducting films. *Applied Physics Letters*, 84(10), 1722-1724.
- [133] Takahashi, K. S., Gabay, M., Jaccard, D., Shibuya, K., Ohnishi, T., Lippmaa, M., & Triscone, J. M. (2006). Local switching of two-dimensional superconductivity using the ferroelectric field effect. *Nature*, 441(7090), 195.
- [134] Marshall, M. S., Malashevich, A., Disa, A. S., Han, M. G., Chen, H., Zhu, Y., ... & Ahn, C. H. (2014). Conduction at a ferroelectric interface. *Physical Review Applied*, 2(5), 051001.
- [135] Mathews, S., Ramesh, R., Venkatesan, T., & Benedetto, J. (1997). Ferroelectric field effect transistor based on epitaxial perovskite heterostructures. *Science*, 276(5310), 238-240.
- [136] Hong, X., Posadas, A., & Ahn, C. H. (2005). Examining the screening limit of field effect devices via the metal-insulator transition. *Applied Physics Letters*, 86(14), 142501.
- [137] Hoffman, J., Hong, X., & Ahn, C. H. (2011). Device performance of ferroelectric/correlated oxide heterostructures for non-volatile memory applications. *Nanotechnology*, 22(25), 254014.
- [138] Chen, X., Zhang, X., Koten, M. A., Chen, H., Xiao, Z., Zhang, L., ... & Hong, X. (2017). Interfacial Charge Engineering in Ferroelectric-Controlled Mott Transistors. *Advanced Materials*, 29(31), 1701385.
- [139] Harano, T., Shibata, G., Yoshimatsu, K., Ishigami, K., Verma, V. K., Takahashi, Y., ... & Chang, F. H. (2015). Phase diagram of Ca_{1-x}Ce_xMnO₃ thin films studied by X-ray magnetic circular dichroism. *Solid State Communications*, 207, 50-53.
- [140] Kavich, J. J., Warusawithana, M. P., Freeland, J. W., Ryan, P., Zhai, X., Kodama, R. H., & Eckstein, J. N. (2007). Nanoscale suppression of magnetization at atomically assembled manganite interfaces: XMCD and XRMS measurements. *Physical Review B*, 76(1), 014410.
- [141] Goodenough, J. B., & Zhou, J. S. (2007). Orbital ordering in orthorhombic perovskites. *Journal of Materials Chemistry*, 17(23), 2394-2405.

- [142] Vaz, D. C., Lesne, E., Sander, A., Naganuma, H., Jacquet, E., Santamaria, J., ... & Bibes, M. (2018). Growth and Electrostatic/chemical Properties of Metal/LaAlO₃/SrTiO₃ Heterostructures. *JoVE (Journal of Visualized Experiments)*, (132), e56951.
- [143] Wang, K. (2013). *Laser based fabrication of graphene*. In *Advances in Graphene Science*. InTech.
- [144] Niu, W., Gao, M., Wang, X., Song, F., Du, J., Wang, X., ... & Zhang, R. (2016). Evidence of weak localization in quantum interference effects observed in epitaxial La_{0.7}Sr_{0.3}MnO₃ ultrathin films. *Scientific reports*, 6, 26081.
- [145] Giannozzi, P., Andreussi, O., Brumme, T., Bunau, O., Nardelli, M. B., Calandra, M., ... & Colonna, N. (2017). Advanced capabilities for materials modelling with Quantum ESPRESSO. *Journal of Physics: Condensed Matter*, 29(46), 465901.
- [146] Straub, T., Claessen, R., Steiner, P., Hübner, S., Eyert, V., Friemelt, K., & Bucher, E. (1997). Many-body definition of a Fermi surface: application to angle-resolved photoemission. *Physical Review B*, 55(20), 13473.
- [147] Alexandrov, A. S. (Ed.). (2008). *Polarons in advanced materials* (Vol. 103). Springer Science & Business Media.
- [148] Feynman, R. P., Hellwarth, R. W., Iddings, C. K., & Platzman, P. M. (1962). Mobility of slow electrons in a polar crystal. *Physical Review*, 127(4), 1004.
- [149] Goian, V., Kamba, S., Borodavka, F., Nuzhnyy, D., Savinov, M., & Belik, A. A. (2015). The manifestation of spin-phonon coupling in CaMnO₃. *Journal of Applied Physics*, 117(16), 164103.
- [150] Mishra, S. K., Gupta, M. K., Mittal, R., Kolesnikov, A. I., & Chaplot, S. L. (2016). Spin-phonon coupling and high-pressure phase transitions of RMnO₃ (R = Ca and Pr): An inelastic neutron scattering and first-principles study. *Physical Review B*, 93(21), 214306.
- [151] Migdal, A. B. (1958). Interaction between electrons and lattice vibrations in a normal metal. *Journal of Experimental and Theoretical Physics*, 7(6), 996-1001.
- [152] Roy, B., Sau, J. D., & Sarma, S. D. (2014). Migdal's theorem and electron-phonon vertex corrections in Dirac materials. *Physical Review B*, 89(16), 165119.
- [153] Grimaldi, C., Pietronero, L., & Strässler, S. (1995). Nonadiabatic superconductivity: electron-phonon interaction beyond Migdal's theorem. *Physical Review Letters*, 75(6), 1158.

- [154] Ummarino, G. A., & Gonnelli, R. S. (1997). Breakdown of Migdal's theorem and intensity of electron-phonon coupling in high-T_c superconductors. *Physical Review B*, 56(22), R14279.
- [155] Vaz, D. C., Lesne, E., Sander, A., Naganuma, H., Jacquet, E., Santamaria, J., ... & Bibes, M. (2017). Tuning up or down the critical thickness in LaAlO₃/SrTiO₃ through in situ deposition of metal overlayers. *Advanced Materials*, 29(28), 1700486.
- [156] Millis, A. J., Littlewood, P. B., & Shraiman, B. I. (1995). Double exchange alone does not explain the resistivity of La_{1-x}Sr_xMnO₃. *Physical Review Letters*, 74(25), 5144.
- [157] Calderón, M. J., & Brey, L. (2001). Low-temperature resistivity in double-exchange systems. *Physical Review B*, 64(14), 140403.
- [158] Alexandrov, A. S., & Bratkovsky, A. M. (1999). Carrier density collapse and colossal magnetoresistance in doped manganites. *Physical Review Letters*, 82(1), 141.
- [159] Tupitsyn, I. S., Mishchenko, A. S., Nagaosa, N., & Prokof'ev, N. (2016). Coulomb and electron-phonon interactions in metals. *Physical Review B*, 94(15), 155145.
- [160] Rivadulla, F., Otero-Leal, M., Espinosa, A., De Andrés, A., Ramos, C., Rivas, J., & Goodenough, J. B. (2006). Suppression of ferromagnetic double exchange by vibronic phase segregation. *Physical Review Letters*, 96(1), 016402.
- [161] Abrashev, M. V., Bäckström, J., Börjesson, L., Popov, V. N., Chakalov, R. A., Kolev, N., ... & Iliev, M. N. (2002). Raman spectroscopy of CaMnO₃: mode assignment and relationship between Raman line intensities and structural distortions. *Physical Review B*, 65(18), 184301.
- [162] Kabanov, V. V., Zagar, K., & Mihailovic, D. (2005). Electric conductivity of inhomogeneous two-component media in two dimensions. *Journal of Experimental and Theoretical Physics*, 100(4), 715-721.
- [163] Zainullina, R. I., Bebenin, N. G., Ustinov, V. V., & Shulyatev, D. A. (2017). Elastic properties of La_{0.82}Ca_{0.18}MnO₃ single crystal. *Physics of the Solid State*, 59(2), 283-286.
- [164] Becker, T., Streng, C., Luo, Y., Moshnyaga, V., Damaschke, B., Shannon, N., & Samwer, K. (2002). Intrinsic inhomogeneities in manganite thin films investigated with scanning tunneling spectroscopy. *Physical Review Letters*, 89(23), 237203.

- [165] Mishchenko, A. S., & Nagaosa, N. (2004). Electron-phonon coupling and a polaron in the t-J model: from the weak to the strong coupling regime. *Physical Review Letters*, 93(3), 036402.
- [166] Rugar, D., Mamin, H. J., Guethner, P., Lambert, S. E., Stern, J. E., McFadyen, I., & Yogi, T. (1990). Magnetic force microscopy: General principles and application to longitudinal recording media. *Journal of Applied Physics*, 68(3), 1169-1183.
- [167] Vistoli, L., Wang, W., Sander, A., Zhu, Q., Casals, B., Cicheler, R., ... & Bibes, M. (2019). Giant topological Hall effect in correlated oxide thin films. *Nature Physics*, 15(1), 67.
- [168] Kanazawa, N., Onose, Y., Arima, T., Okuyama, D., Ohoyama, K., Wakimoto, S., ... & Tokura, Y. (2011). Large topological Hall effect in a short-period helimagnet MnGe. *Physical Review Letters*, 106(15), 156603.
- [169] Porter, N. A., Sinha, P., Ward, M. B., Dobrynin, A. N., Brydson, R., Charlton, T. R., ... & Marrows, C. H. (2013). Giant topological Hall effect in strained Fe_{0.7}Co_{0.3}Si epilayers. *arXiv preprint arXiv:1312.1722*.
- [170] Garcia, V., Bibes, M., Barthélémy, A., Bowen, M., Jacquet, E., Contour, J. P., & Fert, A. (2004). Temperature dependence of the interfacial spin polarization of La_{2/3}Sr_{1/3}MnO₃. *Physical Review B*, 69(5), 052403.
- [171] Nakazawa, K., Bibes, M., & Kohno, H. (2018). Topological Hall effect from strong to weak coupling. *Journal of the Physical Society of Japan*, 87(3), 033705.
- [172] Imbrenda, D., Yang, D., Wang, H., Akbashev, A. R., Kasaei, L., Davidson, B. A., ... & Spanier, J. E. (2016). Surface-and strain-tuning of the optical dielectric function in epitaxially grown CaMnO₃. *Applied Physics Letters*, 108(8), 082902.
- [173] Cohn, J. L., Peterca, M., & Neumeier, J. J. (2004). Low-temperature permittivity of insulating perovskite manganites. *Physical Review B*, 70(21), 214433.
- [174] Mikheev, E., Raghavan, S., Zhang, J. Y., Marshall, P. B., Kajdos, A. P., Balents, L., & Stemmer, S. (2016). Carrier density independent scattering rate in SrTiO₃-based electron liquids. *Scientific reports*, 6, 20865.
- [175] Béa, H., Dupé, B., Fusil, S., Mattana, R., Jacquet, E., Warot-Fonrose, B., ... & Barthélémy, A. (2009). Evidence for room-temperature multiferroicity in a compound with a giant axial ratio. *Physical Review Letters*, 102(21), 217603.
- [176] Wang, Y., Niranjana, M. K., Janicka, K., Velev, J. P., Zhuravlev, M. Y., Jaswal, S. S., & Tsymbal, E. Y. (2010). Ferroelectric dead layer driven by a polar interface. *Physical Review B*, 82(9), 094114.

- [177] Wang, L., Feng, Q., Kim, Y., Kim, R., Lee, K. H., Pollard, S. D., ... & Meng, W. (2018). Ferroelectrically tunable magnetic skyrmions in ultrathin oxide heterostructures. *Nature Materials*, 17(12), 1087.
- [178] Tsymbal, E. Y., & Panagopoulos, C. (2018). Whirling spins with a ferroelectric. *Nature Materials*, 17(12), 1054.

Resumé en Français

Introduction

La topologie dans la physique de la matière condensée est un domaine d'intérêt croissant en raison des phases topologiques et des phénomènes physiques distincts découverts au cours de la dernière décennie. Dans son sens le plus strict, la topologie est l'étude des propriétés qui sont conservées sous des déformations continues, et en tant que telle, elle fournit les moyens mathématiques d'étudier et de prédire de nouvelles phases et de nouveaux phénomènes, tels que les isolants topologiques et l'effet Hall quantique de spin. Dans l'espace réel, des structures topologiquement non triviales appelées skyrmions magnétiques peuvent être stabilisées dans des systèmes magnétiques [3, 20].

Les skyrmions magnétiques sont des structures en forme de vortex, avec une texture de spin couvrant toutes les directions de l'espace. La topologie de ces structures est quantifiée par la charge topologique Q définie comme le nombre de fois que les spins

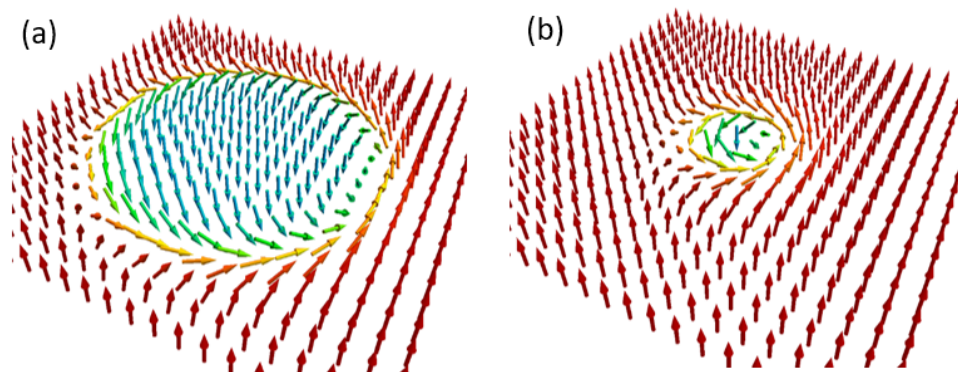


Figure A.1: (a) Croquis de bulles skyrmion et (b) skyrmions (image courtoisie de Joo-Von Kim).

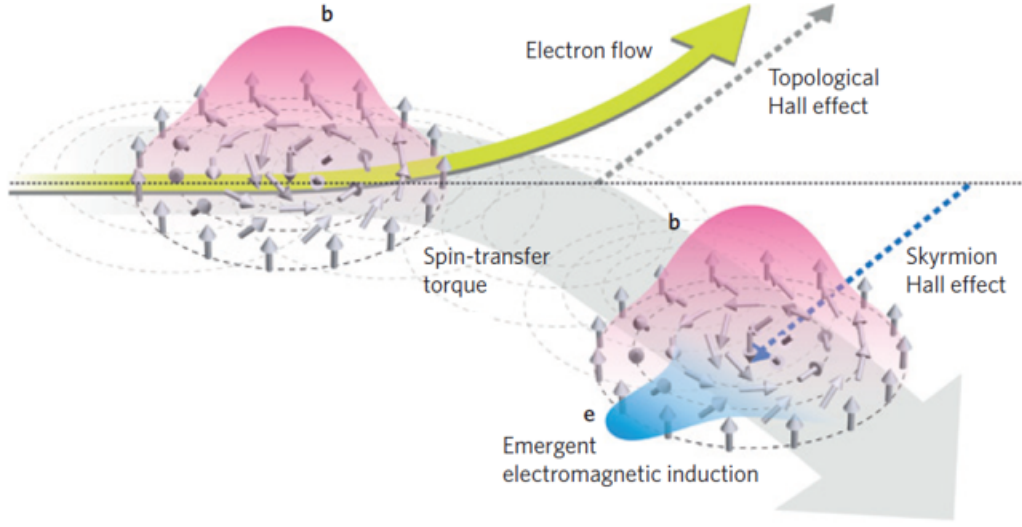


Figure A.2: (a) Représentation schématique des effets d'un courant traversant un skyrmion [3].

$\vec{n}(\vec{r})$ s'enroulent autour du coeur de skyrmion, ou [3]

$$Q = \frac{1}{4\pi} \int d\vec{r} \cdot [\partial_x \vec{n}(\vec{r}) \times \partial_y \vec{n}(\vec{r})] = pv.$$

Les skyrmions magnétiques naissent de la compétition entre l'échange et l'interaction Dzyaloshinskii-Moriya (DMI), qui, par nature, nécessite la brisure de symétrie. En raison de leur petite taille et de leur grande stabilité, les skyrmions magnétiques suscitent beaucoup d'intérêt pour des applications de stockage d'information [20]. Les structures topologiques de spin peuvent être stabilisées même en l'absence de rupture de symétrie, car la concurrence entre l'anisotropie magnétique et l'interaction dipolaire peut donner lieu à des bulles magnétiques avec une charge topologique non nulle Q . Ces bulles ont un diamètre de quelques centaines de nanomètres et sont généralement appelées bulles skyrmion.

Les structures topologiques de spin peuvent être utilisées dans une multitude d'applications. Par exemple, les mémoires magnétiques racetrack peuvent utiliser des skyrmions comme bit, pour un traitement et une lecture rapides des données. Les skyrmions peuvent même être utilisés dans des dispositifs de calcul de réservoir pour obtenir un calcul neuromorphique. Néanmoins, toute application possible nécessite la possibilité de détecter électriquement les skyrmions. L'un des moyens de détection est par effet Hall topologique. Lorsqu'un électron traverse un système magnétique à topologie non triviale, une charge topologique non nulle induit une phase géométrique de Berry, qui donne naissance à un champ magnétique émergent qui dévie l'électron (voir la figure A.2). Ceci peut être sondé par l'effet Hall, et s'appelle l'effet Hall

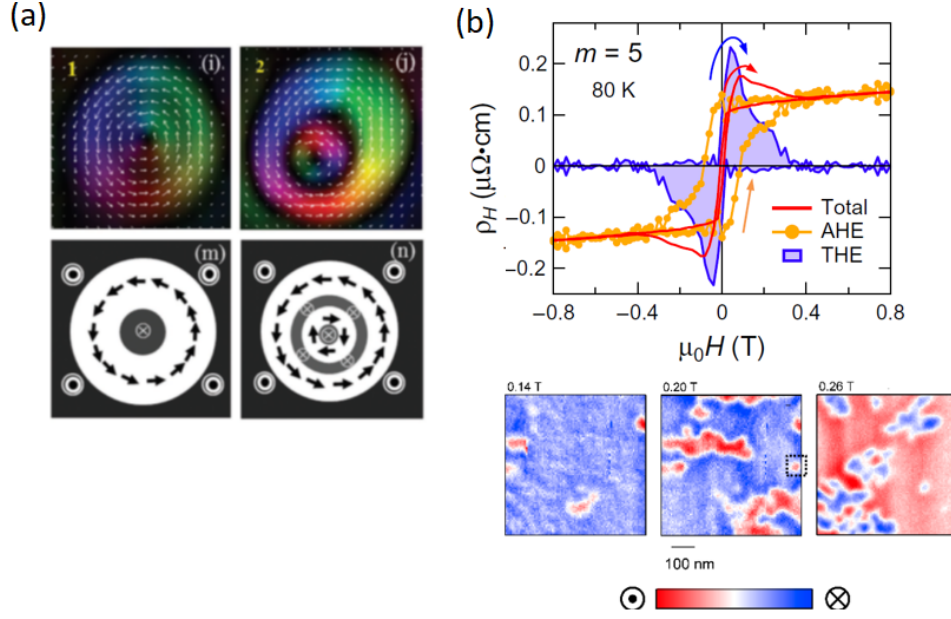


Figure A.3: (a) Aimantation des bulles de skyrmion dans $\text{La}_{0.825}\text{Sr}_{0.175}\text{MnO}_3$ et schéma de leur topologie [104]. (b) Effet Hall topologique de $\text{SrRuO}_3/\text{SrIrO}_3$, et microscopie à force magnétique montrant la présence de skyrmions dans le système [111].

topologique. Le modèle de Bruno est couramment utilisé pour comprendre cet effet, et donne une amplitude [28]

$$\rho_{THE} = \frac{P\langle b \rangle}{en} = \frac{P\sigma_{sk}\Phi_0}{en}$$

où P est la polarisation de la courant, $\langle b \rangle = \sigma_{sk}\Phi_0$ est le champ magnétique émergent et σ_{sk} est la densité du skyrmion.

Les oxydes pérovskites sont une classe de matériaux connus pour abriter une large gamme de phénomènes (transition métal-isolant, ordres magnétiques divers, supraconductivité, ferroélectricité, semi-métallicité). Ces matériaux sont également remarquablement sensibles aux stimuli (déformations et ingénierie des interfaces, champ magnétique et électrique, dopage), ce qui en fait des candidats idéaux pour l'étude des phénomènes physiques comme les états topologiques. Au cours des dernières années, on a observé de nombreuses structures topologiques des spins dans les oxydes. Les monocristaux centrosymétriques comme $\text{La}_{0.875}\text{Sr}_{0.175}\text{MnO}_3$ sont capables d'accueillir des bulles skyrmion stabilisées par des interactions dipôles [104], comme montré dans fig. A.3a. Les multicouches peuvent être utilisées pour induire la rupture de symétrie dans l'interface, comme dans $\text{SrRuO}_3/\text{SrIrO}_3$, où les skyrmions émergent et provoquent un effet Hall topologique [111]. (fig. A.3b). Il semble que, dans les oxydes, les systèmes centrosymétriques et non centrosymétriques peuvent présenter

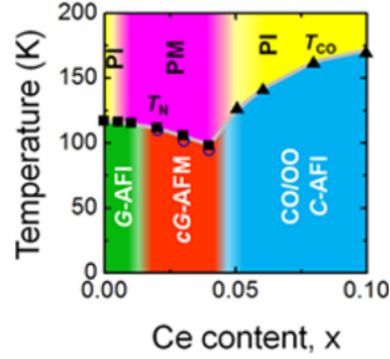


Figure A.4: Diagramme de phase des couches minces de CaMnO_3 dopés, sur des substrats YAlO_3 [125].

des structures topologiques des spins, ce qui fait de ces matériaux un terrain de jeu pour étudier comment ces structures se comportent en présence de degrés de liberté en interaction, de fortes corrélations et de fort couplage électron-boson.

Structure électronique des films minces de CaMnO_3 dopés

Afin d'étudier les structures topologiques des spins dans les matériaux oxydés, nous avons dû commencer par concevoir un matériau à anisotropie magnétique perpendiculaire, afin de stabiliser les structures topologiques des spins, et la métallicité, afin de les sonder par effet Hall topologique. Nous avons utilisé des couches minces de CaMnO_3 , déposés sur des substrats YAlO_3 , car elles peuvent croître épitaixialement avec une compression épitaixiale qui stabilise une aimantation perpendiculaire [125]. De plus, la compression épitaixiale stabilise une phase métallique à faible dopage de Ce (voir fig. A.4).

Nous avons d'abord étudié les propriétés électroniques de ces couches minces de CaMnO_3 . Les simulations de théorie fonctionnelle de la densité (DFT) montrent que le matériau est un isolant à transfert de charge, et que le dopage pousse l'énergie de Fermi dans la bande de conduction déjà à 2% dopage de Ce. Lorsque cela se produit, le matériau devient métallique et la surface de Fermi se forme. La surface de Fermi, représentée dans la fig. A.5a, est composé d'une sphère d'électrons 3D autour du point Γ , et de cylindres quasi-2D dépassant de Γ dans les directions x , y , et z . Une coupe le long de ΓMX est présentée dans la fig. A.5b, montrant que la surface de Fermi s'agrandit avec dopage, et que sur les coins de la zone Brillouin ($\pm\pi/a, \pm\pi/a$) des répliques de la sphère électronique 3D à Γ apparaissent. Ceci est dû à la distorsion orthorhombique, qui double la cellule unitaire dans l'espace réel, et la réduit de moitié dans l'espace réciproque.

Nous avons réalisé des mesures de spectroscopie photoélectronique résolue en angle (ARPES) pour mieux comprendre la situation. Figs. A.5c,d montrent des coupes de

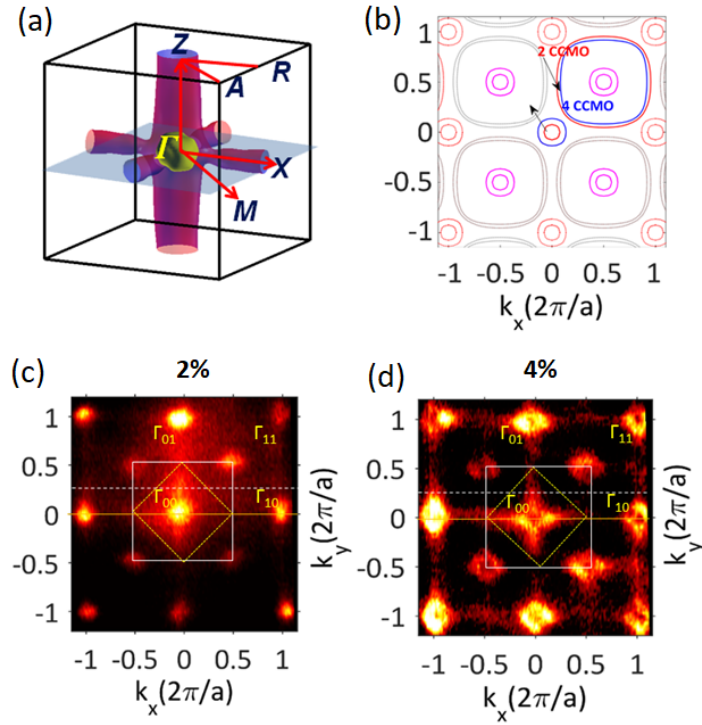


Figure A.5: (a) Surface de Fermi DFT et (b) coupe le long du plan ΓXY . Cartes de surface Fermi ARPES le long du plan ΓXM pour 2% (c) et 4% (d) de dopage mesuré à $h\nu = 643$ eV.

la surface Fermi le long de ΓMX pour 2% et 4% de dopage respectivement. Elles sont cohérentes avec les simulations DFT (fig. A.5b), et montrent que la surface Fermi augmente avec avec dopage, comme prévu. Aux coins de la zone de Brillouin se trouvent également les répliques de la surface de Fermi de la déformation orthorhombique.

Les dispersions d'énergie peuvent être prises à n'importe quel point de la surface Fermi. Figs. A.6a,b montrent la dispersion d'énergie de la sphère d'électrons 3D à Γ pour 2% et 4% dopage de Ce respectivement. Les maximums des courbes de dispersion d'énergie sont en bon accord avec les bandes de conduction de DFT, montrant que les électrons dans ces sphères 3D ont de faibles masses effectives ($0.35 - 0.4 m_e$). Dans le cas d'un dopage à 4%, à 80 meV de l'énergie de Fermi, le groupe montre un point d'inflexion, de sorte que la forme de la bande dévie d'un comportement parabolique. Ce point d'inflexion est indicatif d'une interaction avec un degré de liberté bosonique, avec une énergie d'environ 80 meV. Cette interaction raidit l'électron et augmente la masse effective de l'électron aux énergies au-dessus du point d'inflexion. Un point d'inflexion similaire peut être présent même à des dopages plus faibles, mais il est moins visible en raison de la plus faible largeur de bande occupée.

Les dispersions d'énergie mesurées dans les cylindres q2D sont présentées dans la fig. A.6c,d. Ces dispersions n'ont pas l'apparence d'une bande, mais plutôt d'une

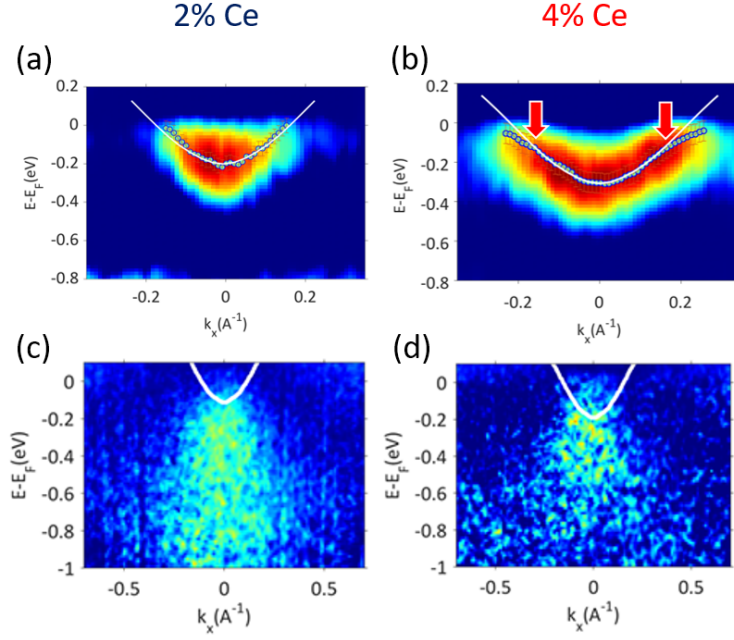


Figure A.6: Dispersion des bandes 3D autour de point Γ pour (a) 2% et (b) 4% de dopage, avec calculs DFT. Dispersion des bandes q2D, autour de $k_y = 0.5\pi/a$ pour (c) 2% et (d) 4% de dopage.

large chute d'eau dont l'origine est proche du niveau de Fermi E_F . Ce type de spectre est également différent d'un bien définie d'une quasi-particule. Cette chute d'eau asymétrique s'étendant dans les énergies de la bande de valence est la signature d'un fort couplage entre les électrons et de multiples degrés de liberté bosoniques [147]. Les bosons associés sont des phonons, qui interagissent fortement avec les porteurs et, alors que les porteurs se déplacent, ils traînent le long de la distorsion du réseau cristallin, augmentant leur masse effective [148]. Les quasi-particules qui en résultent sont appelées polarons.

Étonnamment, les deux bandes présentent des forces de couplage électron-phonon très différentes. Ceci contraste avec la théorie classique des polarons, où la force de couplage dépend des propriétés diélectriques du matériau, qui ne varient pas entre les bandes. En théorie quantique des polarons, l'interaction électron-phonon pourrait être différente pour différentes fonctions d'onde, mais nos calculs DFT ne montrent pas de différence substantielle entre les éléments de matrice des porteurs quasi-2D et 3D. La DFT s'appuie sur l'approximation de Migdal, c'est-à-dire négligeant les termes d'ordre supérieur de l'expansion de Feynman-Dyson (appelés corrections de vertex), en utilisant uniquement l'ordre le plus bas [151]. Le théorème de Migdal affirme que cette approximation est valable pour les métaux, les isolants et les semi-conducteurs légèrement dopés où $\Delta\epsilon_F > \hbar\omega_{ph}$. Cependant, dans CaMnO_3 légèrement dopé, la bande passante occupée est très faible, ce qui donne un petit $\Delta\epsilon_F$, comparable aux

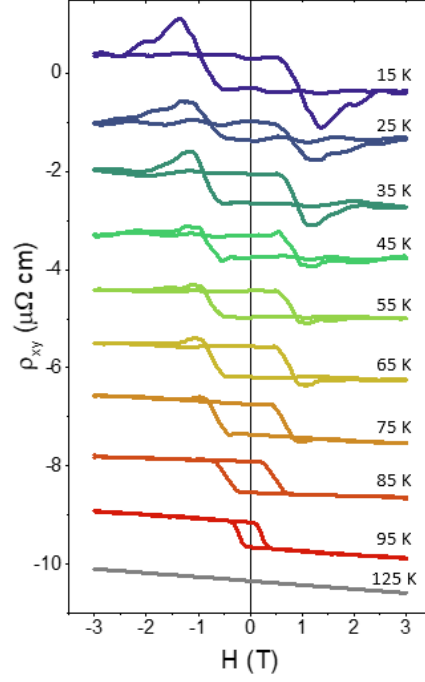


Figure A.7: Effet Hall anormal et topologique à différentes températures jusqu'à 95 K pour un échantillon dopé à 4%. Effet Hall normal à 125 K. Les données sont décalées verticalement pour plus de clarté.

énergies des phonons couplés $\hbar\omega_{ph} = 80$ meV. Pour la bande 3D, $\Delta\epsilon_F > \hbar\omega_{ph}$ et donc l'approximation Migdal tient, cependant la bande de valence q2D est décalée vers le haut par corrélations, de sorte que $\Delta\epsilon_F \approx \hbar\omega_{ph}$ où l'approximation Migdal échoue, donnant lieu à un renforcement de l'amplitude du couplage électron-phonon par corrections de vertex.

Les manganites comme CaMnO_3 présentent des comportements de transport électronique qui sont généralement interprétés en utilisant les polarons comme seuls porteurs de charge. Cependant, nous avons montré comment les porteurs aussi légèrement couplés aux phonons sont présents dans la bande de conduction de CaMnO_3 . Nous avons donc élargi le modèle polaronique du transport électronique de manganite pour inclure ces porteurs légers, et l'expression résultante montre comment cette hypothèse à deux porteurs est cohérente avec les mesures de transport observées, et que les polarons lourds sont encore capables de dominer le transport, en raison de leur grande densité des porteurs.

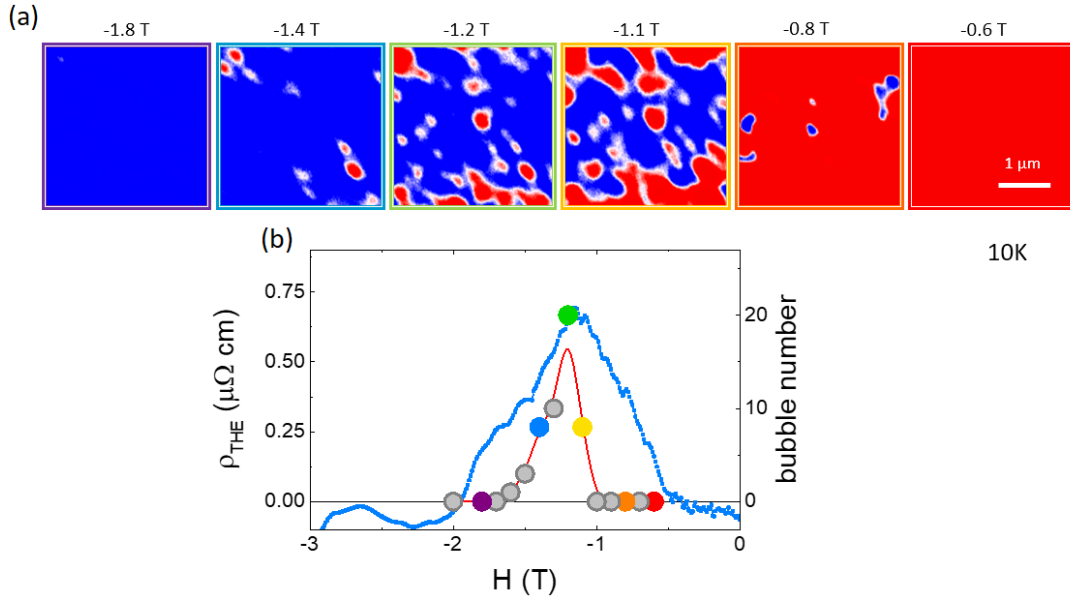


Figure A.8: (a) Images MFM à 10 K à différents champs magnétiques négatifs, balayant vers le bas après application d'un champ perpendiculaire positif de +3T. (b) Dépendance avec champ magnétique de l'effet Hall topologique (ligne bleue) et du nombre de bulles observées dans les images MFM (points) à 10 K.

Effet Hall topologique géant dans les couches minces de CaMnO_3 dopé

Pour en revenir aux propriétés magnétiques, nous avons mesuré l'aimantation de couches minces de CaMnO_3 dopé avec Ce pour confirmer que la compression épitaxiale induit une aimantation perpendiculaire. Ceci, combiné à la métallicité, rend ces échantillons intéressants pour la recherche de structures topologiques des spins dans les oxydes. Nous avons mesuré l'effet Hall d'une couche mince dopée à 4% de Ce, montré dans fig. A.7. Au-dessus de T_c , le signal est un effet Hall linéaire ordinaire. Sous T_c , le signal de Hall développe une composante hystérétique (voir 95 K). Cette composante suit l'aimantation, et est l'effet Hall anormal d'un échantillon magnétisé perpendiculairement. A des températures encore plus basses (75 K et moins), une troisième composante apparaît sous la forme de deux pics anti-symétriques centrés autour de 1 T. Cette troisième composante a la forme particulière de l'effet Hall topologique, décrite dans la première partie de ce résumé. Cela suggère qu'il y a des charges topologiques qui apparaissent après l'inversion de aimantation.

Nous avons utilisé la microscopie à force magnétique (MFM) pour examiner notre demande. Dans la fig. A.8 nous montrons de telles images, prises après saturation positive de l'aimantation (en appliquant +3 T), puis en balayant le champ vers le bas. A -0,6 T, l'aimantation est encore complètement alignée dans le sens positif

(couleur rouge). Quand la manganite nucléée des domaines à aimantation négative (bleu), des bulles à aimantation positive (rouge) commencent à apparaître. A -1,2 T, la densité des bulles rouges atteint son maximum et diminue progressivement avec l'augmentation du champ. Ces bulles ont des diamètres de l'ordre de 100 – 300 nm, comme les bulles topologiques rapportées dans d'autres oxydes centrosymétriques [104, 101, 102, 107].

Dans la figure A.8 nous montrons la densité calculée des domaines de bulles en fonction de l'effet Hall topologique, à 10 K. On peut voir que la densité des bulles varie fortement avec le champ, et est maximale à un champ proche du pic de l'effet Hall topologique H_T . A différentes températures, la densité de la bulle est maximale à des champs proches de H_T . Ceci suggère que l'effet Hall topologique provient d'une texture des spins spécifique associée à ces bulles magnétiques. Puisque CaMnO_3 est centrosymétrique et sans DMI interfaciale, ces bulles ne peuvent être des skyrmions magnétiques. Cependant, la compression épitaxiale stabilise l'anisotropie magnétique contre les interactions dipôles, ce qui permet à ces couches minces d'abriter les bulles skyrmion.

Bien que nous ne puissions le vérifier directement, les bulles observées dans nos échantillons pourraient porter une charge topologique tout comme les skyrmions standard. Dans ce scénario, les bulles observées contribueraient à l'effet Hall topologique par un mécanisme de phase de Berry. En utilisant le modèle de Bruno avec la densité de bulles obtenue, nous calculons une amplitude de l'effet Hall topologique 40 fois plus faible que ce que nous observons. Pour étudier cet écart, nous avons mesuré l'effet Hall topologique de couches minces avec différents niveaux de dopage. Tout comme pour le dopage à 4%, les images MFM révèlent la présence de bulles apparaissant en même temps que l'effet Hall topologique. Fig. A.9 résume ces mesures. Lorsque n diminue, l'effet Hall topologique diverge plus rapidement que la tendance $1/n$ obtenue avec le modèle de Bruno. Il semble que ce modèle soit non seulement incapable d'expliquer la grande amplitude de l'effet, mais aussi d'expliquer la forte dépendance avec le dopage.

Plutôt qu'un modèle pour le régime de couplage fort, dans le cas du CaMnO_3 faiblement ferromagnétique, un modèle applicable aux couplages plus faibles est mieux adapté. Ici, il faut considérer non seulement les processus adiabatiques (phase de Berry) mais aussi les processus non-adiabatiques pour le mouvement des électrons dans une texture des spins, comme décrit dans [171]. La résistivité de l'effet Hall topologique devient

$$\rho_H \propto \frac{Jm^*}{n^{5/3}}$$

où J est lié au couplage Hund entre les électrons de conduction et l'aimantation, multiplié par l'aimantation relative, qui est proportionnelle à la densité de porteurs n . De façon remarquable, l'amplitude devient proportionnelle à la masse effective, qui

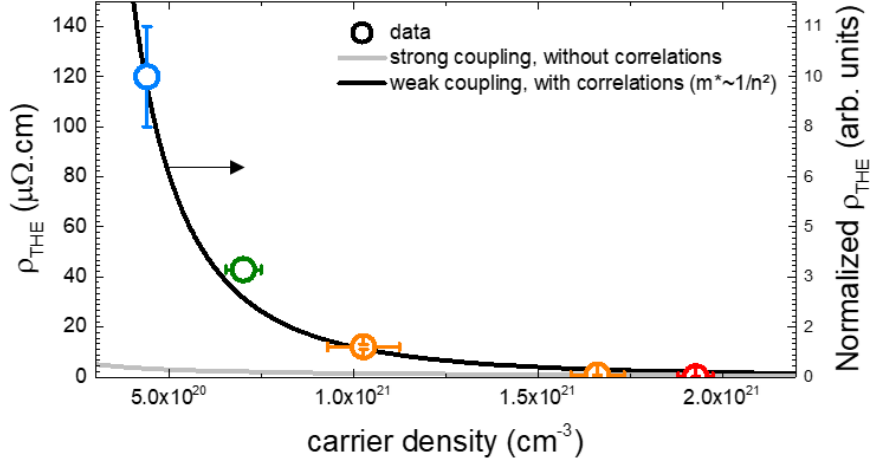


Figure A.9: Dépendance de l'effet Hall topologique avec densité des porteurs. Le modèle est représenté normalisé à la valeur expérimentale à $1.03 \times 10^{21} \text{ cm}^{-3}$.

peut généralement être augmentée dans les oxydes. En particulier, lorsque la transition vers l'état isolant se fait du côté métallique (en réduisant le niveau de dopage), la masse effective diverge, grâce à des corrélations électroniques. Cette augmentation est la suivante

$$m^* \propto \frac{1}{n^\alpha}$$

où typiquement $\alpha = 1$. Pour les faibles épaisseurs, les effets à plusieurs corps amplifient cet effet, apportant $\alpha = 2$.

Dans la fig. A.9 nous comparons la dépendance expérimentale de l'effet Hall topologique avec la densité des porteurs avec le modèle dans le régime de couplage fort et dans le régime de couplage plus faible considéré ici. La dépendance en dopage est bien en accord avec ce modèle, en utilisant $\alpha = 2$, ce qui montre comment de fortes corrélations peuvent augmenter l'effet Hall topologique dans les oxydes fortement corrélés.

Conclusions

Dans la première partie de ce travail, nous avons imagé directement la surface Fermi de couches minces dopées CaMnO_3 , et observé deux types de porteurs: les polarons lourds et les électrons légers. Nous avons montré comment ces résultats sont cohérents avec le comportement de transport de ces films minces et, en fin de compte, nous avons fourni des informations sur la façon dont les électrons se délocalisent et se couplent aux phonons dans les isolants dopés de Mott. Dans la deuxième partie, nous avons décrit l'effet Hall topologique géant observé dans le CaMnO_3 dopé au Cérium. Les mesures MFM montrent comment cet effet se produit en même temps

que la formation de bulles magnétiques. En mesurant cet effet pour différents niveaux de dopage, nous avons observé une augmentation de cet effet Hall topologique, qui démontre comment les corrélations et la topologie peuvent interagir dans les oxydes.

Titre : Propriétés topologiques et électroniques des couches minces de manganite dopées

Mots clés : Oxydes, Couche mince, Effet Hall topologique

Résumé : Les couches minces d'oxyde présentent un large éventail de phénomènes physiques et riches diagrammes de phase, ajustables par l'ingénierie des déformations et des interfaces. Le CaMnO_3 , en particulier, est extrêmement sensible au dopage et aux contraintes d'épitaxie et, lorsqu'il est élaboré sous compression, il passe d'un état isolant et antiferromagnétique à un état métallique et faiblement ferromagnétique à seulement 2% de dopage au Ce.

Nous avons utilisé une combinaison de spectroscopie de photoémission résolue en angle, de magnéto-transport et de théorie de la fonctionnelle de la densité pour étudier les propriétés électroniques de ce matériau. Nous avons observé l'existence de deux porteurs de charge distincts, les électrons légers et les polarons lourds, dont la nature diffère en raison de leur couplage radicalement différent aux phonons. Nous attribuons ces différences à un remplissage relatif différent de la bande en raison des corrélations, qui améliorent considérablement le couplage aux phonons de la bande des polarons lourds. Les expériences de magnéto-transport révèlent que la bande polaire domine le transport malgré sa mobilité réduite.

La compression épitaxiale donne également lieu à une forte anisotropie magnétique qui stabilise des bulles magnétiques et s'accompagnent d'un effet

Hall topologique. Cela suggère que ces bulles ont un caractère topologique. L'effet Hall topologique diverge lorsque la manganite s'approche de la transition métal-isolant à faible dopage. Nous avons utilisé une théorie récemment développée pour interpréter ce comportement, et nous concluons que des corrélations peuvent entrer en jeu, augmentant la masse effective des porteurs et par conséquent l'effet Hall topologique.

Comme cette manganite est très sensible aux changements de densités de porteurs, nous avons développé des transistors à effet de champ ferroélectriques $\text{BiFeO}_3/(\text{Ca,Ce})\text{MnO}_3$. Lors de la commutation de la polarisation ferroélectrique de la couche supérieure de BiFeO_3 , nous n'avons pu observer de changement notable dans les propriétés des couches de manganite sous-jacentes. Nous avons utilisé la microscopie électronique en transmission pour étudier les propriétés de ces bicouches avec une résolution atomique, et nous avons observé que l'épinglage de polarisation à l'interface $\text{BiFeO}_3/(\text{Ca,Ce})\text{MnO}_3$ empêche une commutation complète de la polarisation et réduit ainsi la capacité opérationnelle de ces dispositifs. Néanmoins, nous avons pu détecter l'influence de la polarisation ferroélectrique sur les propriétés électroniques de la manganite à l'échelle atomique.

Title : Topological and electronic properties of electron-doped manganite thin films

Keywords : Oxides, Thin Films, Topological Hall effect

Abstract : Oxide thin films feature a wide range of physical phenomena and rich phase diagrams tunable by strain and interface engineering. CaMnO_3 , in particular, is extremely sensitive to both doping and strain and, when grown with compressive strain, transitions from an insulating and antiferromagnetic state to a metallic and weakly ferromagnetic state at only 2% Ce doping.

We used a combination of angle-resolved photoemission spectroscopy, magnetotransport, and density functional theory to study the electronic properties of this material. We observed the existence of two separate charge carriers, light electrons and heavy polarons, whose physical nature differs because of drastically different couplings to phonons. We ascribe these differences to a different relative band filling due to correlations, which enhance greatly the coupling to phonons of the heavy polarons band. Magnetotransport experiments reveal that the polaron band dominates transport despite its lower mobility.

Compressive strain also gives rise to a strong magnetic anisotropy which stabilizes magnetic bubbles that accompany a topological Hall effect. This sug-

gests that these bubbles have topological character, i.e. are skyrmion bubbles. The topological Hall effect diverges as the manganite approaches the metal-insulator transition at low dopings. We used a recently developed theory in order to interpret this behavior, and we conclude that correlations may come into play, enhancing the effective mass of the carriers, and in turn the topological Hall effect.

As this manganite is highly sensitive to changes in doping and carrier density, we grew $\text{BiFeO}_3/(\text{Ca,Ce})\text{MnO}_3$ ferroelectric field-effect transistors. Upon switching the ferroelectric polarization of the BiFeO_3 top layer, we could not observe any sizable changes in the properties of the underlying manganite layers. We used transmission electron microscopy to study the properties of these bilayers with an atomic resolution, and we observed that polarization pinning at the $\text{BiFeO}_3/(\text{Ca,Ce})\text{MnO}_3$ impedes a complete switch of the polarization and so reduces the operational capabilities of these devices. Nevertheless, we could detect modifications of the electronic properties of the manganite induced by polarization reversal at the atomic scale.

